Design of a Shock Tube for Jet Noise Research

by

John Matthew Kerwin

S.B. Aeronautics and Astronautics, Massachusetts Institute of Technology, 1994

Submitted to the Department of Aeronautics and Astronautics
in partial fulfillment of the requirements for the degree of

Master of Science

at the

MASSACHUSETTS INSTITUTE OF TECHNOLOGY

June 1996

Author .....
Department of Aeronautics and Astronautics
April 16, 1996

Certified by .....
Professor Ian A. Waitz
Assistant Professor of Aeronautics and Astronautics
Thesis Supervisor

Accepted by .....
Professor Harold Y. Wachman
Chairman, Department Graduate Committee

Design of a Shock Tube for Jet Noise Research

by

John Matthew Kerwin

Submitted to the Department of Aeronautics and Astronautics
on April 16, 1996, in partial fulfillment of the
requirements for the degree of
Master of Science

Abstract

This thesis describes the design of a shock tube for the study of supersonic free jets. The primary purpose of the facility will be to study noise suppressor nozzles for application on supersonic civil transport aircraft. The shock tube has many strengths; it is mechanically simple, versatile, has low operating costs, and can generate acoustic and fluid dynamic data that is comparable to that of steady state facilities.

A reflection-type shock tube was designed to produce a reservoir of fluid at total temperatures and pressures analogous to those at the exit of a gas turbine engine. This fluid will be exhausted through a nozzle, generating a turbulent jet inside an anechoic test cell. Using air as the test gas, jet total temperatures up to 1750 K and total pressures up to 38 atm can be achieved. In addition, the shock heating creates highly uniform total temperature and pressure profiles at the nozzle inlet, eliminating the core noise often present in steady-state, vitiated air facilities. Lastly, the short duration of the test allows for relatively inexpensive stereo-lithography nozzles to be tested at realistic flow conditions. Fluid dynamic and acoustic measurements including thrust, Mie scattering to determine mixedness, and far-field noise will be taken in the facility.

An analysis is presented of the shock tube and fluid jet, and a detailed mechanical design of the facility is included. The optimum shock tube geometry was established using an ideal one-dimensional gas dynamic model with corrections to account for the growth of an unsteady boundary-layer. The nozzle and jet starting processes were investigated to estimate the duration of the quasi-steady, fully-developed jet. Requirements for noise measurements are discussed, including frequency scaling, high frequency measurement limits, uncertainties in power spectral analysis, and required sampling times.

Two shock tube configurations are presented: (1) an $8''$ diameter, $38'$ long, vertical shock tube with a $16' \times 19'$ test cell and (2) a $12''$ diameter, $60'$ long, horizontal shock tube with a $19' \times 26'$ test cell. The $12''$ facility will be constructed. Using this facility 18 ms duration tests can be performed on a $5.2''$ exit diameter noise suppressor nozzle (roughly $1/12^{th}$ of full scale). Frequencies up to 80 kHz (corresponding to 6.7 kHz full scale) can be measured, and it is expected that noise power spectrum measurements within ± 2 dB can be obtained with 3 shock tube runs for full scale frequencies above 500 Hz .

Thesis Supervisor: Professor Ian A. Waitz
Title: Assistant Professor of Aeronautics and Astronautics

Acknowledgments

The completion of this thesis would have been impossible without the advice, assistance and friendship of a number of people. Foremost, I would like to thank Prof. **Ian A. Waitz** for providing me with countless opportunities throughout my stay at MIT and for his guidance during this project. I am also deeply indebted to Dr. **Gerry Guenette** for his enthusiasm and mechanical inspirations, and to Prof. **Edward Greitzer** for his many insights into the project.

There are many others I would like to thank:

To Prof. **Uno Ingard**, Mr. **Chet Killam**, Prof. **Mohammad Durali**, Dr. **David Davidson**, Dr. **Mike Miller**, Mr. **Daniel Yukon** and Dr. **Terry Parker** for all their help and expertise along the way.

To Dr. **Choon Tan** for friendly advice and funding our caffeine addiction.

To my officemates **Greg Stanislaw**, **Dave Tew**, **Luc Frechette** and "F-as-in-Frank" **Fouzi Al-Essa** for their friendship, humor, advice, sarcasm, raillery, and general tomfoolery.

To my Unified comrades, **Sonia**, **Julian**, and **Mike** for having the tenacity to still be here, and to **Christine**, **Jun**, and **Larry** for having the good sense to get away.

To **Willy** for five years of wit, friendship, adventures, and all-nighters.

A special thanks to **Kaesmene**, a close friend, poet, and editor for helping me with my prose, and to **Elliott**, a long time friend, for being there through it all.

To my sister for her free psychoanalysis and counseling.

And, most of all, to my parents for their loving support; this thesis is dedicated to them.

Support for this project was provided by NASA Langley, under contract NAG-1-1511 and supervision of John. M. Seiner. This support is gratefully acknowledged.

Contents

List of Figures

List of Tables

Nomenclature

Roman

A	cross sectional area
D	diameter
Ec	Ecardt number
K	kinematic momentum, $\equiv 2\pi \int_0^\infty u^2 y dy$
M	Mach number
NPR	primary nozzle pressure ratio, p_t/p_0
Pr	Prandtl number
Re	Reynolds number
Re_t	transition Reynolds number
Sr	Strouhal number, $\equiv \frac{fD_e}{u_e}$
T	static temperature
T_r	adiabatic recovery temperature
T_t	total temperature
a	local speed of sound
c_s	shock speed
c^-	negative expansion characteristic
c^+	positive expansion characteristic
f	frequency
h_n	height of nozzle above test cell floor
l	length
l_{jet}	jet length
l_{pc}	jet potential core length
$\dot{m}_p$	massflow through primary nozzle

p	static pressure
p_t	total pressure
r	distance from nozzle exit
R_{mic}	distance to microphones
u	velocity (laboratory frame)
v	velocity (shock stationary frame)
x	axial distance

Greek

χ_{He}	mass fraction of helium in driver gas
γ	ratio of specific heats
ρ	density
μ	viscosity
δ	boundary layer thickness
δ^*	boundary layer displacement thickness
ϵ_o	virtual kinematic visconsity, $\approx (0.0161)\sqrt{K}$
τ_x	wall shear force
τ_1	arrival time of disturbance from shock-interface interaction
τ_2	arrival time of secondary expansion
τ_3	arrival time of primary expansion
τ_{exp}	test time limited by reflected expansion waves
τ_{exg}	test time limited by exhaustion of test gas
τ_{jet}	jet starting time
τ_{nozzle}	nozzle starting time
θ	boundary layer momentum thickness
ψ	directivity angle, measured from upstream jet axis
ν	kinematic viscosity
ζ	boundary layer similarity parameter, $\zeta \equiv \frac{y}{\delta}$; $y < \delta$, $\zeta \equiv 1$; $y > \delta$

Subscripts

dn	driven section
dr	driver section
c	jet centerline velocity
e	ejector exit
o	conditions immediately behind shock
p	primary stream
r	reflected shock
s	secondary stream
s	incident shock
st	shock tube
t	total or stagnation quantity
w	wall
0	ambient conditions
$1-9$	conditions in shock tube, see figure 2-2

Superscripts

$*$	primary nozzle throat
$'$	denotes shock relative frame

Miscellaneous

p_4/p_1	diaphragm pressure ratio

Chapter 1

Introduction

1.1 Background

Recently there has been a renewed interest in developing a supersonic commercial transport for trans-Pacific operations. Before a concerted design effort can be undertaken, however, it must be established whether or not such an aircraft would be environmentally viable. One of the primary environmental concerns is noise pollution in communities near airports. The current supersonic transport, the Concorde, fails to meet the FAR 36 Stage III noise regulations, and it receives a special exemption in order to operate at U.S. airports. The next generation of high speed civil transports (HSCTs) will be required to meet these regulations if they are to operate as frequently as their subsonic counterparts.

The dominant noise source at take-off and landing is the high speed exhaust jet from the engines. A significant reduction in jet velocity during this phase of operation has been widely accepted as the only promising way to meet noise goals. Current efforts to develop such a technology have focused on acoustically lined mixer-ejector nozzles similar to that shown in Figure 1-1. These nozzles use deployable chutes to mix ambient air with engine exhaust inside an acoustically treated duct. This reduces the jet exit velocity and, correspondingly, the turbulent intensity of the free jet and the associated noise. Thrust loss and weight are critical parameters for the nozzle design. To be a viable concept, a noise reduction of at least 3 $EPNdB$ per percent thrust loss will be required, while at the same time adding less than 20% to the engine weight. It is essential, therefore, to mix the streams as rapidly as possible to reduce the required duct length, and to perform the mixing with minimal losses.

Recent research has shown that a passive, lobed mixing device can be used to rapidly

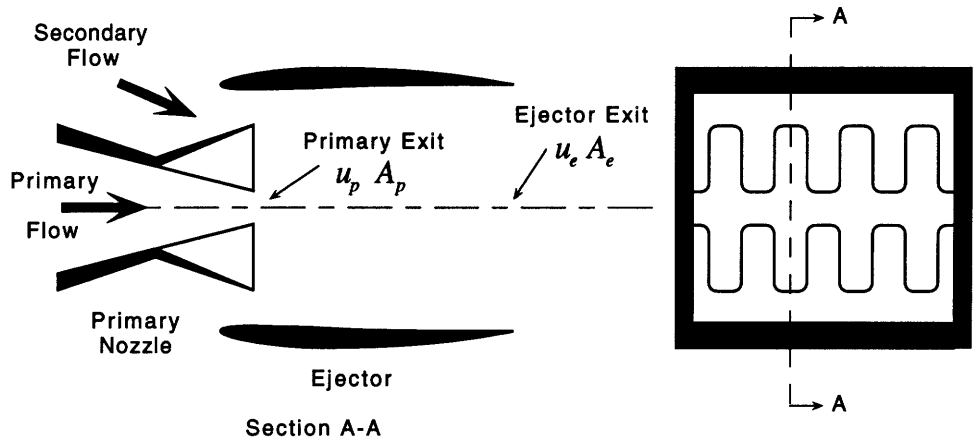

Figure 1-1: Section and rear view of a typical mixer-ejector nozzle for jet noise suppression, adapted from Lord *et al.* [16]

mix co-flowing streams with relatively low losses [6][16]. A schematic of a lobed mixer is shown in Figure 1-2. There are two distinct flow features responsible for this rapid mixing. First, there is a larger initial interfacial mixing area between the two streams due to the convoluted trailing edge. Second, the presence of counter-rotating streamwise vortices on the interface between the two streams stretch the interface. This provides both additional mixing area and increased flow property gradients which are the driving potential for the mixing.[5]

To date, the HSCT mixer/ejectors have fallen short of the noise reduction goals. The design efforts, however, have relied largely on empirical methods. A greater emphasis on physically-based understanding of noise suppressor performance could provide a road map for optimizing designs. This is the goal of research being conducted at the Aero-Environmental Research Laboratory at MIT. Experimental and computational tests have provided insights into the detailed fluid mechanics of noise suppressor nozzles [35][36][13] and allowed for the creation of models of gross fluid mechanical behavior [6]. Currently, a system-level model is being developed to provide a physically-based noise suppressor design tool. One critical component of an effective noise suppressor system model which does not currently exist is a simplified acoustic sub-model.

1.2 Motivation

In order to establish links between the dominant flow structures and acoustic radiation of hot supersonic jets and to enable the development of simplified acoustic models, carefully

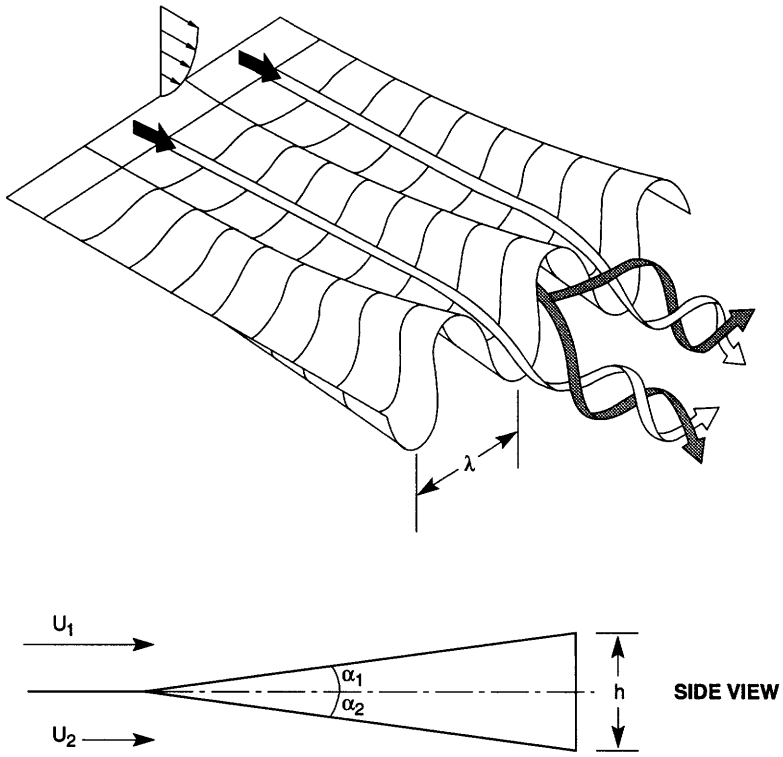

Figure 1-2: Perspective and side view of a typical lobed mixer, adapted from Presz *et al.* [29]

controlled experiments need to be conducted. An ideal facility for these tests is an acoustic shock tube. Over certain operating ranges a shock tube can be used to produce fluid mechanic and acoustic data which matches that obtained in steady-state facilities. Furthermore, the facility can provide an economical, rapid prototyping and test capacity that does not currently exist for designing jet noise suppressors.

Shock tubes have been used to produce high temperature supersonic jets for acoustic studies on three previous occasions. In the 1970's experiments were carried out by Prof. Louis at MIT [17]. A four inch shock tube facility was used to test round and rectangular nozzles. Experiments were also conducted by Oertel and presented at the 10^{th} Shock tube Symposium [25]. These experiments focused on Mach wave radiation from supersonic jets. In neither of these two previous efforts were comparisons made to steady-state data. The only other jet noise research performed using a shock tube was completed at Manchester University in collaboration with Rolls Royce, but the results have not been reported in open literature. The experimental setup at Manchester University, however, was significantly different than what is presented here. Only cold-flow tests were conducted, using helium and argon as test gases to produce the required velocities.

When constructed, this shock tube-based jet noise facility will be the only one of its kind. Mie scattering imaging of the mixing layer coupled with acoustic measurements from a linear microphone array will allow links between mixing layer structures and radiated noise to be identified. Flexibility of driver gas composition and pressure in this facility will allow the realization of a wide range of jet stagnation temperatures (up to 1750 K) and pressures (up to 38 atm, enough to drive a fully expanded $M = 3.0$ nozzle). This operating range spans the full range of interest for the HSCT. One of the advantages of using a shock tube as a jet noise source is that the total temperature and pressure profiles at the nozzle inlet are uniform as a result of shock heating. Thus the jet noise is pure, and does not contain the core noise often present in large steady-state, vitiated air facilities. Also, with modern measurement techniques, the short run times can be turned into a benefit; relatively inexpensive stereo-lithography models can be tested at realistic flow conditions. In addition to these technical advantages, the size of the shock tube facility makes it ideally suited to operation in a research environment. Ten runs a day can be completed with minimal cost per run and parametric testing can be performed more economically and faster than in a steady state facility.

1.3 Facility Objectives

The objective of the shock tube research facility is to elucidate the links between acoustics and flow structure in strongly augmented mixing flows typical of jet noise suppressors. Clarifying these links is necessary to provide a basis for understanding noise generation internal to the ejector, in designing acoustic treatment, and in developing and validating simplified models for acoustic radiation which may be incorporated into a mixer-ejector system model.

Thus, the specific objectives of the shock tube facility are to create a scaled jet analogous to that of the HSCT at take-off and to obtain acoustic and fluid dynamic measurements that include thrust, Mie scattering of mixedness, and far field noise. The following parameters were taken as the baseline performance goals for the shock tube design:

- Ejector Exit Velocity: $u_e \approx$ 1350 to 1750 ft/s (400 to 530 m/s)
- Primary Nozzle Mach Number: $M_p \approx 1.5$ or less

- Primary Nozzle Pressure Ratio (NPR): $p_{t_5}/p_0 \approx 3.4$
- Primary Stream Total Temperature: $T_{t_5}/T_0 \approx 2.5$ to 3.0
- Primary Nozzle Throat Area: $A^* \approx 1320\ in^2$ (0.85 m^2)
- Secondary/Primary Stream Area Ratio: $A_s/A_p \approx 1.2$ to 2.5
- Ejector Length/Diameter: $l_e/D_e \approx 1.5$ to 3.0

The shock tube was designed for optimum performance over these ranges.

In addition to satisfying these requirements, the facility was designed to be as flexible as possible to enabling testing of a wide range of gas turbine nozzles. With the current design, the shock tube will be capable of driving a perfectly expanded Mach 3.0 jet at a total temperature as high as 1750 K.

1.4 Facility Overview

Two shock tube configurations were investigated. The primary focus of the thesis will be an $8''$ diameter vertical shock tube that was designed to generate a scaled jet inside a $16' \times 19'$ test cell. During the writing of this thesis, however, an alternate laboratory space became available that enabled an expansion of the shock tube's capabilities. In this new space, the test cell is larger, $19' \times 26'$, and the shock tube can be oriented horizontally and scaled up to a $12''$ diameter. It is the $12''$ diameter facility that will eventually be built. While the fluid mechanic and acoustic performance of both the $12''$ and $8''$ shock tubes are discussed in this thesis, the detailed mechanical design is presented only for the $8''$ tube.

1.4.1 $8''$ Diameter Vertical Shock Tube

The original configuration would allow for approximately 9 ms of test time on up to a $1/16^{th}$ scale HSCT nozzle. The nozzle is driven by a vertically oriented shock tube spanning approximately $40'$ from the sub-basement floor to the third floor laboratory as shown in Figure 1-3. The tube consists of two sections separated by a diaphragm. The upper (driven) section is filled with the test gas, air in this case, and evacuated to about 1/10 atmosphere. The lower (driver) section is filled with a mixture of helium and argon and pressurized to between 4 and 50 atmospheres. The experiment is initiated by rupturing the

diaphragm which, in turn, causes a shock wave to propagate through the test gas. When this shock reflects from the end-plate holding the nozzle, it leaves behind it a reservoir of high temperature, high pressure fluid, which will drive the nozzle at conditions analogous to that at the exit of a gas turbine engine.

The driver section is rigidly connected to the sub-basement floor, so that all loads imparted on the tube are carried directly to the foundation. The driven section, on the other hand, is counterweighted and mounted on casters to allow access to the diaphragms. The height of the entire shock tube can be adjusted by changing the length of the spacer section on the tube base. This enables acoustic measurements to be taken for both the up-stream and down-stream arcs. During the tests, the sections are securely fixed together by a series of bolt circles.

The nozzle exhausts into an anechoic test cell which houses the microphones, laser, and all other acoustic and aerodynamic instrumentation. The nozzle height can be adjusted from $16''$ to $72''$ above the test cell floor in order to set the relative position of the fluid jet and the microphone array. A hatch is located directly above the nozzle to allow exhaustion of the jet plume and prevent over-pressure in the room. The acoustic insulation proposed is $4''$ thick fiberglass Sound Batt which will result in a 10 dB reduction in acoustic intensity for reflected frequencies greater than 1000 Hz.

One of the primary limitations of this configuration, as will be described in Chapter 3, is the small size of the test cell. The microphones can be placed a maximum of $131''$ from the nozzle exit. This means that far field acoustic measurements can only be taken on HSCT nozzles smaller than $1/20^{th}$ scale. The interesting frequency range on nozzles that small would extend over 100 kHz, well beyond what can be accurately measured. Larger nozzles, i.e. $1/16^{th}$ scale, radiate lower frequencies but the microphones would be in the near-field, requiring that corrections be made in order to extrapolate to far-field behavior.

1.4.2 $12''$ Diameter Horizontal Shock Tube

The alternate location for the facility allows for the shock tube to be oriented horizontally and alleviates many of the space constraints. Far-field acoustic measurements could be taken on up to a $1/12^{th}$ scale HSCT nozzle with close to 16 ms of total test time. Figure 1-5 shows a schematic of microphone locations for this new test cell. The microphones can be placed along a wide arc $182''$ from the nozzle exit, allowing far-field measurements to be

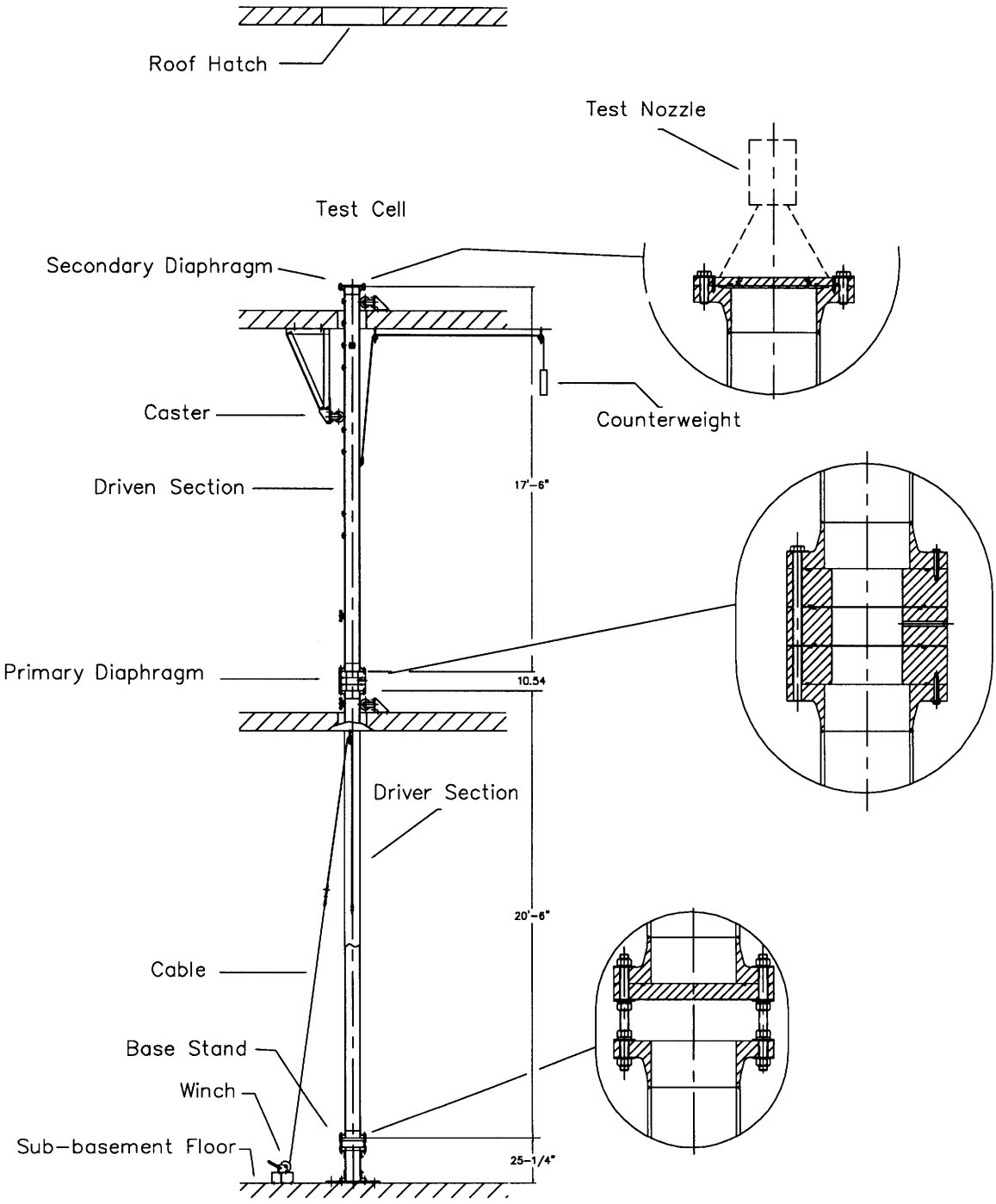

Figure 1-3: Facility overview of the 8″ vertical shock tube.

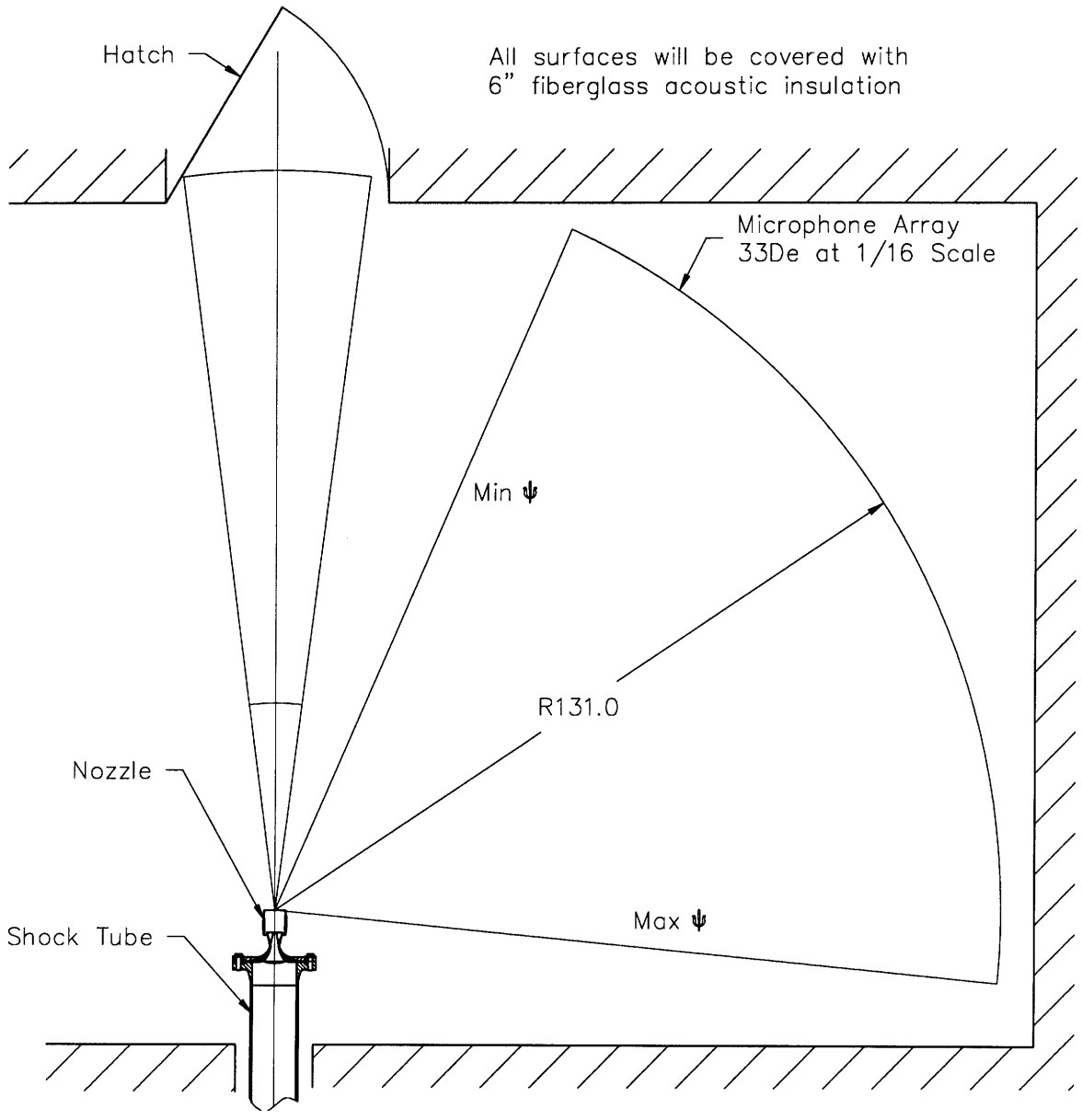

Figure 1-4: Test cell overview of the 8″ vertical shock tube.

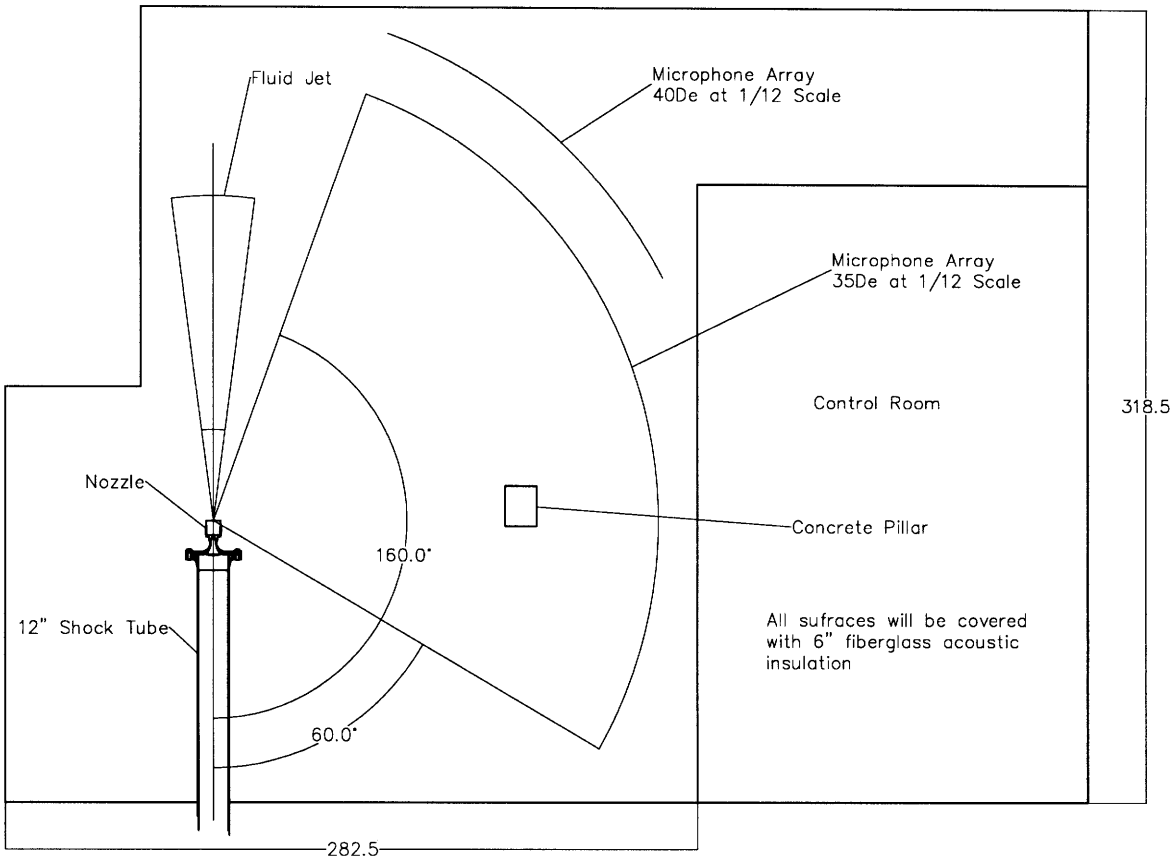

Figure 1-5: Test cell for the proposed 12″ horizontal shock tube

taken over a full range of directivity angles (except for the 15° shadow behind the concrete pillar). There is also space to expand the shock tube to a total length of 60′ and a diameter of 12″. This substantially increases the total test time and provides a sufficient volume test gas to drive the large scale nozzles. Additionally, the driver section can be mounted on rollers and translated horizontally to provide access to the diaphragm, thereby eliminating the need for spur gears and counterweights.

1.5 Thesis Overview

The design and analysis of these two facilities is divided into three sections. Chapter 2 will present a gas-dynamic model of the shock tube, starting with the ideal one-dimensional shock relations then addressing the different viscous and 3-D effects. Gross test times will be evaluated as a function of the design parameters, and the optimum tube geometry will be established based on performance at the HSCT operating point. Chapter 3 will then focus on the generation of a scaled jet using this shock tube. The time required for the jet to reach

a quasi-steady state will be investigated to provide an estimate of the total time available to take data. The radiated acoustics will also be addressed, including the frequency scaling and an uncertainty analysis of the power spectrum measurements. Finally, Chapter 4 will present an overview of the mechanical design for the 8″ vertical shock tube and give some suggestions for how this design could be adapted for the 12″ diameter shock tube in the alternate laboratory space.

Chapter 2

Shock Tube Gas-Dynamic Design

The underlying purpose of the shock tube is to generate a reservoir of high temperature, high pressure fluid that can be used to drive flow through a nozzle. By employing different driver gases and tube pressures, a wide range of conditions can be achieved. The trade-off for the mechanical simplicity and versatility of the shock tube is the short duration of the test; the reservoir conditions typically remain constant for only 2 to 20 milliseconds. These short time scales can be overcome with fast signal processing, but sufficient time must be allowed for the jet to start and the system to reach a quasi-steady state. As a result, it is critical to establish the duration of the tests as a function of the tube geometry and general operating parameters.

In this chapter the gas-dynamic behavior and design of shock tubes will be discussed. An ideal one-dimensional fluid dynamic model is employed to establish the shock tube performance as a function of the operating pressures, geometry, gas composition and other design variables. Non-ideal effects are addressed and, where the effects are significant, adjustments are made to the performance predictions. This model is then employed to optimize the geometry over the desired operating range and to provide the basis for the mechanical design.

2.1 The Wave System in a Simple Shock Tube

Figures 2-1 and 2-2 show the time-distance history of the shock and expansion waves that will occur in the shock tube. Initially, the tube is separated into a driver and a driven section by a thin aluminum or Lexane diaphragm. The driven section, region (1), contains the test

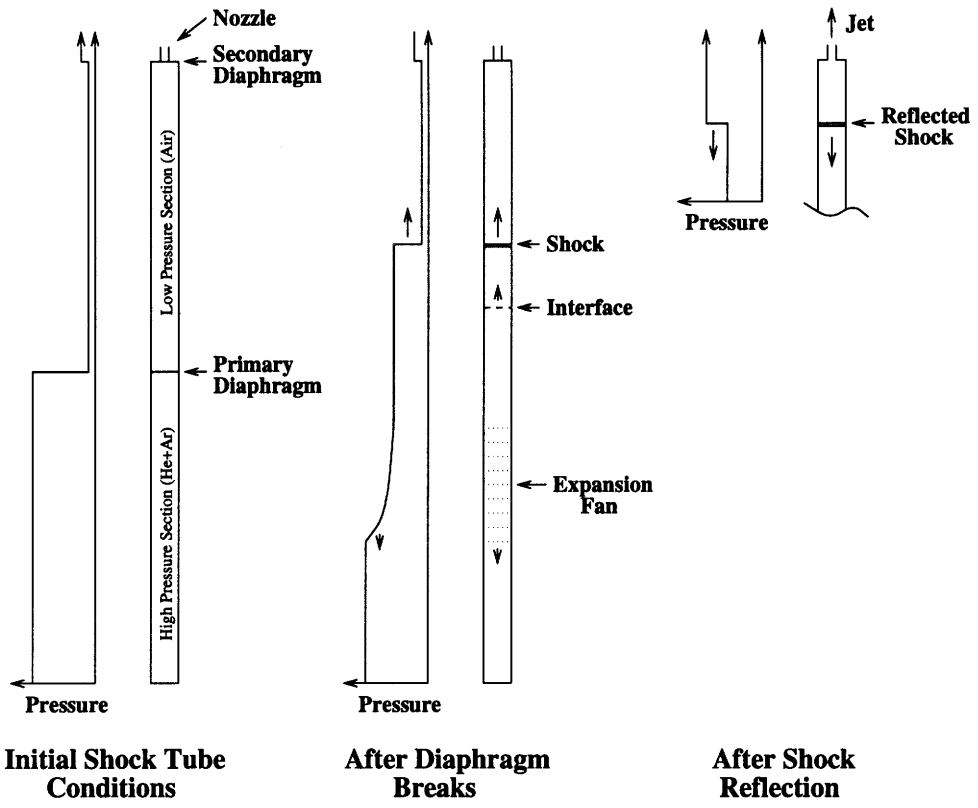

Figure 2-1: Schematic of wave system in shock tube

gas (air) and will typically be evacuated to around 1/10 atmosphere. The driver section, region (4), contains a mixture of helium and argon pressurized from 4 to 40 atmospheres depending on the desired test conditions. When the diaphragm is ruptured the driver gas acts like an impulsively started piston driving the test gas. A shock wave will result, propagating through the test gas, heating and accelerating the fluid. Correspondingly, an expansion fan will propagate through the driver gas decreasing the pressure and accelerating the fluid toward the nozzle. The shock wave will reach the end of the tube, reflect from the end-plate, and create a region of high-pressure, high-enthalpy fluid that can be used as a reservoir to drive the nozzle. The duration of steady flow through the nozzle will be limited by the exhaustion of the test gas or the subsequent arrival of a reflected disturbance at the nozzle. This chapter will highlight the gas-dynamics of the shock tube. A more detailed mathematical description of the flow physics is presented in Appendix A.

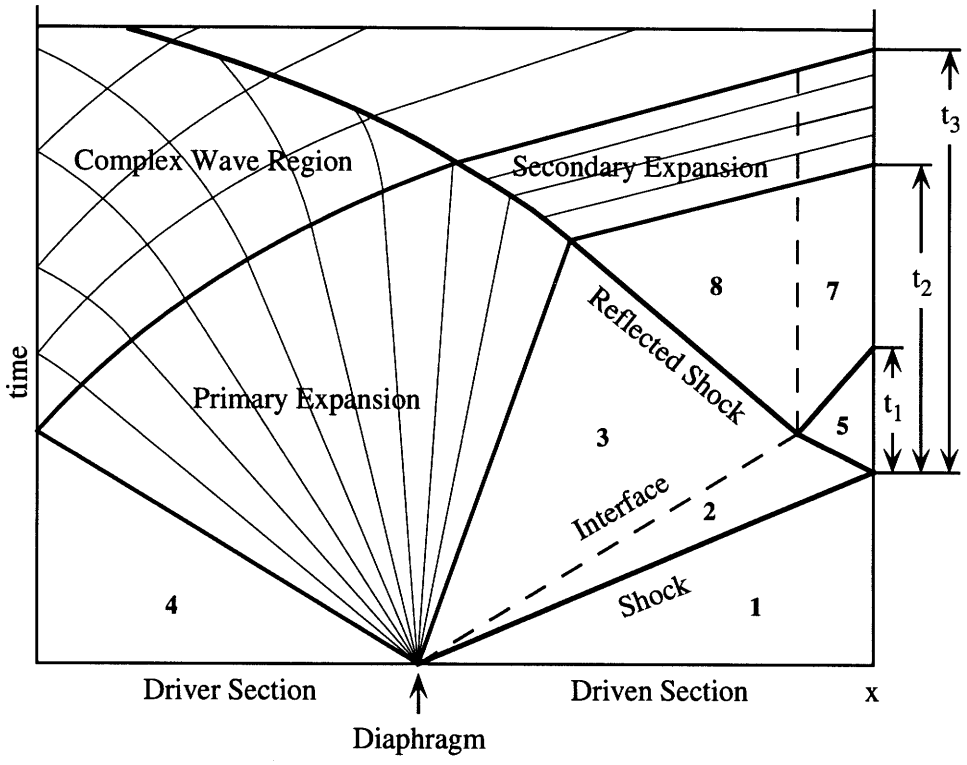

Figure 2-2: Time-distance history of wave system in shock tube

2.1.1 The Shock Tube Equation

The gas-dynamic behavior of the shock tube can be characterized by any one of three dependent parameters: the diaphragm pressure ratio; p_4/p_1, the incident shock Mach number; M_s, and the driver gas composition; χ_{He} (assuming air is used as the test gas). In general, M_s is the most useful parameter for characterizing the shock tube performance because it can be inferred from the shock speed, $c_s = M_s a_1$, which is usually measured directly. Experimental correlations can then be made between M_s and the other two parameters that describe the initial conditions in the tube. It is useful, however, to find an analytical relation between these three parameters in order to establish the required design pressures and shock strength limitations of the facility. This leads to the derivation of the basic shock tube equation.

An idealized one-dimensional model is used to approximate the shock and expansion formation. In this model, the diaphragm is assumed to burst instantaneously, resulting in a "step" discontinuity in pressure at $x = 0$. This discontinuity will resolve into a shock wave propagating into the driven section at a speed c_s and an expansion fan traveling in the opposite direction. Using this simplification, the shock strength, p_2/p_1, and the expansion

strength, p_3/p_4, can be found as a function of the diaphragm pressure ratio. This results in the basic shock tube equation: [14]

$$\frac{p_4}{p_1} = \frac{p_2}{p_1}\left[1 - \frac{(\gamma_4 - 1)(a_1/a_4)(p_2/p_1 - 1)}{\sqrt{2\gamma_1}\sqrt{2\gamma_1 + (\gamma_1 + 1)(p_2/p_1 - 1)}}\right]^{\frac{-2\gamma_4}{\gamma_4 - 1}} \tag{2.1}$$

where the expansion strength can be obtained from

$$\frac{p_3}{p_4} = \frac{p_3}{p_1}\frac{p_1}{p_4} = \frac{p_2/p_1}{p_4/p_1}. \tag{2.2}$$

There are two distinct regions between the shock wave and the expansion tail. There is a region of hot driven gas (2) that has been traversed by the shock, and a region of cold driver gas (3) that has been accelerated by the expansion. To simplify the analysis, there is assumed to be no mixing of these two gases such that a distinct *contact surface* is maintained at their interface. With the strength of the shock and expansion known, the flow quantities in each of these regions can be derived from the normal shock relations. A complete derivation of the gas-dynamic model is presented in Appendix A.

In actual shock tubes, the diaphragm bursting process is highly three-dimensional and requires a finite period of time for the diaphragm to fold out of the flow. As a result, there will not be a distinct shock front, but rather an irregular distribution of compression waves. These waves, however, will overtake each other as they travel downstream, resulting in a steepening compression front. Within a few tube diameters, the waves coalesce into a distinct shock front and exhibit close agreement with the idealized model[7].

2.1.2 Shock Reflection

Reflection from a Rigid End-Plate

When the shock reaches the end-plate it will be reflected, leaving behind a region of high-temperature fluid (region 5) that can be used as a reservoir to drive flow through a nozzle. Due to the short test duration, it is impractical to measure the reservoir temperature directly, so it will need to be deduced from the incident shock speed. In the case of a solid end-plate, the reservoir conditions can be found by assuming perfect shock reflection. In

this case, the reflected shock Mach number is

$$M_r = \frac{1}{M'_{2(s)}} \tag{2.3}$$

where $M'_{2(s)}$ is the Mach number of the fluid in region (2) relative to the incident shock. The pressure and temperature in the reservoir can then be related to M_s by the following relations:

$$\frac{T_5}{T_1} = \frac{[2(\gamma_1 - 1)M_s^2 + (3 - \gamma_1)]\,[(3\gamma_1 - 1)M_s^2 - 2(\gamma_1 - 1)]}{(\gamma_1 + 1)^2 M_s^2} \tag{2.4}$$

$$\frac{p_5}{p_1} = \left[\frac{2\gamma_1 M_s^2 - 1(\gamma_1 - 1)}{(\gamma_1 + 1)}\right]\left[\frac{(3\gamma_1 - 1)M_s^2 - 2(\gamma_1 - 1)}{(\gamma_1 - 1)M_s^2 + 2}\right] \tag{2.5}$$

These conditions will remain constant until the arrival of a reflected disturbance.

A shock reflecting from an end-plate with a small nozzle will exhibit almost identical behavior to a perfect shock reflection provided that the nozzle throat area is small compared to the tube cross sectional area, i.e. $A^*/A_{st} < 0.05$. However, for large area ratios, the presence of the nozzle will have a significant effect[2].

Reflection from an End-Plate with a Nozzle

The presence of a nozzle can effect the parameters behind the reflected shock. Immediately after the shock reflects, there will be a complex system of unsteady rarefactions resulting from the nozzle starting process[2]. This results in a distortion of the reflected front and a highly three-dimensional flow. After the nozzle start-up process is complete, however, a steady-state pattern is approached which can be described by a simple one-dimensional model[24].

In order to solve for the reflected shock strength, it is first necessary to establish the fluid Mach number in the reservoir. Using a 1-D nozzle analysis, it can be shown that the drift Mach number, M_5, is only a function of γ_1 and the nozzle area ratio:

$$M_5 = \left[1 + \frac{\gamma - 1}{2}\right]^{-\frac{\gamma+1}{2(\gamma-1)}} \left[\frac{\rho_{t_5}}{\rho_5}\right]\left[\frac{T_{t_5}}{T_5}\right]^{\frac{1}{2}}\left[\frac{A^*}{A_{st}}\right] \tag{2.6}$$

where $\frac{\rho_t}{\rho}, \frac{T_t}{T} = f(\gamma, M_5)$.

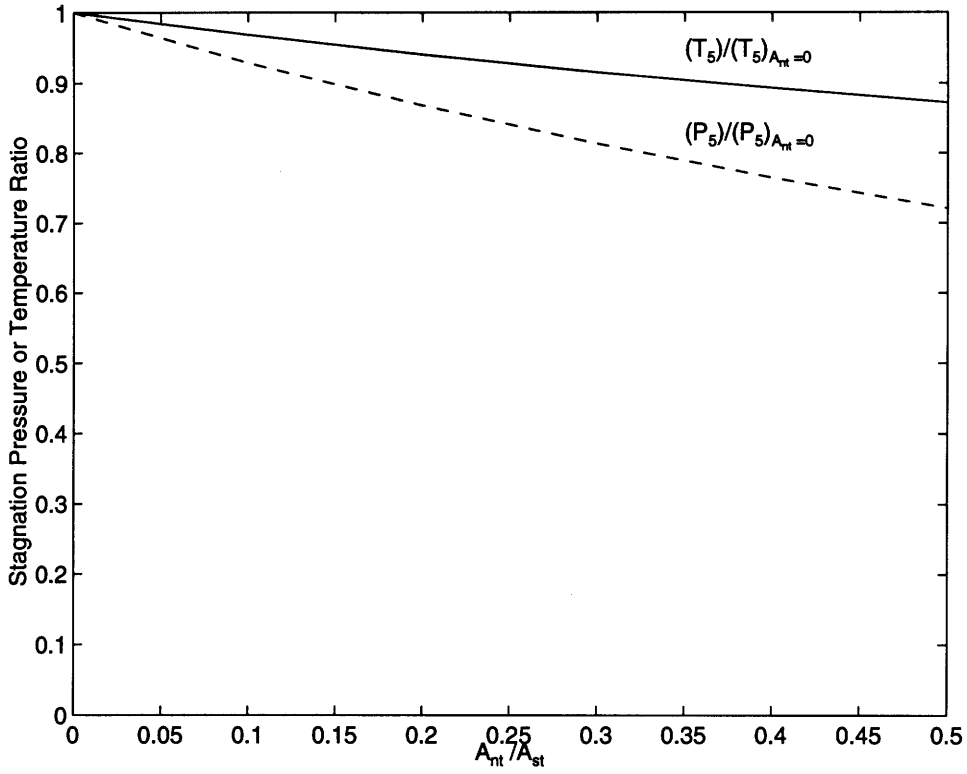

Figure 2-3: Incomplete shock reflection due to massflow through nozzle. Typical nozzle area ratios will range from $A^*/A_{st} = 0.05$ to 0.20. $M_s = 2.28$

The reflected shock Mach number, M_r, can now be found from the expression for the velocity change across a normal shock.

$$\frac{\Delta u}{a_2} = M_2 - M_5 \frac{a_5}{a_2} = \frac{2}{\gamma_1 + 1}\left[M_r - \frac{1}{M_r}\right] \tag{2.7}$$

It is important to note that M_r is defined as the Mach number of the fluid in region (2) (of Figure 2-2) relative to the standing reflected shock wave.

Figure 2-3 shows the effect of incomplete shock reflection for a typical operating condition. The effect on reservoir pressure is of little consequence because it will be measured directly. Stagnation temperatures, on the other hand, are typically inferred from the incedent shock speed, c_s. If an ideal reflection is assumed for large nozzles, $A^*/A_{st} > 0.1$, the derived temperature will be significantly in error ($T_t/T_{t_{ideal}} \approx 0.89$ for $A^*/A_{st} = 0.25$) [10]. The changes from the ideal reservoir conditions shown in Figure 2-3 are only a weak function of incident Mach number.

2.1.3 Interface Tailoring

As the reflected shock moves from region (2) to region (3) (see Figure 2-2), there will typically be a change in shock strength and a reflected shock or expansion. This reflected disturbance will quickly arrive at the nozzle, changing the reservoir conditions and limiting the test time. This reflection, however, can be eliminated if the conditions on each side of the interface are carefully matched so that the reflected shock strength is unchanged as it crosses the contact surface. This "tailoring" of the interface requires that

$$\frac{\gamma_2}{a_2^2}\left[(\gamma_2+1)\frac{p_5}{p_2}+\gamma_2-1\right]=\frac{\gamma_3}{a_3^2}\left[(\gamma_3+1)\frac{p_5}{p_2}+\gamma_3-1\right] \tag{2.8}$$

This equation can be satisfied if a mixture of helium and argon is employed as the driver gas. This allows for a variable mass-averaged molecular weight in the driver, and, as a consequence a variable speed of sound. For any given reflected shock strength, p_5/p_2, there will be a unique driver gas pressure and He/Ar mixture that will satisfy the tailoring condition.

This relation assumes that the flow in the shock tube behaves ideally. As a result, the test conditions calculated in Equation 2.8 are only approximate. In practice, tailoring is achieved by systematically varying the shock speed and analyzing the reservoir pressure traces. If the tailoring condition is met, this trace will show a flat-topped plateau. It is important to note, however, that non-tailored operation can produce a similar signature. The multiple reflections between the contact surface and end-plate can result in a quasi-uniform region that is difficult to qualitatively distinguish from the tailored state [1]. The measured reservoir pressures must therefore be checked against that predicted from the incident shock speed.

2.1.4 Interaction of a Shock Wave overtaking an Expansion

If the reflected shock wave is sufficiently strong, it will overtake the expansion tail before encountering the reflected expansion head (see Figure 2-12c). If this is the case, the shock will encounter an adverse pressure gradient as it passes through the expansion fan. This strengthens the shock and creates a weak secondary expansion that will arrive at the nozzle ahead of the primary expansion. Typically the variation of temperature and pressure across this expansion will be small, $p_9/p_8 < 0.95$ and $T_9/T_8 < 0.98$. However, jet noise is very

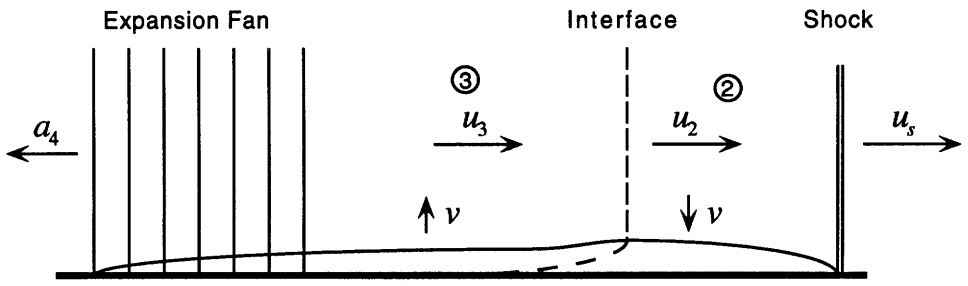

Figure 2-4: Effect of boundary layer growth on shock tube flows.

sensitive to changes in reservoir temperature. For an unshrouded supersonic nozzle, the exit velocity $u_p \sim \sqrt{T_{t_5}}$ and the noise power $P \sim u_p^8/T_{t_5}^{5/2} \sim T_{t_5}^{3/2}$. An 8% drop in reservoir temperature would therefore reduce the radiated noise by approximately 1 dB.

2.2 Boundary Layer Effects

The one-dimensional gas dynamic analysis of a perfect fluid presented in Section 2.1 is useful for providing a first estimate of shock tube performance. However, in real shock tubes there are viscous, thermal, and three-dimensional effects that have a significant impact on performance. The most significant of these is the unsteady growth of a boundary layer in the fluid accelerated by the shock. The generation of this boundary layer results in the attenuation of the shock, axial and transverse flow non-uniformities, acceleration of the free-stream, shock curvature, reflected shock bifurcation, and a general reduction of the test time [23].

The fluid between the expansion head and the shock wave has been accelerated from rest to a velocity u_2. As a result, there will be an unsteady boundary layer growing in this region. The maximum boundary layer thickness will occur somewhere between the diaphragm and the contact surface, and will be reduced to $\delta = 0$ at the wave fronts as shown in Figure 2-4.

The presence of this boundary layer has a number of effects on the shock tube flow. The axial velocity, for instance, will no longer be uniform due to the restriction in flow area. More significantly, there will be a positive radial velocity, v, in region (2) producing the same effect as if the tube diameter were expanding. This generates weak pressure waves that overtake and attenuate the shock [22]. An estimate of the boundary layer thickness was made to determine the magnitude of these effects.

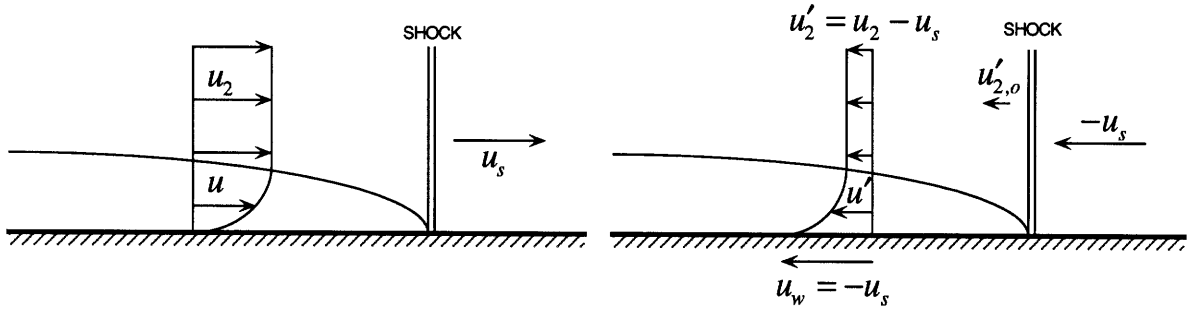

(a) Laboratory reference frame

(b) Shock stationary reference frame

Figure 2-5: Boundary layer approximated as steady flow over a semi-infinite flat plate through change of reference frame

2.2.1 Boundary Layer Model

The boundary layer is difficult to analyze due to the unsteady nature of the problem. However, if a shock stationary reference frame is adopted then the problem can be approximated as a steady boundary layer growing on a moving semi-infinite flat plate, as shown in Figure 2-5. This model requires that the boundary layer be thin compared to the shock tube diameter. If this is the case, than a number of simplifying assumptions can be made:

- The pressure perturbations associated with the unsteady boundary-layer growth can be ignored
- The shock attenuation can be neglected, and the inflow conditions (T_2,p_2,v_2) can be assumed to be uniform
- The free stream velocity, v_2, is independent of x; this requires $\delta^* \ll D_{st}$.
- Locally, the curved tube wall can be approximated as a flat plate.

The Reynolds number can be defined as

$$Re \equiv \frac{\rho_w u_2 x}{\mu_w \left(\frac{u_s}{u_2} - 1\right)} \tag{2.9}$$

where the characteristic velocity is taken to be u_2, the difference in velocity between the free stream and the wall. Similarly, the characteristic distance is taken to be $x\left(\frac{u_s}{u_2} - 1\right)$ which is the distance any particle at a position x will have traveled since the passage of the shock.

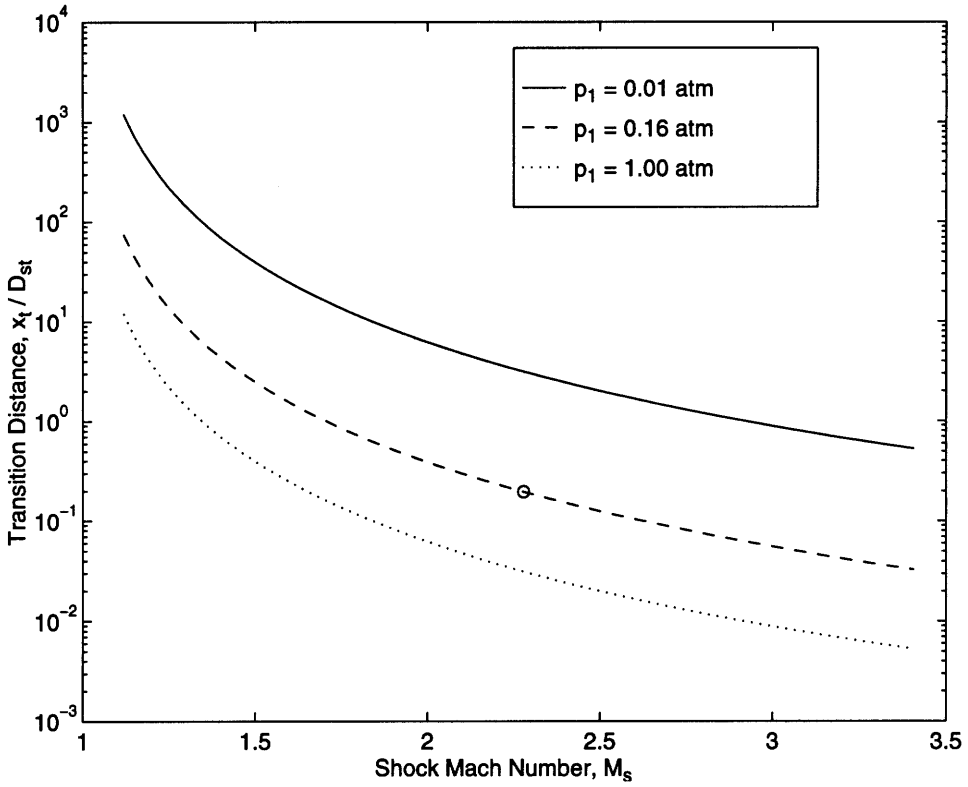

Figure 2-6: Distance between shock and turbulent boundary layer transition point as a function of shock Mach number, M_s. Circle denotes typical HSCT operating point, $p_5/p_0 = 3.7$, $T_5/T_0 = 3.0$. $Re_t = 4 \times 10^6$.

Boundary layer transition occurs in the range $5 \times 10^5 \leq Re_t \leq 4 \times 10^6$ for $1 \leq M_s \leq 9$ [9]. Figure 2-6 presents the location of the transition point as a function of shock Mach number. The flow will become turbulent a short distance behind the incident shock, $x_t \approx 5$ cm, at the facility design conditions, so a fully turbulent boundary layer model can be adopted. This will be a valid model for test conditions characteristic of gas turbine engine nozzles. However, if low tube pressures, $p_1 < 0.05$ atm, and relatively weak shocks, $M_s < 2.0$, are employed, a substantial length of the boundary layer will be laminar (see Figure 2-6) and the fully turbulent model will no longer be valid.

The details of the turbulent boundary layer model are presented in Appendix B. The velocity profile was assumed to follow a power-law distribution, and the thermal boundary layer was defined using the Crocco-Busemann relation. The boundary layer thickness and wall shear forces were found using the Blausius relation for compressible turbulent flow over a semi-infinite flat plate [7].

Results of these calculations are presented in Figure 2-7 for the facility design conditions. The boundary layer model has been demonstrated to agree with experimental data to within

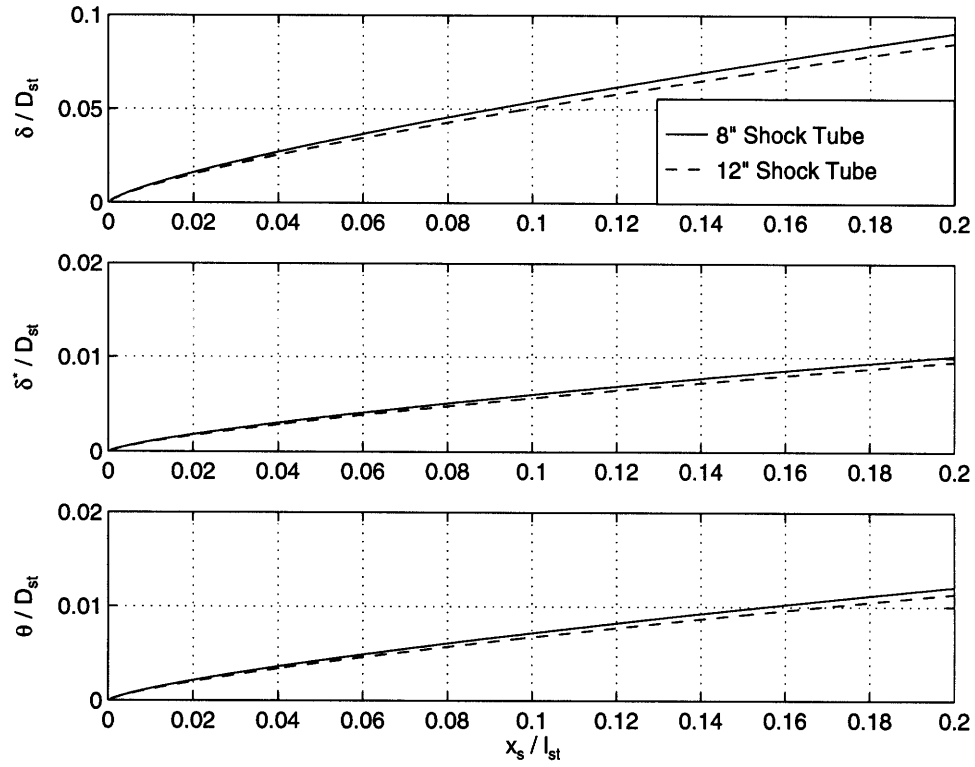

Figure 2-7: Boundary layer parameters in driven section for 8″ and 12″ shock tube facilities; $M_s = 2.28$, $p_1 = 0.15$ atm.

approximately 15% over this operating range [19]. As a general trend, the boundary layer effects will become more severe as the length-to-diameter ratio of the shock tube is increased and the initial driven section pressure is reduced.

2.2.2 Shock Attenuation

The attenuation of the initial shock wave can be predicted by modeling the boundary layer as a distribution of mass sources along the wall of the tube. The pressure perturbations can then be integrated along the characteristic lines to find the variation in shock strength [23]. These calculations, however, are cumbersome, and, for the relatively weak shocks required for this experiment, the attenuation will not be severe. Existing shock tubes with similar geometries and operating conditions realize 90% to 95% of the ideal shock speed [21]. For the purposes of the design, an 8% loss has been assumed. The exact number is not important because the driver pressure can be increased to account for the attenuation. It is important, however, to account for the roughly 25% higher driver pressures that will be required to compenstate for such losses when establishing the maximum pressures in the

facility.

2.2.3 Free Stream Acceleration

The presence of the boundary layer will also cause a reduction in effective flow area and, as a consequence, variations in free-stream velocity. This change in u_2 will not be uniform, but rather a function of δ^* and therefore a function of distance behind the shock. This has the effect of tilting the expansion head toward the nozzle and decreasing the separation between the shock and the contact surface as shown in Figure 2-9.

The variation in free-stream velocity can be estimated using the simplified boundary layer model. The problem is approximated as a steady flow through a contracting duct where the effective diameter is set based on the displacement thickness. This gives an expression

$$\frac{\rho_2 v_2}{(\rho_2 v_2)_o} = \frac{D_{st}}{D_{st} - 4\delta^*} \tag{2.10}$$

where v_2 is the velocity in the shock stationary reference frame. Figure 2-8 shows the results of this calculation transformed into the laboratory frame. It can be seen that the free stream velocity will be increased as much at 10% at the contact surface. This will reduce the shock-interface separation and curve the centered expansion toward the nozzle (see Section 2.2.4).

The coupling between the free stream variations and the boundary layer growth was neglected in this model, so the results are only approximate. A more accurate solution can be found using a local similarity assumption and simultaneously solving for δ and u_2 [22]. However, if the boundary layer is thin compared to the tube diamter, the uniform free-stream model is sufficient.

2.2.4 Influence of Boundary Layer on Time-Distance History

The non-ideal effects associated with the boundary layer will have a strong influence on the time-distance history of the shock tube. Figure 2-9 illustrates qualitative differences between real and ideal behavior based on observations from other shock tubes [23]. Some of the differences result from the finite diaphragm bursting times and the non-uniformity of the free stream due to boundary layer growth. However, the most significant changes are a

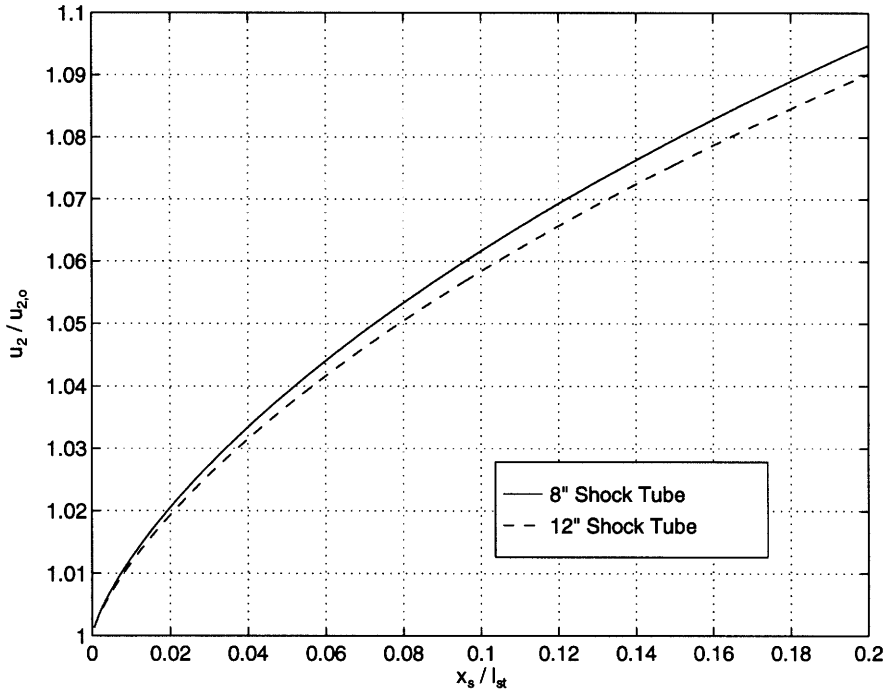

Figure 2-8: Variation in free stream velocity due to boundary-layer growth behind the shock for the 8″ and 12″ shock tubes; $M_s = 2.28$, $p_1 = 0.15$ atm.

consequence of the shock attenuation.

The shock will not follow a straight line on the wave-map. Initially it will accelerate as the diffuse compression front created by the diaphragm removal coalesces into a discrete shock. The shock will reach a maximum speed several diameters downstream, then slow down as it is attenuated by the weak rarefactions generated by the boundary layer.

As a result, in order to achieve the same reservoir conditions, a higher driver pressure will be required than predicted using the ideal model. This will generate a stronger centered expansion and cause the expansion tail to be tilted toward the nozzle. This, in turn, will cause the reflected shock to overtake the expansion tail at a lower T_5/T_1 than predicted by the ideal model, significantly changing the optimum geometry. This effect can be modeled by evaluating the increase in driver pressure needed to compensate for the shock attenuation, recalculating the strength of the centered expansion using the increased diaphragm pressure ratio, and updating the time-history diagram using the trajectory of the stronger centered expansion. The relative length of the driven section, l_{dn}/l_{st}, should be larger than that predicted in the ideal model to make allowances for this change in gas-dynamic behavior. Assuming a $M_s/(M_s)_{ideal} = 0.92$, roughly a 20% longer driven section is needed.

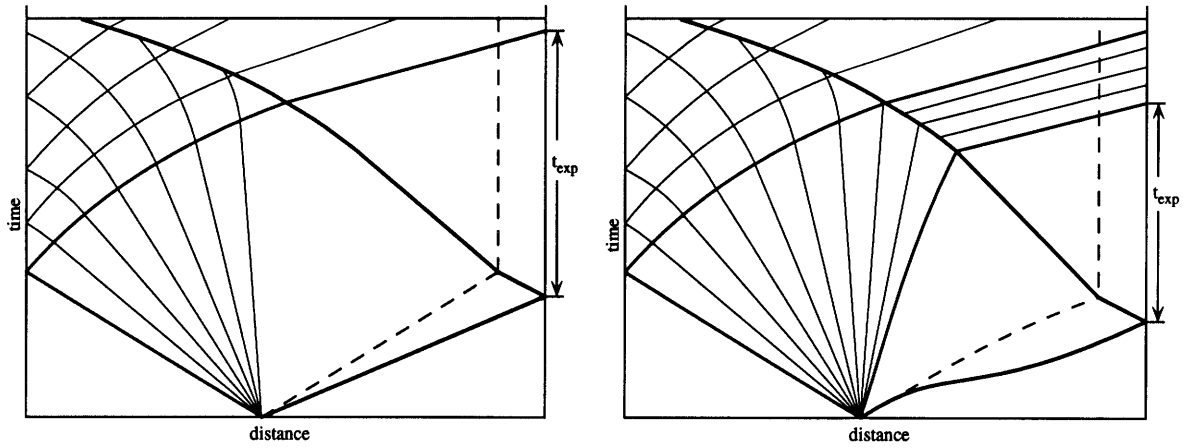

(a) Ideal shock tube flow

(b) Real shock tube behavior

Figure 2-9: Illustration of time-distance histories in real and ideal shock tubes used to generate equivalent reservoir conditions.

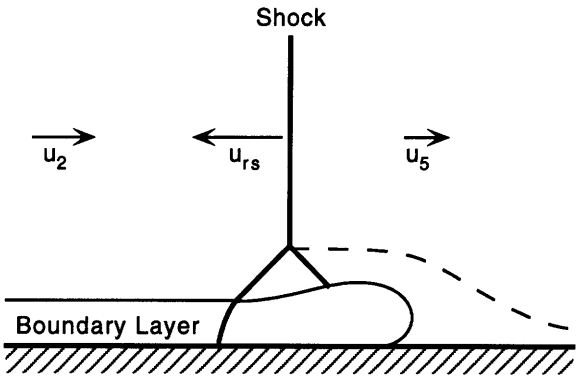

Figure 2-10: Shock Bifurcation Structure for $Re < 900,000$. Figure adapted from Mark [18]

2.2.5 Reflected Shock-Boundary Layer Interaction

After the shock reflects from the end wall, it will encounter the unsteady boundary layer and no longer behave as a simple plane wave. In laminar flows, a strong bifurcation of the shock has been observed in the region close to the shock tube walls as shown in Figure 2-10 [18]. This oblique shock structure leads to non-uniform heating across the test section and, more importantly, the mixing of driver and driven gases as the shock crosses the contact surface. This contaminates the test gas with the cold driver fluid and reduces the total test time.

In turbulent flows this effect is much less severe. The increased transport of energy from the main stream eliminates the conditions in the low-energy laminar boundary layer that lead to shock bifurcation. As a result, it is necessary to establish whether the reflected

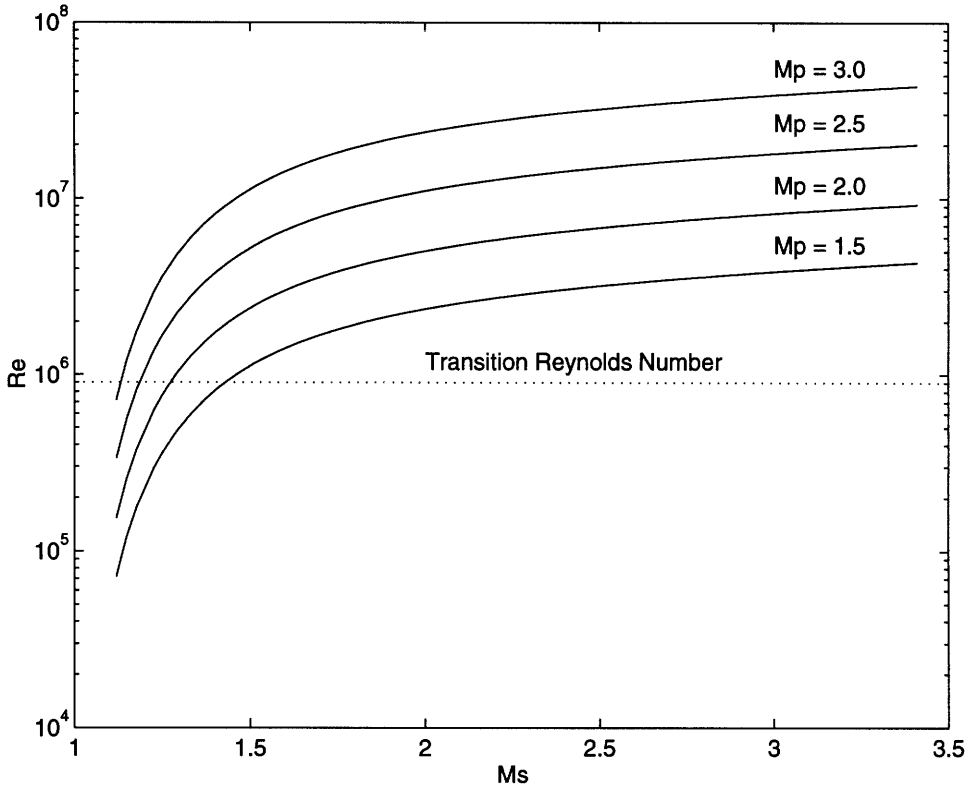

Figure 2-11: Reynolds number at point of shock-interface interaction.

shock will be interacting with a laminar or turbulent boundary layer when it crosses the contact surface.

Turbulence transition was investigated in reference [18] using a series of Schlieren photographs. It was found that the shock bifurcation structure disappeared for Reynolds numbers over 9×10^5 where

$$Re \equiv \frac{\rho_w u_2 x}{\mu_w} \left(\frac{u_2}{u_s} + \frac{u_2}{u_{rs}} \right) \tag{2.11}$$

From Figure 2-11 it can be seen that shock bifurcation will only be expected for low initial tube pressures ($p_1 < 0.07\ atm$) or weak shocks ($M_s < 1.5$). It should be noted, however, that the transition Re cited in reference [18] was based on limited data and is not necessarily representative of all shock strengths; experiments were conducted at $M_s = 2.15$. Mixer/ejector experiments in this facility will be conducted with shock Mach numbers close to this value, ranging from $2.00 < M_s < 2.25$.

2.3 Duration of Constant Conditions in Reservoir

The duration of constant conditions in the reservoir will be limited by one of two factors; the arrival of a reflected shock or expansion at the nozzle, or the exhaustion of the test gas. In most cases, the arrival of a reflected disturbance will be limiting. However, for large area ratio nozzles ($A^*/A_{st} > 0.08$) or high reservoir temperatures ($T_5/T_o > 4.0$) the volume of test gas will be a greater constraint.

2.3.1 Wave Reflection Limited Test Times

Depending on the operating conditions and the relative lengths of the driver and driven sections, there are three different reflections that can result in the termination of the test. Wave diagrams for each of these conditions are shown in Figure 2-12. Each case is discussed below.

Reflections From Contact Surface

The first disturbance that could potentially end a test results from the interaction of the shock with the contact surface (see Section 2.1.3). This is shown schematically in Figure 2-12a. In this case, as is shown in Figure 2-13, test times will typically be in the range of $\tau_{exp} = \tau_1 \approx 2$ to 3 milliseconds. This test time is insufficient for jet noise experiments as the fluid jet will not have time to reach a quasi-steady state (see Section 3.3). Therefore reflections from the contact surface must be eliminated through tailoring of the driver gas as discussed in Section 2.1.3.

Primary Expansion Head

The second situation is shown in Figure 2-12b. The head of the primary expansion fan will travel the length of the driver section, reflect from the end-wall, and propagate back to the nozzle. This is a strong wave and will rapidly reduce the reservoir pressure and temperature once it arrives. In this case, test times are in the range $\tau_3 \approx 14$ to 20 milliseconds as shown in Figure 2-13. The arrival of the expansion head can be delayed by increasing the relative length of the driver section, l_{dr}/l_{st}. However, the driven section must remain long enough to insure a sufficient volume of test gas and to prevent the shock from overtaking the expansion tail.

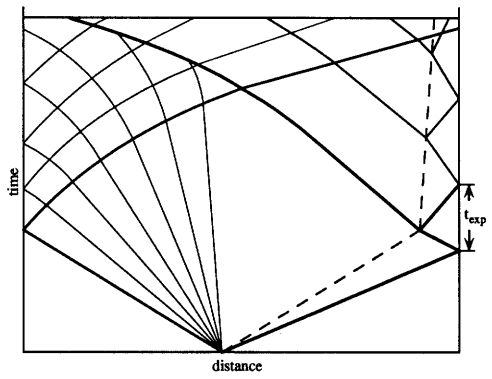

(a) Test time limited by reflection off interface

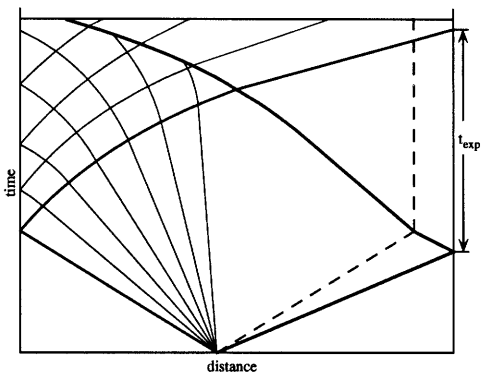

(b) Test time limited by primary expansion

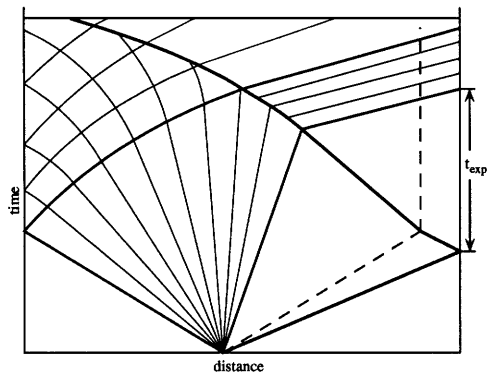

(c) Test time limited by secondary expansion

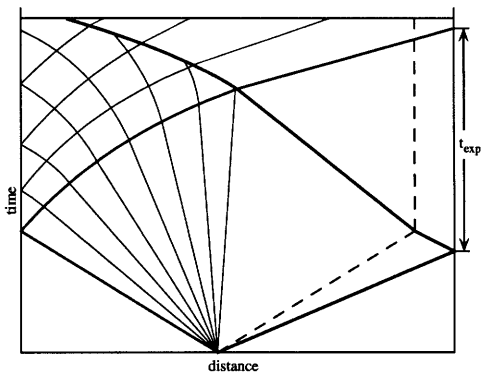

(d) Optimum shock tube geometry at given T_5/T_1

Figure 2-12: Expansion wave limited test times.

Disturbance From Shock-Expansion Interaction

If the reflected shock overtakes the expansion tail as shown in Figure 2-12c, a weak secondary expansion is created that will arrive at the nozzle ahead of the primary expansion. This generally occurs at high reservoir temperatures where stronger shocks are required to generate the necessary temperature rise. Figure 2-13 shows the ideal arrival times of the different reflected disturbances for the shock tube. It can be seen that the secondary expansion will only be limiting for $T_5/T_1 > 4.3$. The temperature ratios at which the shock overtakes the expansion tail can be increased by increasing the relative length of the driven section, l_{dn}/l_{st}.

Optimization

The test time can be maximized for any given T_5/T_1 and total tube length by setting the relative lengths of the driver and driven sections. This maximum will occur when the reflected shock, expansion head, and expansion tail all intersect at a common point as shown in Figure 2-12d. Figure 2-14 illustrates how the shock tube lengths can be optimized for a given reservoir temperature ratio. The test time drops off sharply above the optimization point so the section lengths should be set based on the highest temperature in the design range. It should also be noted that the presence of a boundary layer will have a significant effect on the optimization point. A stronger expansion will be required that will tend to result in a shock-expansion interaction at a lower T_5/T_1 than predicted in the ideal model (see section 2.1). A $l_{dn}/l_{st} = 0.46$ was selected for optimum performance in the $2.5 < T_5/T_1 < 3.0$ range.

2.3.2 Test Gas Exhaustion Limited Test Times

In the cases where there is a high massflow through the nozzle the depletion of the test gas can become limiting. This is generally the case when testing large nozzles ($A^*/A_{st} > 0.10$) or at high reservoir temperatures ($T_5/T_0 > 3.0$). A rough estimate of the time to exhaust the test gas is $t_{ex} = \rho_1 l_{dn} A_{st}/\dot{m}_n$ where $\rho_1 l_{dn} A_{st}$ is the total mass of test gas. Substituting in Equation A.12 for the nozzle massflow gives the expression

$$t_{exg} = \left[1 + \frac{\gamma_1 - 1}{2}\right]^{\frac{\gamma_1+1}{2(\gamma_1-1)}} \left[\frac{T_5}{T_1}\right] \left[\frac{p_5}{p_1}\right]^{-1} \left[\frac{A_t}{A_{st}}\right]^{-1} \left[\frac{l_{dn}}{a_5}\right] \tag{2.12}$$

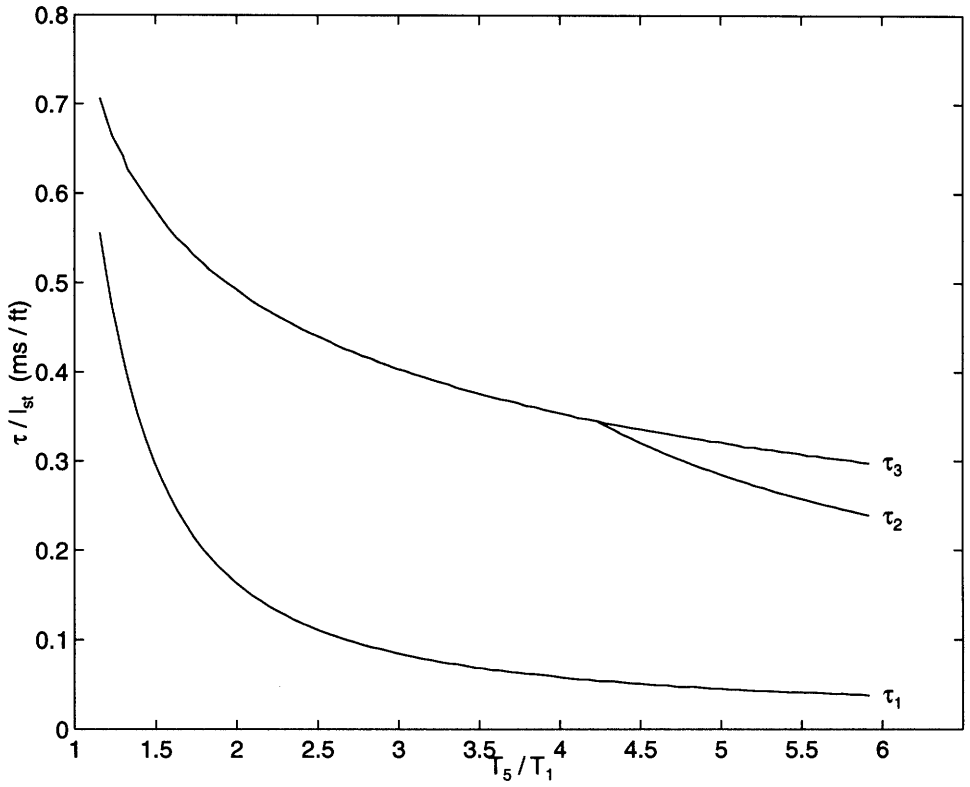

Figure 2-13: Expansion limited tests time per unit shock tube length (ms/ft) as a function of reservoir temperature ratio, T_5/T_1. τ_1 is the test time limited by reflection from the interface, τ_2 the test time limited by the secondary expansion, and τ_3 the test time limited by the primary expansion (see Figure 2-12). $l_{dn}/l_{st} = 0.46$.

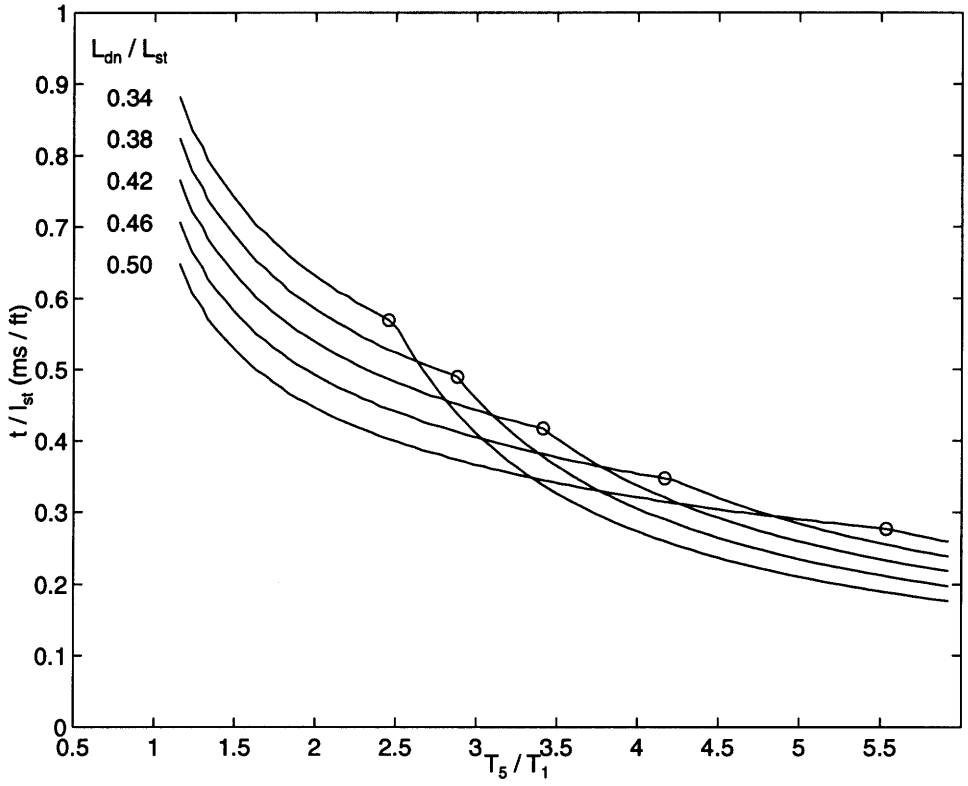

Figure 2-14: Expansion limited test times per unit shock tube length (ms/ft) for various size driven sections, l_{dn}/l_{st}. $t_{exp} = min(\tau_2, \tau_3)$. Circles indicate the optimum operating point for each geometry, i.e. the maximum possible test time per unit length for a given reservoir temperature.

It should be noted that p_5/p_1 and T_5/T_1 can be related by Equations 2.4 and 2.5 so that the ideal time to exhaust the test gas becomes a function of the required reservoir temperature, T_5, and the driven section geometry. The results of this calculation are presented in Figure 2-15. The facility is designed for nozzle throat area ratios in the range of $0.04 \leq A^*/A_{st} \leq 0.10$, so t_{exg} will be 1.4 to 3.0 times larger than the expansion limited test times at typical operating temperature ratios, $2.0 < T_5/T_1 < 3.0$.

In practice, the contamination of the test gas with the cold driver fluid will reduce the total test times. Three-dimensional effects during diaphragm bursting will result in a "contact zone" rather than a distinct contact surface. Similarly, when the shock impinges on the interface, Richtmyer-Meshkov instabilities can result that will further mix the two gases. More importantly, if the shock is bifurcated as it crosses into region (3), as is illustrated in Figure 2-10, a cold jet of driver fluid will be created close to the wall. This will arrive at the nozzle, prematurely ending the test.

The above model is only an upper bound on the test gas exhaustion limited test time. It is difficult to assess how much of this time will actually be realized. While shock bifurcation, the primary mechanism of test gas contamination, can be predicted using the correlation presented in Section 2.2.5, it will not occur for the design test conditions. The secondary mechanisms, however, cannot be easily modeled so it was conservatively assumed that no more than 60% to 70% of the ideal test gas exhaustion time would actually be realized.

2.4 Gas-Dynamic Performance and Design

The performance analysis of the shock tube can be divided into two parts. First, the various gas-dynamic parameters (pressure, temperature, shock speeds, driver gas composition, etc.) can be related using the analytical models presented in the previous two sections. Second, the time-distance history of the shock tube can then be generated for any given operating point and tube geometry. From this, the test times can be estimated and the tube geometry optimized for the desired set of reservoir conditions.

2.4.1 Establishing Gas-Dynamic Performance Curves

The models presented in Section 2.1 can be used to relate the different gas parameters and give some measure of shock tube performance. Perhaps the most useful set of correlations

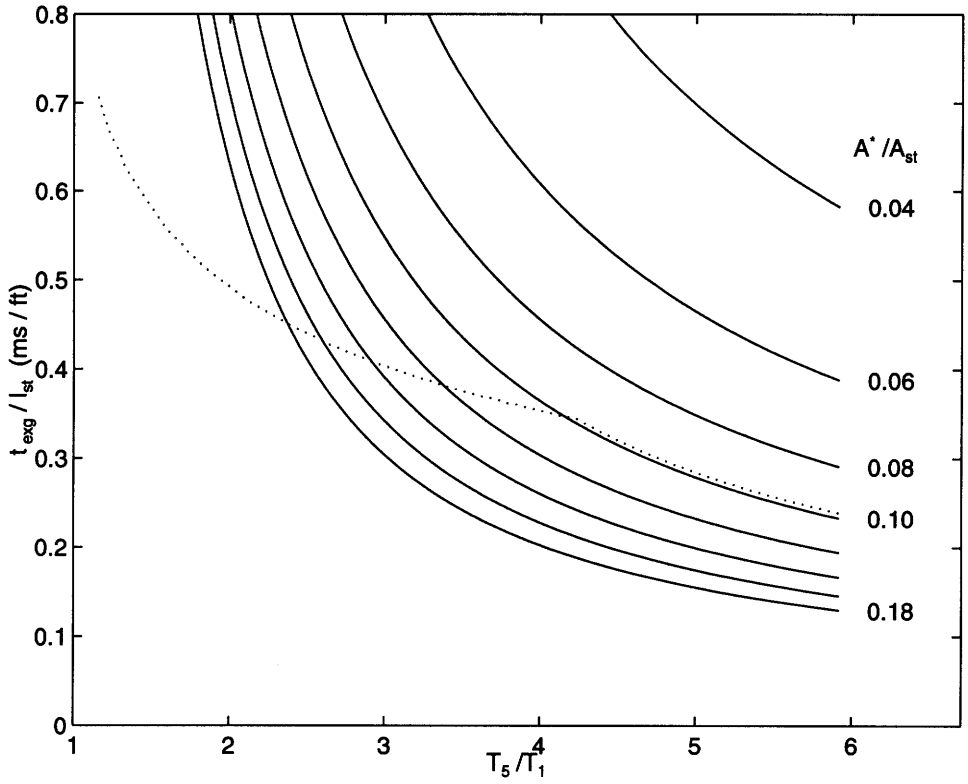

Figure 2-15: Ideal time to exhaust test gas, t_{exg}/l_{st}, for various A^*/A_{st}. Dotted line refers to reflected expansion limited test time. $l_{dn}/l_{st} = 0.46$

connect M_s and the reservoir pressure and temperature rise (p_5/p_1, T_5/T_1). The shock speed will be measured directly during the experiments so, given the initial condition of the driver gas, these relations can be used to infer T_5 and p_5. This is particularly important for the reservoir temperature which is difficult to measure directly due to the short timescales.

Figure 2-16 shows the relation between M_s and the reservoir pressure and temperature rise based on the ideal model. Curves are presented for both a solid end-plate, $A^*/A_{st} = 0$, and the largest nozzle that will be employed, $A^*/A_{st} = 0.1$. It is important to note that the shock Mach number will not be constant along the length of the tube due to diaphragm bursting effects and shock attenuation (see Section 2.2.2). These relations are based on the value of M_s immediately before the shock reflects from the end-plate. Using this value for M_s these correlations have historically shown excellent agreement with experimental data [7].

These relations establish a number of operating parameters for the shock tube. The driven gas will initially be at ambient temperature, so the desired T_5 will dictate the required shock Mach number. This, in turn, gives the reservoir pressure rise, p_5/p_1. Then, given the

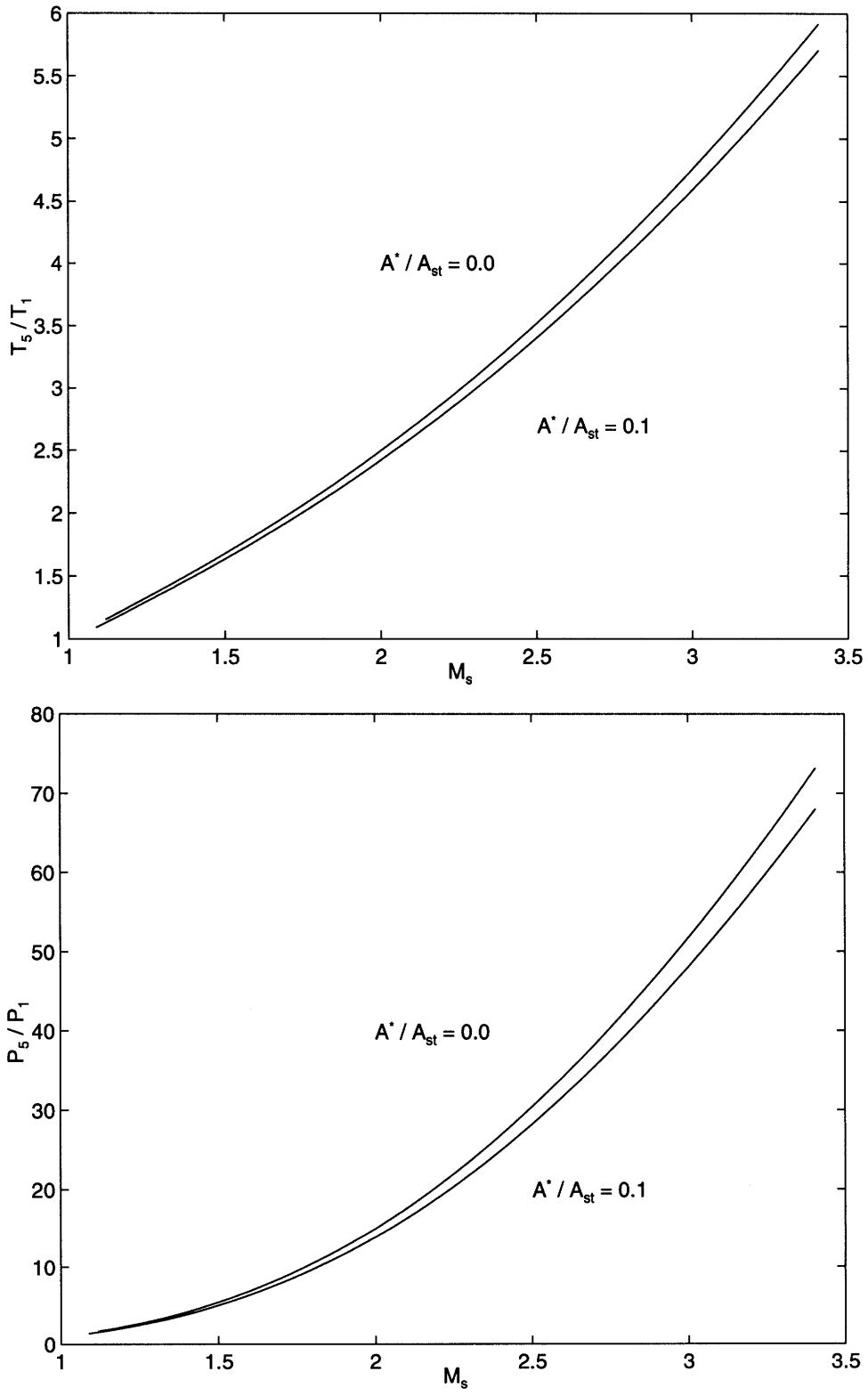

Figure 2-16: Reservoir pressure and temperature rise as a function of incident shock Mach number. Air is used as driven gas.

relation

$$\frac{p_1}{p_0} = \frac{p_5/p_0}{p_5/p_1} \tag{2.13}$$

the initial pressure in the driven section can be found. Thus the shock Mach number and initial state of the driven gas have been established as a function of the desired nozzle pressure ratio, p_5/p_0, and primary jet total temperature.

Correlations can also be made between the diaphragm pressure ratio, driver gas composition, and incident shock strength. This will complete the connection between the initial state of the shock tube and the reservoir conditions. These three parameters can be coupled using the ideal model discussed in Section 2.1. The tube must operate under tailored conditions, so the driver gas composition can be found as a function of M_s using the tailoring equation (Equation 2.8) and the shock reflection relations (Equations 2.6 and 2.7). Next, the basic shock tube equation (Equation 2.1) can be used to relate the diaphragm pressure ratio to the shock Mach number using the tailored driver gas composition. The ideal results are presented in Figures 2-18 and 2-17.

Unfortunately, the incident shock Mach number, M_s, is generally 5% to 10% less than that predicted by the basic shock tube equation. This is predominantly due to the unsteady growth of a boundary layer as discussed in Section 2.2. Therefore, experimental correlations must be made between p_4/p_1, χ_{He}, and the reservoir temperature and pressure that also satisfy the tailoring condition across the interface. For the design, a ratio of $M_s/(M_s)_{ideal} = 0.92$ was assumed to give an estimate of the shock speed as a function of the initial driver pressure. This value for $M_s/(M_s)_{ideal}$ has been observed in shock tubes with similar geometries and operating conditions [21].

Figure 2-17 shows the ideal relation between shock Mach number and driver gas composition that satisfies the tailoring condition. The maximum shock speed is set by the tailoring conditions for a 100% helium driver. This gives $(M_s)_{max} \approx 3.4$, which corresponds to a reservoir temperature of approximately 1750 K.

The incident shock Mach number and diaphragm pressure ratio are related in Figure 2-18. In practice, M_s will be 5% to 10% less than that predicted by the ideal model due to the shock attenuation effects. Experimental correlations will need to be developed that connect these two parameters for this facility. However, to give an estimate of the maximum

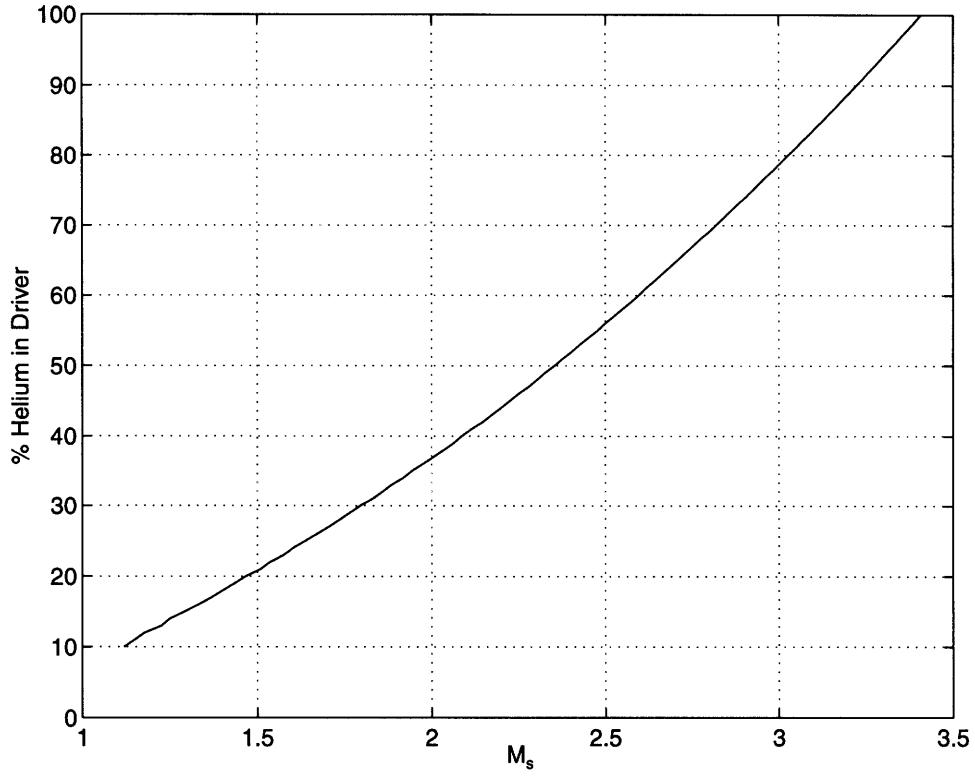

Figure 2-17: Driver composition required to satisfy tailored interface condition. $\%He$ by mass given for $He + Ar$ driver.

reservoir pressure, an 8% loss is assumed. The maximum allowable tube pressure is set by the flanges, $p_{max} = 740\ psig$ for the $8''$ shock tube. So for an initial driver pressure of $p_4 = p_{max}$ a maximum nozzle pressure ratio of $p_5/p_0 = 38$ can be achieved.

2.4.2 Setting Tube Geometry to Optimize Test Time

In contrast to the gas parameters, there is a great deal of flexibility in setting the shock tube geometry. For a fixed total tube length the relative lengths of the driver and driven sections can be varied to maximize the test time at any given operating point, as discussed in Section 2.3.1. However, for the $8''$ vertical shock tube, the total tube length is limited by the available space ($38'$ from sub-basement floor to nozzle) and the section lengths must be set so that diaphragms are accessible. In addition, some thought must be given to the availability of stainless steel tubing. Typical pipe sections come in $240''$ lengths. If longer sections are desired then non-standard length tubing must be obtained or a separate flanged section added; either option may significantly increase costs. Given these constraints, a $246''$ driver ($238''$ tube + $2 \times 4''$ flanges) and a $210''$ driven section were chosen. This is consistent

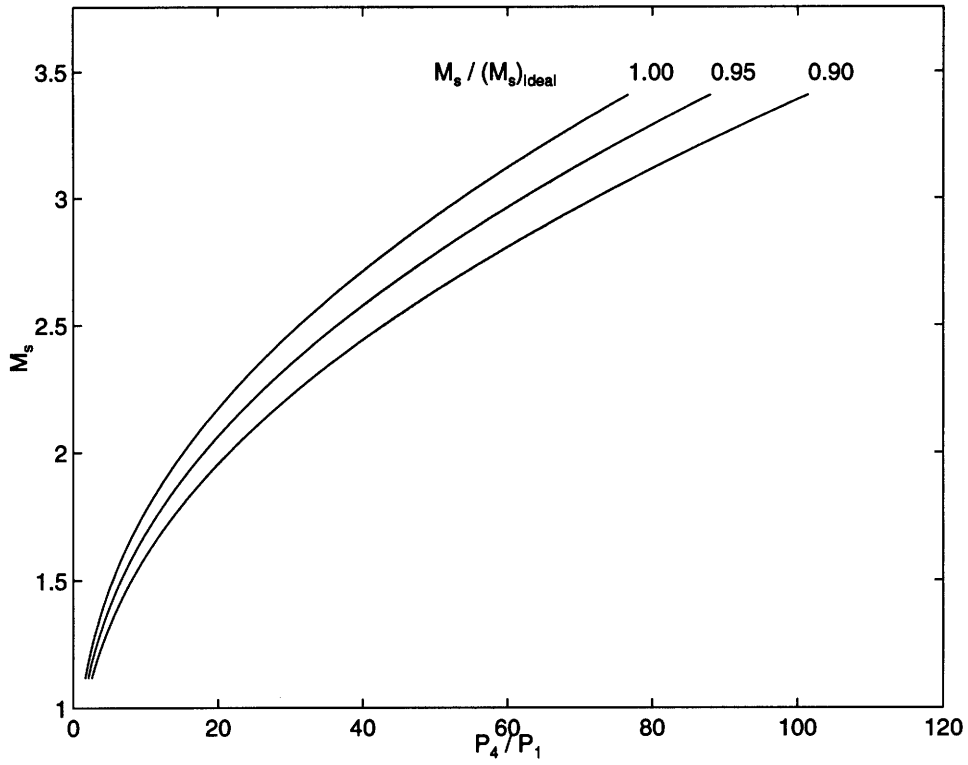

Figure 2-18: Diaphragm pressure ratio required to generate a Mach M_s shock for different shock attenuations.

with the optimum $l_{dn}/l_{st} = 0.46$ found for operation at the facility design conditions. For the $12''$ horizontal shock tube the total tube length can be expanded to $60'$, resulting in optimum driver and driven section lengths of $33.4'$ and $27.6'$ respectively.

Once the tube lengths have been established, the cross sectional area can be set based on the largest nozzle to be tested. As is shown in Section 2.3.2, it is desirable for A^*/A_{st} to be less than 0.10 so that there is near perfect shock reflection and sufficient volume of test gas. This sets the shock tube diameter based on the A^* of the largest nozzle to be tested. For the vertical facility, the maximum size nozzle was selected to be a roughly $1/16^{th}$ scale HSCT mixer/ejector, set based on acoustic measurement constraints which are discussed in the next chapter. The resulting required shock tube diamter is $8''$. It would be desirable to test up to a $1/12^{th}$ scale nozzle in the horizontal facility, which increases the required diameter to $12''$.

2.4.3 Shock Tube Loading

The gas-dynamic model is also a useful tool for predicting the maximum pressures and axial loads seen by the shock tube. For the experiments of primary interest, the pressures will

be moderate. The driver pressure will be approximately 70 psi (4.8 atm) which will result in a maximum axial load of 3,500 lbs (16 kN) for the 8″ tube or 7,900 lbs (35 kN) for the 12″ tube immediately after diaphragm rupture. At the limit pressure, $p_4 = 740$ $psig$, the maximum axial load will be 37,000 lbs (164 kN) and 83,000 lbs (370 kN) for the 8″ and 12″ tubes respectively.

Although the maximum loads can get quite large, the total impulse remains small due to the short duration of the test. For the 12″ shock tube, $\int F dt \approx 52$ $lb \cdot s$ (230 $N \cdot s$ at an $NPR = 3.4$, and $\int F dt \approx 1800$ $lb \cdot s$ (8100 $N \cdot s$) at an $NPR = 27$. Figure 2-19 shows the worst case loading profile. Initially the pressure forces on the end plates are balanced by the pressure forces on the diaphragm. At $t = 0$ the diaphragm is ruptured and, as a result, it no longer imparts any load on the shock tube walls. This results in a strong downward force due to the pressure imbalance between the two end-plates. Once the shock reflects from the end-wall (point (b)) there will be a step increase in pressure at the driven end reducing the net downward force. Similarly, when the primary expansion reaches the driver end (point (c)) the pressure will rapidly decrease, resulting in a net upward force. Finally, when the reflected expansion head reaches the driven end (point (d)) the pressures will quickly reach equilibrium through a series of complex wave reflections and interactions. The loads will go to zero and the test will be complete.

2.5 Gas-Dynamic Design Summary

Tables 2.1 and 2.2 summarize the gas-dynamic performance of the 8″ and 12″ shock tubes at various operating conditions. A more complete analysis of the facility performance will be presented in the next chapter after the generation of the scaled jet has been discussed. For HSCT experiments $T_5/T_0 \approx 2.5$ to 3.0, which correspond to cases A and B in the tables. The shock tube has been optimized for this temperature range, so the expansion-limited test time (t_{exp}) is at a maximum for the given total shock tube lengths. The 8″ facility performs well over this range for nozzle throat diameters up to 2.6″ and the 12″ facility for D^* up to 4.1″. Test gas exhaustion times will be limiting for larger nozzles due to test gas contamination (see Section 2.3.2).

Case C illustrates the maximum reservoir pressure. The reservoir pressure only affects the tube loading and, to some extent, the losses in the tube. The other parameters are

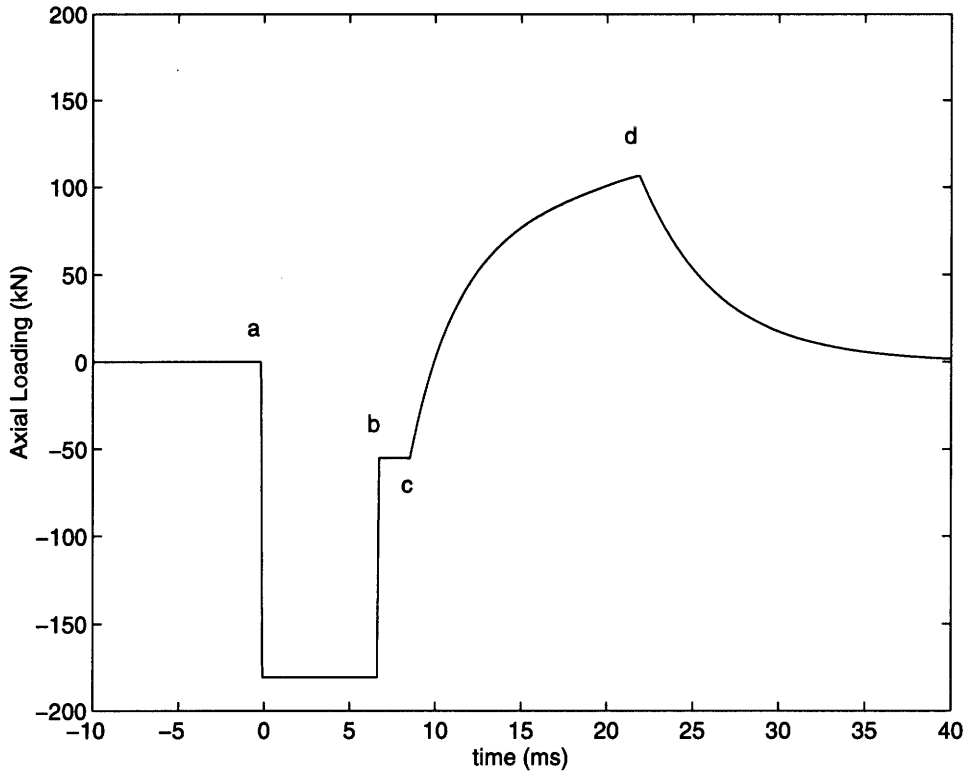

Figure 2-19: Axial loading on floor mounts for a $M = 3$ nozzle with $T_5/T_1 = 3$ and 10% loss in shock Mach number.

	T_5/T_0	p_5/p_0	p_4/p_1	p_5/p_1	M_s	χ_{He}	p_4/p_0	p_1/p_0	F_{max}	t_{exp}	t_{exg}	D^*	A^*/A_{st}
A	3.0	3.4	29.1	21.9	2.25	0.46	4.49	0.15	3300	15.4	30.0	2.1	0.07
											21.0	2.6	0.10
											11.6	3.4	0.18
											8.1	4.1	0.26
B	2.5	3.4	20.2	15.1	2.00	0.37	4.44	0.22	3280	16.7	39.9	2.1	0.07
											27.9	2.6	0.10
											15.5	3.4	0.18
											10.7	4.1	0.26
C	—	37.9	—	—	—	—	—	—	37200	—	—	—	—
D	5.9	3.4	95.8	73.2	3.41	1.00	4.42	0.04	3260	9.1	12.6	2.1	0.07
											8.9	2.6	0.10
											4.9	3.4	0.18
											3.4	4.1	0.26

Table 2.1: Summary of shock tube parameters for the 8″ vertical shock tube. $l_{st} = 38'$, $l_{dn}/l_{st} = 0.46$.

	T_5/T_0	p_5/p_0	p_4/p_1	p_5/p_1	M_s	χ_{He}	p_4/p_0	p_1/p_0	F_{max}	t_{exp}	t_{exg}	D_e	A^*/A_{st}
A	3.0	3.4	29.1	21.9	2.25	0.46	4.49	0.15	7425	27.0	144	2.1	0.03
											108	2.6	0.04
											53.8	3.4	0.08
											35.9	4.1	0.12
B	2.5	3.4	20.2	15.1	2.00	0.37	4.44	0.22	7380	24.8	108	2.1	0.03
											80.9	2.6	0.04
											40.4	3.4	0.08
											27.0	4.1	0.12
C	—	37.9	—	—	—	—	—	—	83700	—	—	—	—
D	5.9	3.4	95.8	73.2	3.41	1.00	4.42	0.04	7335	14.0	45.5	2.1	0.03
											34.1	2.6	0.04
											17.1	3.4	0.08
											11.4	4.1	0.18

Table 2.2: Summary of shock tube parameters for the 12″ horizontal shock tube. $l_{st} = 60'$, $l_{dn}/l_{st} = 0.46$.

functions of the pressure ratios in the tube (p_4/p_1, p_5/p_1, etc) and are not dependent on their absolute value.

Case D shows the maximum temperature possible with a helium-argon driver and air as a test gas. In general, test times are decreased with increasing pressure; expansion limited test times drop almost in half due to stronger shocks and expansions generated in the tube. Similarly, to generate the same reservoir pressure, p_1 must initially be lower than that for weaker shocks to compensate for the larger pressure rise across the shock. This reduces the total mass of test gas and, correspondingly, the test gas exhaustion times.

This completes the description of the shock tube gas-dynamics. The generation of the scaled jet is discussed in the following chapter. The useful test times and range of measurements that can be taken will be established, thereby completing the performance analysis of the facility.

Chapter 3

Generation and Acoustics of the Scaled Jet

As was detailed in the previous chapter, the shock tube can be used to generate conditions analogous to that at the exit of a gas-turbine engine. This provides an inexpensive means to test scaled engine nozzles at elevated temperatures and highly uniform enthalpy. The size of the test nozzles, however, is tightly constrained by the limited volume of test gas and the acoustic measurement requirements. If there is high massflow through the nozzle the driven gas will be depleted rapidly, limiting the test times. In addition, the size of the test cell limits how far the microphones can be placed from the nozzle exit. If the nozzle diameter is large compared to distance to the microphones such that $R_{mic}/D_e < 40$ then the fluid jet will exhibit near-field acoustic behavior, making the noise measurements difficult to interpret. Conversely, the frequency of the radiated noise scales inversely with the nozzle diameter. As a result, small scale nozzles may produce frequencies that are higher than can be easily measured. The scale of the nozzle is therefore a trade-off between these constraints.

The primary limitation of the $8''$ vertical facility is that no single nozzle can be used to characterize all of the noise generation sources for a typical HSCT mixer/ejector nozzle. However, if the noise sources internal and external to the nozzle are investigated separately, the entire range can be covered. This can be accomplished by employing two different scale nozzles:

- $1/16^{th}$ *Scale Nozzle for Internal Mixing Studies:* The noise generated inside the nozzle

ejector shroud will dominate the external mixing noise in the higher frequency range ($f > 1\ kHz$). As a result, at least a $1/16^{th}$ scale nozzle is required to keep these frequencies in the measurable range[1]. Using this scale nozzle, however, will cause the microphones to be in the near-field. This will make the lower frequency external mixing noise measured suspect unless corrections can be made to extrapolate to far-field behavior. These corrections, however, are difficult for complex sources such as fluid jets.

- $1/20^{th}$ *Scale Nozzle for External Mixing Studies:* To alleviate the problems associated with near-field acoustic measurements the nozzle can be made smaller ($1/20^{th}$ scale), ensuring that the microphones will be in the far-field. This will allow the low frequency external mixing sources to be characterized. The high frequency range, however, will be truncated due to high frequency measurement limitations.

The combination of these two nozzles will allow the important internal and external noise sources to be investigated. Alternately, there may be some intermediate scale nozzle that provides a reasonable compromise between the different measurement constraints.

The primary strength of the $12''$ horizontal shock tube facility is that a single nozzle could be used to investigate far-field behavior of both the internal and external noise sources. The larger test cell enables the microphones to be placed farther from the nozzle exit, eliminating the need for near-field corrections on the $1/16^{th}$ scale nozzle. This nozzle could then be used to investigate a wide range of jet noise sources. A $1/12^{th}$ scale nozzle could also be employed, extending the measurable frequency range while maintaining a reasonable distance of $R_{mic}/D_e = 40$ to the microphones to ensure far-field radiation behavior.

In addition to these constraints, the short duration of the test remains the primary limitation of shock tubes. Typically, the reservoir temperature will only remain constant for 10 to 30 ms. This problem is further compounded because a fraction of this time will be required for the nozzle to start and for the jet to develop to a sufficient length. Models will be discussed that predict this start-up time and provide estimates of the time remaining to take measurements. It has been found that sufficient time is available to take fluid mechanic and acoustic measurements for HSCT applications.

[1]Noise measurements assumed to be limited to frequencies under 80 kHz

3.1 Jet Noise Generation and Scaling

3.1.1 The HSCT Nozzle

The facility was optimized to test mixer/ejectors at conditions applicable to the HSCT. For the shock tube design a simple axisymmetric configuration was assumed, but the results will be approximately applicable to rectangular ducts with equivalent areas. The full scale HSCT nozzle was assumed to fit in the following parameter range with geometries and noise generation mechanisms similar to those presented in Figures 3-1 and 3-2:

- Ejector Exit Velocity: $u_e \approx 400$ to 530 m/s (1350 to 1750 ft/s)
- Primary Nozzle Mach Number: $M_p \approx 1.5$ or less
- Primary Nozzle Throat Area: $A^* \approx 0.85\ m^2$ (1320 in^2)
- Secondary/Primary Stream Area Ratio: $A_s/A_p \approx 1.2$
- Ejector Shroud Area Ratio: $A_e/A_m = 0.90$ to 0.95
- Ejector Length/Diameter: $L_e/D_e \approx 3$ where $D_e \equiv \sqrt{\frac{4A_e}{\pi}}$

In general there will be a great deal of flexibility to vary these parameters, but this provides a useful point at which to evaluate the facility performance.

The important acoustic ranges are another critical parameter for sizing the test nozzles. The highest full scale frequency of interest will dictate the smallest scale nozzle that can be used. Similarly, for the 8″ vertical shock tube, the directivity range will set the orientation of the nozzle in the test cell. These requirements were taken to be as follows:

Frequency

The FAA regulates aircraft noise from 50 Hz to 11 kHz. However, due to the frequency weighting for human ear response, the 100 Hz to 5 kHz range is of primary importance for jet noise. Within this range the 1-4 kHz band is weighted the most heavily [28] and is considered critical for mixer/ejector performance [33].

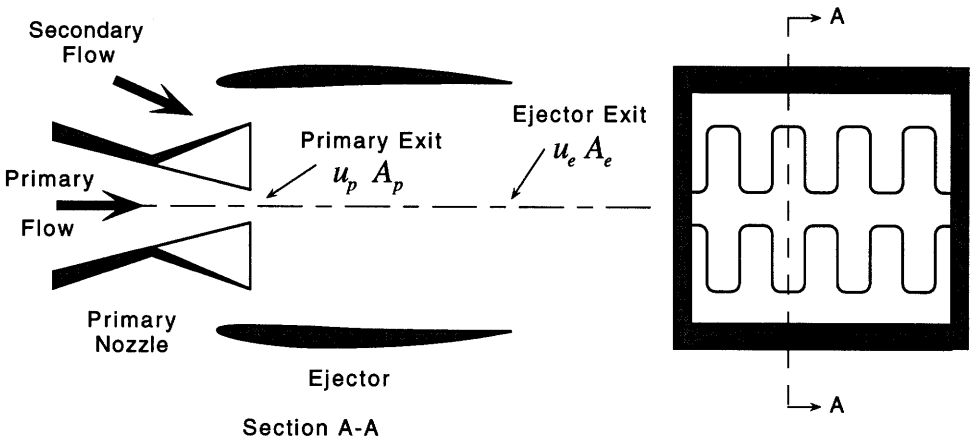

Figure 3-1: Section and rear view of a typical mixer-ejector nozzle for jet noise suppression, adapted from Lord *et al.* [16]

Scale	D^*	D_e	A^*/A_{st} $(D_{st} = 8'')$	A^*/A_{st} $(D_{st} = 12'')$
1	41 in	62.4 in	—	—
1/10	4.1	6.2	0.26	0.12
1/12	3.4	5.2	0.18	0.08
1/16	2.6	3.9	0.10	0.04
1/20	2.1	3.1	0.07	0.03

Table 3.1: Approximate dimensions of full, $1/16^{th}$, and $1/27^{th}$ scale HSCT nozzles

Directivity

Directivity angles from $\psi = 60°$ to $160°$ are of general interest where ψ is measured from the upstream jet axis. For jet noise studies, the downstream arc will be the most critical: $\psi = 90°$ to $160°$.

3.1.2 Noise Generation Mechanisms

Jet noise is generated primarily by two mechanisms: turbulent mixing and the interaction between turbulent structures and the shock cells. The mixing noise will dominate at low frequencies and in the downstream direction. For mixer/ejectors, this noise can be divided into two components.

- *Internal Mixing Noise:* This component is associated with flow over the mixer lobes and tends to dominate at higher frequencies ($f > 500\ Hz$).

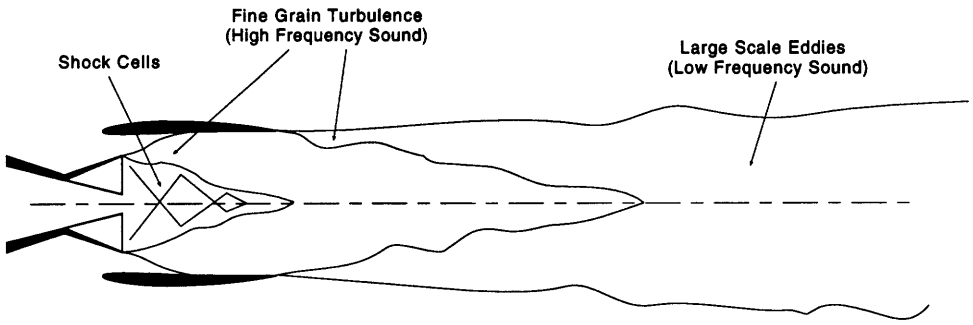

Figure 3-2: Mixer-ejector jet noise generation mechanisms

- *External Mixing Noise:* The external noise is generated by larger scale turbulence resulting from the mixing between the jet and the free stream. It will dominate at lower frequencies, $f = 50\ Hz$ to $500\ Hz$.

In addition, for practical HSCT engine configurations the nozzle may be imperfectly expanded at take-off, resulting in shock associated noise. In general screech tones generated by a feedback mechanism between the shock and the nozzle lip, will not be discernible at the HSCT operating temperatures. However, if broadband shock noise is generated it will dominate the mixing noise in the upstream direction at high frequencies.

3.1.3 Effective Source Distribution

The frequency of mixing noise is a function of turbulence scale and convection speed. As a result, higher frequency sounds are generated by the fine grain turbulence near the nozzle exit, and lower frequencies by the large scale eddies far downstream. However, the source of any given frequency will not be a discrete point, but rather a distribution over a finite volume of the jet. Figure 3-3 shows a typical effective source distribution for a subsonic jet. For HSCT applications, the sources contained within the first 7 to 15 ejector exit diameters are of primary interest.

In the case of mixer/ejector nozzles, there will be high frequency noise associated with the flow over the lobes and through the shock cells. These sources are contained within the mixing duct, and will have an apparent source at the ejector exit.

3.1.4 Effect of Flight Condition

The free stream velocity will have an effect on both the jet noise levels and directivity. As flight velocity increases, any external shock noise is increased while the low frequency mixing

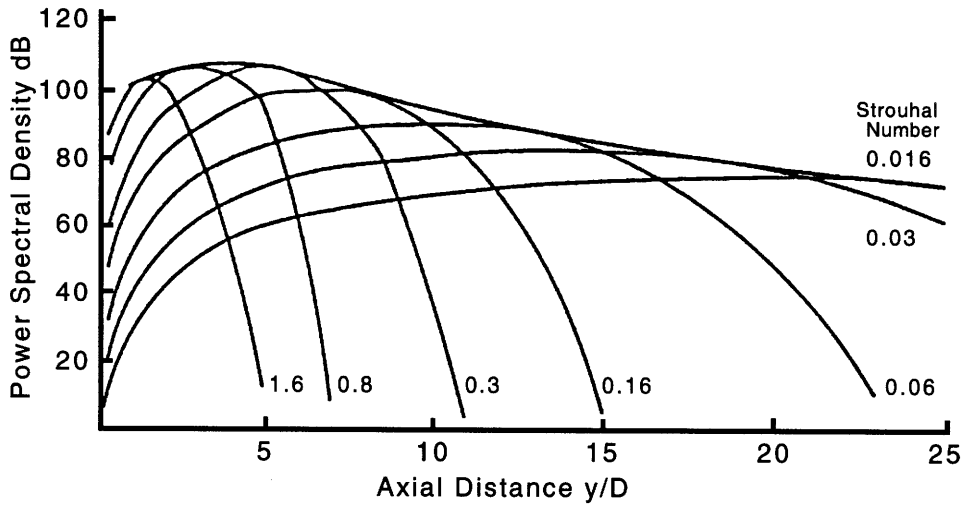

Figure 3-3: Jet noise effective source distribution at low Mach numbers for constant Strouhal number. Source Lilley [15]

noise is decreased. The change in mixing noise is predominantly due to the decrease in jet velocity relative to the free stream. This results in lower shear stresses and correspondingly less turbulent intensity in the mixing region [4].

The internal mixing noise, on the other hand, will be largely unchanged. Therefore, mixer-ejector experiments focusing on this component of the noise will not be significantly effected by the static free stream.

3.1.5 Frequency Scaling

As the scale of the nozzle is decreased, the pressure spectrum level maintains a similar profile but at higher frequencies. A useful non-dimensional quantity for relating the acoustics of different scale nozzles is the Strouhal number:

$$Sr \equiv \frac{fD_e}{u_e} \tag{3.1}$$

For a constant jet velocity, it can be seen that the frequency is inversely proportional to the diameter. Therefore, as is shown in Table 3.2, the frequency range of interest for the $1/20^{th}$ scale nozzle will be 20 times higher than that of the full scale engine. This creates problems for the higher frequencies that can be scaled up into the 100 kHz range.

3.2 Acoustic Measurement Constraints

The nozzle scale will be driven largely by constraints imposed by the acoustic measurements. Far-field distance, frequency scaling, and noise directivity will all play a role in setting the nozzle size and orientation in the test cell.

3.2.1 Far-Field Distance

It is desirable to position the microphones at a distance where the jet behaves as a point source and the acoustic intensity exhibits a $1/r^2$ dependence. Close to the source there are non-propagating modes (pseudosound) which do not follow the spherical spreading law. More importantly, the external mixing noise will have an apparent source distributed along the length of the jet (see Section 3.1.3). As a result, it will appear as a "line" source at small R, falling off with a $1/r$ dependence. However, if the microphones are placed far enough from the jet then it will exhibit the desired $1/r^2$ behavior.

For the HSCT experiments, the relevant sources will be contained within the first $7D_e$ to $15D_e$ of the jet. These external sources will begin to exhibit far-field behavior at a distance of $R_{mic} \approx 40D_e$. For the $8''$ shock tube facility, this constrains D_e to approximately $3.1''$ or $1/20^{th}$ scale. The $12''$ facility, however, would have a larger test cell and could be used to take far-field measurements on nozzles up to $1/12^{th}$ scale nozzle ($D_e = 5.2''$).

If only the high frequency internal noise is considered, the distance to the microphones is less important. The apparent source of this noise will be at the nozzle exit and therefore will exhibit far-field behavior at a shorter distance.

3.2.2 High Frequency Measurements

As was described in Section 3.1.5, the frequencies generated by a fluid jet scale inversely with the diameter of the nozzle. As a result, a small scale model will often move the frequency range of interest up into the 100 kHz range. This introduces numerous problems associated with measuring high frequencies. Corrections must be made for atmospheric attenuation, which are difficult to determine for complex sources. Also, the natural frequency of the microphones must be higher than the measured frequencies. This requires small microphones which exhibit strongly directional characteristics. As a consequence, frequencies cannot be measured in excess of 80 kHz with standard microphones.

	Scale f Measurement Limit (kHz)		
Model Scale	50	80	100
1/10	5.0	8.0	10.0
1/12	4.2	6.7	8.3
1/16	3.1	5.0	6.2
1/20	2.5	4.0	5.0

Table 3.2: Maximum measurable full scale frequencies for various nozzle scales and scaled frequency measurement limits.

This places some limitations on the $1/20^{th}$ scale nozzle. The 80 kHz limit corresponds to a full scale frequency of only 4 kHz, truncating the high frequency range. Therefore, the $1/20^{th}$ scale nozzle will not provide an accurate measure of the internal mixing noise. It will, however, be effective for investigating the lower frequency mixing noise generated downstream of the nozzle.

To characterize the internal mixing, a larger scale nozzle must be used; a $1/16^{th}$ or larger scale nozzle will capture full scale frequencies up to 5 kHz. Using a nozzle this large will result in near-field behavior at low frequencies in the 8″ shock tube facility (see Section 3.2.1). However, if the experiment focuses on only the high frequency internal sources, these effects at low frequencies will not be important. Near-field behavior will not pose a problem for the 12″ facility as far-field measurements can be taken on a $1/12^{th}$ scale nozzle at frequencies as high as 6.7 kHz full scale.

3.2.3 Directivity Angles

In the 8″ shock tube facility, the complete range of directivity angles cannot be covered without changing the height of the nozzle due to the limited size of the test cell (see Figure 3-4). At any given height, the microphones can be positioned over about 60° of the range (see Figure 3-5). For most jet noise experiments, it will be sufficient to cover only the downstream quarter, $\psi \approx 90°$ to 160°. If the nozzle is raised higher in the test cell the downstream angles $\psi \approx 60°$ to $\psi \approx 120°$ can also be covered. Intermediate heights can also be used if there is a more convenient range to investigate between the two. The test cell for the 12″ shock tube facility is large enough to allow a directivity range of $\psi \approx 60°$ to 160° to be covered without moving the nozzle.

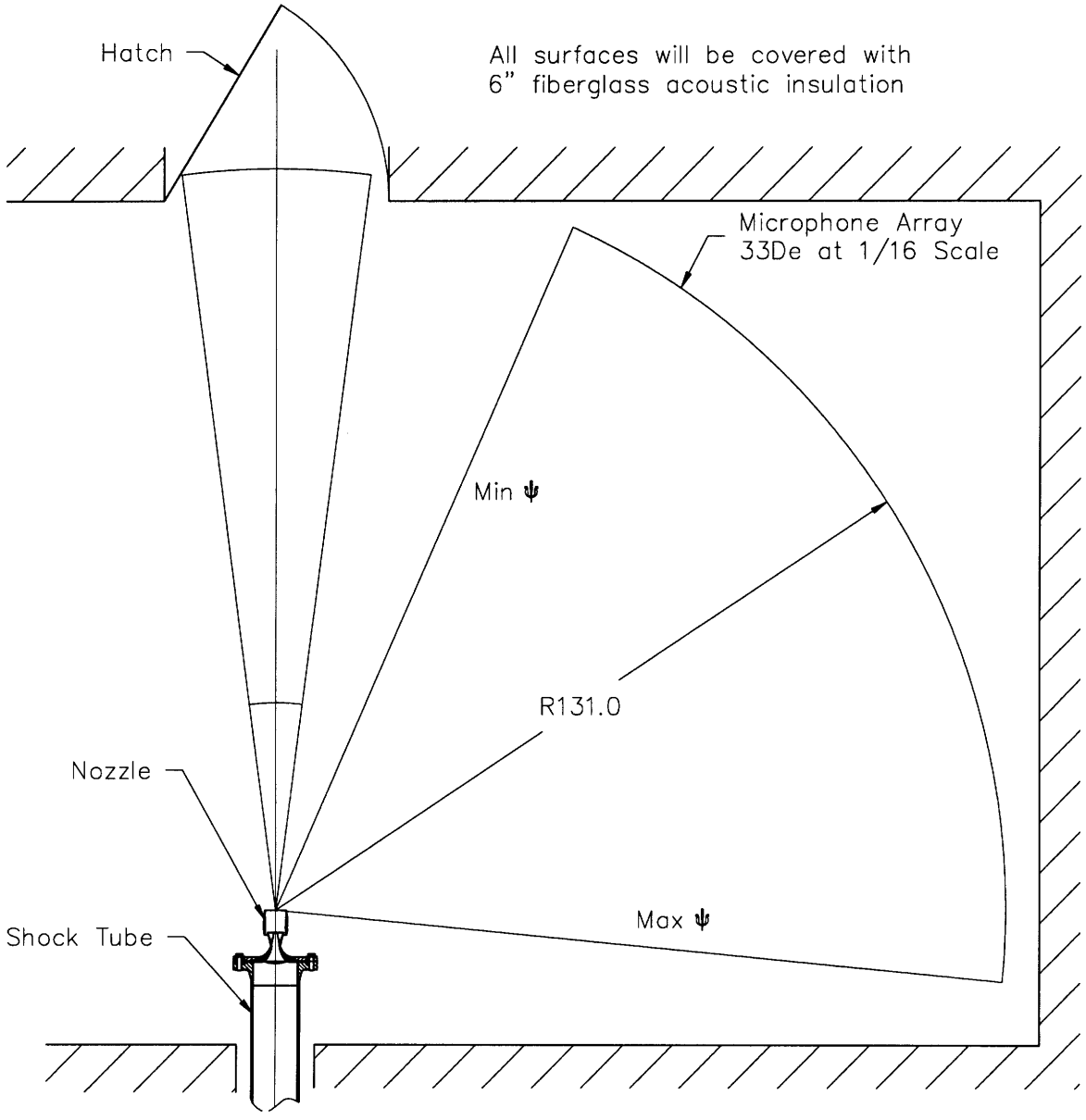

Figure 3-4: Microphone orientation schematic for the 8″ vertical shock tube.

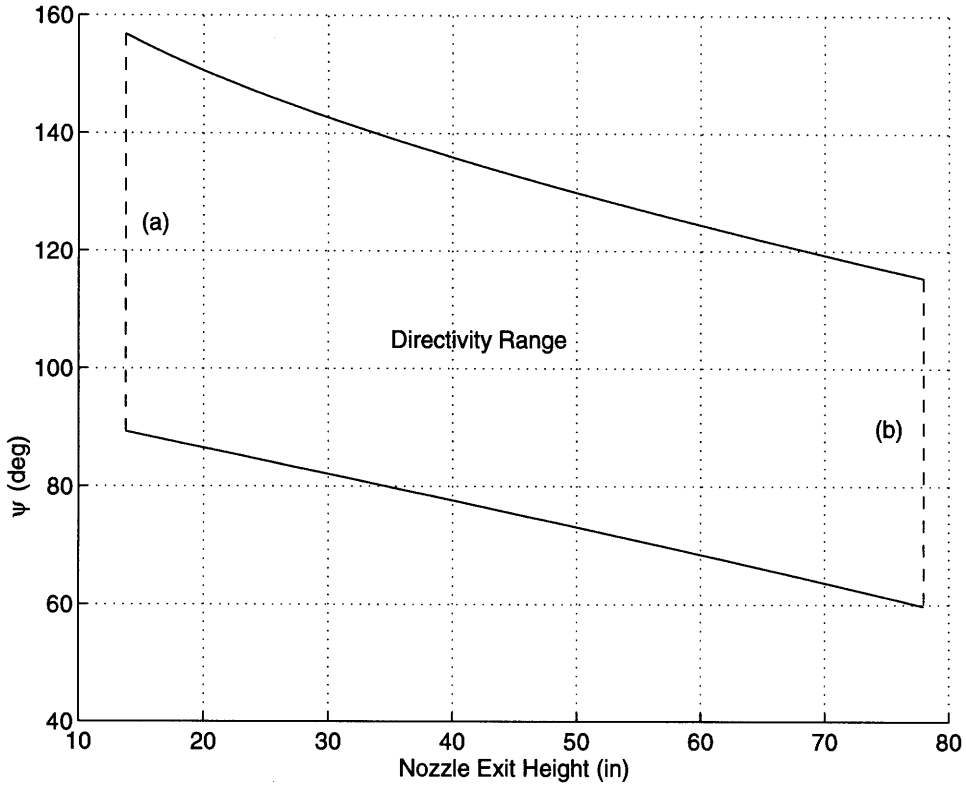

Figure 3-5: Measurable directivity angle range as a function of nozzle height for 8″ shock tube facility. At height (a), $H_n = 13.75''$ and $\psi = 89°$ to 157°. At height (b), $H_n = 78''$ and $\psi = 60°$ to 115°.

3.2.4 Acoustic Sampling Time

The short duration of shock tube experiments makes it critical to understand how much total test time is required to produce results comparable to that of steady state facilities.

The uncertainties in the power spectral analysis were investigated using the methods described by Hardin [8]. It was assumed that the jet noise could be modeled as a chi-square random variable with k degrees of freedom. This random variable, S, can be described by

$$S = Y_1^2 + Y_2^2 + ...Y_k^2 = \sum_{i=1}^{k} Y_i^2 \tag{3.2}$$

where Y_i, $i = 1, 2...k$, are independent, normally distributed random variables with zero means and unit variances. The mean value of S, $E(S)$, is $E(S) = \sum_{i=1}^{k} E(Y_i^2) = k$. Similarly, the probability density function of the chi-square random variable is given by

$$f_s(S;k) = \frac{1}{2^{k/2}\Gamma(\frac{k}{s})} s^{k/2-1} e^{-s/2} \tag{3.3}$$

Using this relation, the variation of the chi-square variable about its mean can be investigated as a function of k, the number of degrees of freedom. Figure 3-6 illustrates this dependence for intervals about the mean containing 80% and 90% of the realizations. For example, 80% of the measured values of $S/E(S)$ can be expected to fall in between the solid lines.

If a single time interval, T, were used to estimate the power spectral density of S, the result could only be expected to fall within 11% and 230% of the actual value 80% of the time. This is clearly insufficient for most experiments. This large variability is predominantly due to the limited number of degrees of freedom of the system; for a single chi-square random variable $k = 2$. The value of k can be increased by subdividing the data into N_B sub-intervals such that

$$\bar{S}_x(w) = \frac{1}{N_B} \sum_{j=1}^{N_B} S_x^{(j)}(w) \tag{3.4}$$

The number of degrees of freedom will then be $k = 2N_B$. For example, dividing the test time into 150 intervals reduces the variability of the power spectrum density to within 11% or ± 1 dB. The price of this increased accuracy is a loss of resolution. The effective

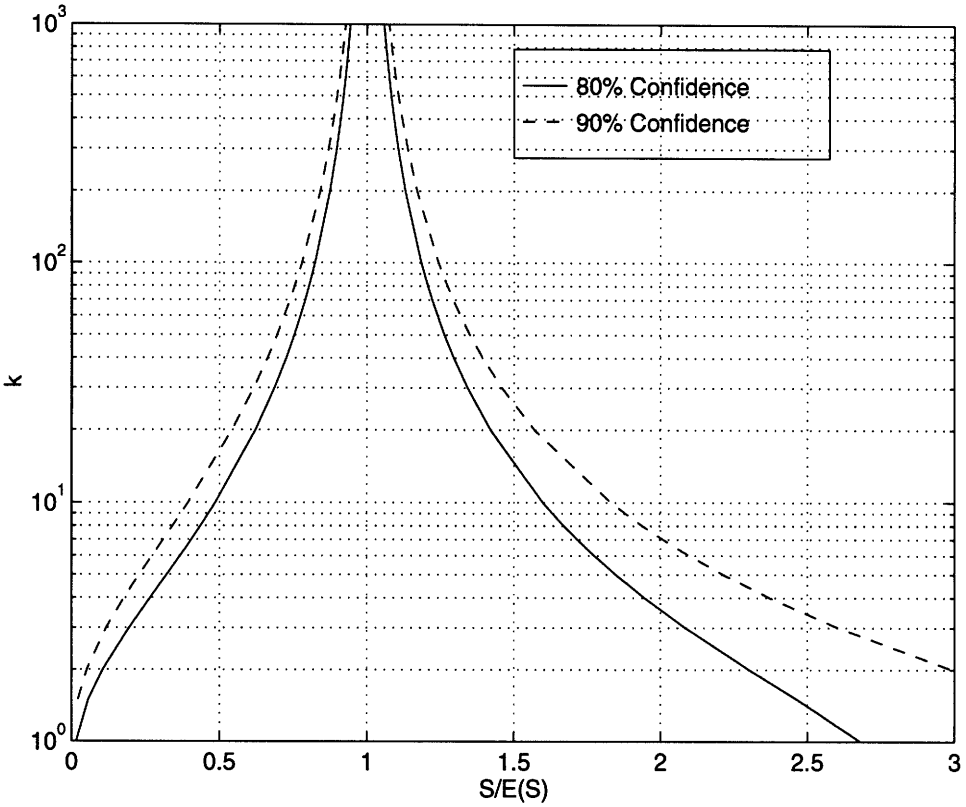

Figure 3-6: Variations of the chi-square variable about its mean, $S/E(S)$, as a function of the number of degrees of freedom, k. The solid line bounds 80% of the realizations, and the dotted line 90%.

80% Confidence					# tests required	
$S/E(S)$	$20log(S/E(S))$	k	Δf (Hz)	T (ms)	10 $ms/test$	20 $ms/test$
0.89 to 1.11	−1.0 to +0.9	300	200	750	76	38
			500	300	30	15
			1000	150	16	8
			2000	75	8	4
			5000	30	3	2
			10000	15	2	1
0.79 to 1.22	−2.0 to +1.7	70	200	175	18	9
			500	70	8	4
			1000	35	4	2
			2000	18	2	1
			5000	7	1	1
90% Confidence					# tests required	
$S/E(S)$	$20log(S/E(S))$	k	Δf (Hz)	T (ms)	10 $ms/test$	20 $ms/test$
0.89 to 1.11	−1.0 to +0.9	500	200	1250	125	63
			500	500	50	25
			1000	250	25	13
			2000	125	13	7
			5000	50	5	3
			10000	25	3	2
0.79 to 1.22	−2.0 to +1.7	120	200	300	30	15
			500	120	12	6
			1000	60	6	3
			2000	30	3	2
			5000	12	2	1
			10000	6	1	1

Table 3.3: Summary of test time requirements for the jet noise experiments. Required test times, T, are presented as functions of the variability $(S/E(S))$, confidence, and bandwidth (Δf).

bandwidth can be written $\Delta f = 1/T_B$ where T_B is the length of each interval: $T_B = T/N_B$. The number of degrees of freedom, the bandwidth, and the total test time can therefore be related by the equation $k = 2\Delta f T$.

The trade-off between variability and resolution is presented in Figure 3.2.4 for the shock tube jet noise experiments. If, for example, it is desired to resolve with 80% confidence the power spectrum levels to within ± 2 dB with a bandwidth of $\Delta f = 1$ kHz, then a $k = 70$ and 35 ms of total test time is required. This would translate to 2 firings of the shock tube at 18 ms of useful data per shot.

For jet noise experiments it is desirable to resolve the corresponding full scale frequencies to 1/3 octave bands since this bandwidth is the basis for the certification standard. Because

each higher octave represents a doubling of frequency, the required bandwidth becomes larger with increased frequency, making the higher frequency bands easier to resolve. The full scale bandwidth can be written

$$\Delta f_{\frac{1}{3}Octave} = \frac{2^{1/3} - 1}{2^{1/6}} f_c \tag{3.5}$$

where f_c is the center frequency of the interval. For instance, if it is desired to resolve corresponding full scale frequencies with f_c starting at 500 Hz into 1/3 Octave bands using a $1/12^{th}$ scale nozzle, a full scale bandwidth of $\Delta f = 116$ Hz would be required that corresponds to a bandwidth of $\Delta f_{1/12} = 1.39$ kHz for the experiments. The higher the frequencies of interest, the larger the bandwidth, and, correspondingly, the fewer required shock tube runs. This implies that for a $1/12^{th}$ scale nozzle at 20 $ms/test$ spectra above 500 Hz full scale can be resolved within ± 2 dB with 3 tests, or ± 1 dB with 9 tests.

This uncertainty analysis is supported by an experimental investigation conducted at NASA Langley Research Center [34]. Data was taken using steady-state jet noise facilities and separated into discrete 8.2 ms blocks. These blocks were compiled into different length ensemble averages ranging in length from 8.2 ms to over 1 sec (1 to 128 blocks). The data was obtained from two different facilities, both of which employed fully expanded $M = 2.0$ nozzles. A total of 128 ensemble averages were taken with frequencies ranging from 400 Hz to 80 kHz.

The first data analyzed was from a $3.6''$ nozzle tested in facility where the test gas was heated with a propane fuel combustion process. Acoustic spectra were analyzed for 1, 2, 3, 4, 8, 16, 32, 64, and 128 ensemble averages, and the standard deviation was calculated for each case. Even after 128 blocks (1 second of data) the standard deviation continued to change with additional averages suggesting that convergence had not been achieved. The second set of data analyzed was from a $2.0''$ nozzle tested in an electric arc heated facility. In this case, the standard deviation converged smoothly, arriving within 0.6 dB of the final value after the first average and to within 0.1 dB after 8 to 16 averages.

The difference between these two facilities is attributed to two factors: (1) the different nozzle scales and (2) the core noise of the combustion facility. The shock tube, with its highly uniform reservoir conditions, can be expected to perform at least as well as the electric arc facility. This implies that, for a $2''$ nozzle, measurements within 1 dB may be

obtained with a single test, and convergence within 0.1 dB achieved within 4 to 8 tests. In addition, a much larger bandwidth, $\Delta f \approx 1\ kHz$, may be adequate, further reducing the variability.

The signal from the microphones will be read by a digital IO board, which means that the the sampling rate will be significant. The Nyquist frequency, $f_N = 1/2\Delta t$, is the highest frequency that can be reproduced from data sampled at equal intervals Δt. This means that to resolve frequencies up to 80 kHz, a sampling rate of at least 160 kHz per channel is required. Some increase over this minimum rate is desired. A sampling rate of $2.5 f_{max}$ has been found to give good results in most applications [26].

3.3 Jet Start-up time

The duration of constant reservoir conditions presented in Chapter 2 is not the actual amount of useful test time. A fraction of this time will be required for the turbulent jet to reach a quasi-steady state. For downstream mixing studies, the jet start-up time can be significant, $t_{start} \approx 2$ to 5 ms for HSCT studies. It is necessary, therefore, to model this starting process in order to better estimate the time available for taking measurements.

3.3.1 Jet Development Model

The jet was assumed to develop at $\frac{1}{2}u_c$, where u_c is the centerline velocity. The jet was divided into two regions for the calculation: a region where the potential core exists and the centerline velocity remains constant at $u_c = u_e$, and a fully-developed region where u_c exhibits a $1/x$ decay (see Appendix C). Using the turbulent jet model described in references [32] and [30], the time for the jet to develop to a length l_{jet} can be described in terms of the exit diameter, jet velocity, and potential core length:

$$\frac{t_{start} u_e}{D_e} = 2\left(\frac{l_{jet}}{D_e}\right) \qquad \frac{l_{jet}}{D_e} \leq \frac{l_{pc}}{D_e} \tag{3.6}$$

$$\frac{t_{start} u_e}{D_e} = \left(\frac{l_{pc}}{D_e}\right)\left[\left(\frac{l_{jet}}{D_e}\frac{D_e}{l_{pc}}\right)^2 + 1\right] \qquad \frac{l_{jet}}{D_e} \geq \frac{l_{pc}}{D_e} \tag{3.7}$$

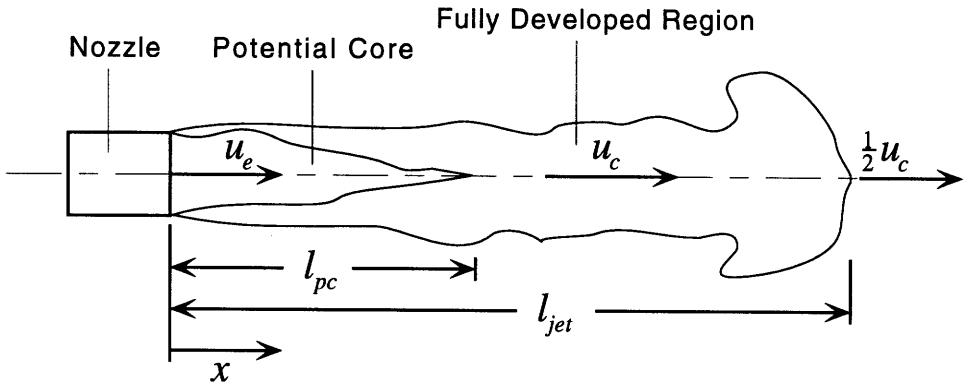

Figure 3-7: Schematic of jet starting parameters.

where $l_{pc}/D_e \approx 6.57$. For mixer/ejector studies, a jet length of $7D_e$ to $15D_e$ is sufficient to capture the relevant noise sources. Jet starting times will range from $t_{jet} = 2.6\ ms$ for the $1/20^{th}$ scale nozzle to $t_{jet} = 5.2\ ms$ for the $1/10^{th}$ scale. Tables 3.5 and 3.5 summarize the jet starting times and net test times for various nozzle configurations and operating conditions.

3.3.2 Nozzle Starting Model

For mixer/ejector nozzles, the time for the nozzle to fully "start" can be a significant fraction of the total test time. In general, a nozzle can be considered started after about 3 flow-through times. For a conservative estimate, the average velocity in the primary nozzle was assumed to be $\bar{u}_p \approx \frac{1}{2}(u^* + u_p)$ and the secondary flow velocity through the ejector simply u_s. Using the geometry in figure 3-1 the flow-through and residence times were estimated for the different scale nozzles:

	Nozzle Length		Flow-Through Times		
	$l_p\ (in)$	$l_e\ (in)$	$t_p\ (\mu s)$	$t_e\ (\mu s)$	$t_{start}\ (ms)$
1/10	6	18.6	244	3257	7.1
1/12	6	15.6	244	2802	6.1
1/16	6	11.7	244	1351	4.8
1/20	6	9.3	244	1074	4.0

Table 3.4: Approximate nozzle flow-through and start-up times. The nozzle was assumed to be started at $t_{start} = 3(t_p + t_e)$ where t_p is the residence time for fluid in the primary nozzle and t_e for the ejector.

These values can be added to those from the jet starting model to give a conservative

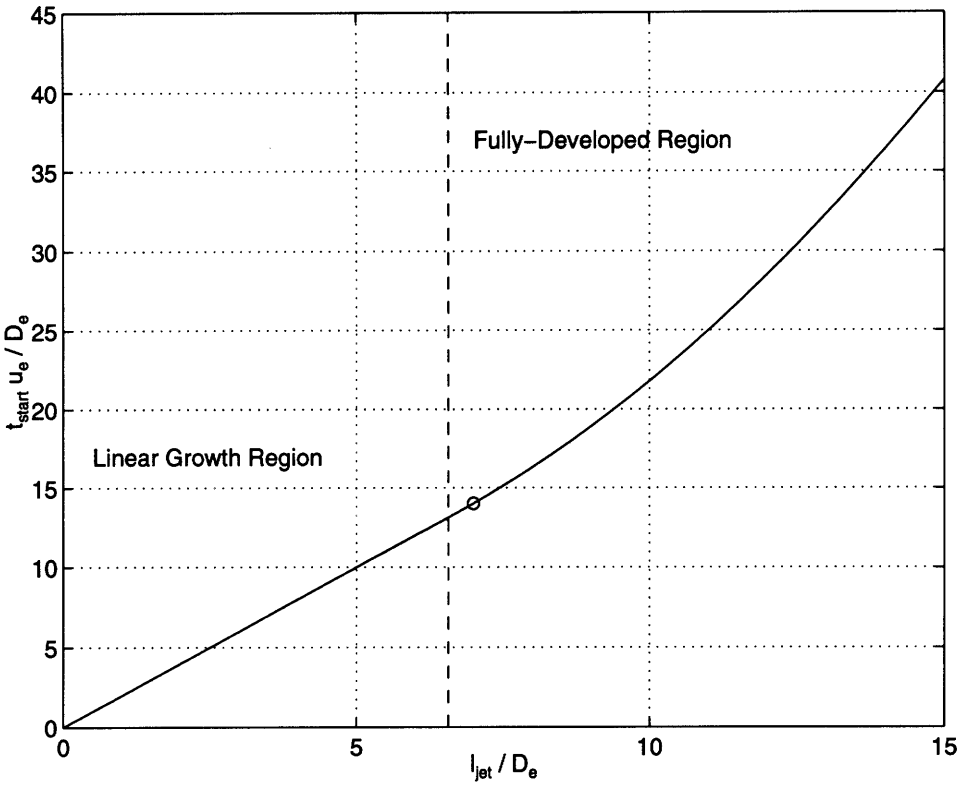

Figure 3-8: Non-dimensional jet starting time as a function of l_{jet}/D_e. Circle refers to required length for HSCT experiments, $l_{jet}/D_e \approx 7$.

estimate of the total start-up time. The results are shown in Table 3.4.

3.4 Room Acoustics

3.4.1 Anechoic Treatment of Room

Sound will have sufficient time to reflect from the walls of the test cell and impinge back on the jet or on the microphones. As a result, it will be necessary to cover the walls, floor, and ceiling with acoustic insulation. The intensity of the reflections should be at least 10 dB less than the incident noise to insure that the effect on the test will be negligible. To accomplish this, $6''$ thick fiberglass insulation with a density of $\rho \approx 2\ lbs/ft^3$ can be used. This should be sufficient for frequencies over 100 Hz. [11].

3.4.2 Start-up noise

There will be a high amplitude acoustic impulse preceding the actual test due to the unsteady mass addition associated with the starting of the nozzle. This noise will be of a

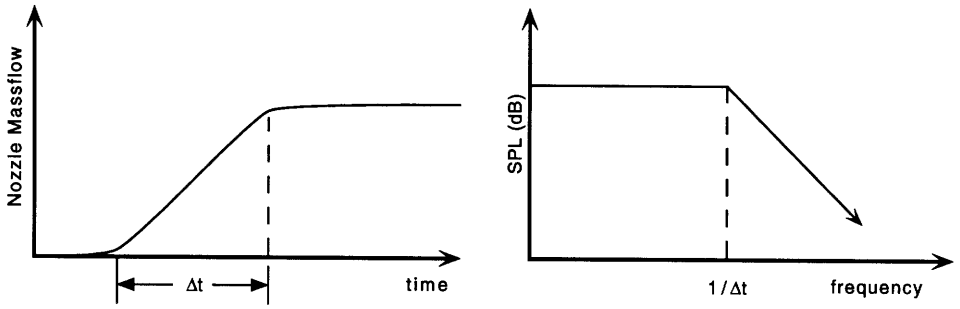

Figure 3-9: "Start-up" noise associated with starting of the nozzle. (a) massflow through nozzle as a function of time. (b) Frequency content of the start-up noise.

higher amplitude than the quasi-steady state jet noise. As a result, reverberations of this noise from the acoustically treated walls may be strong enough to affect the steady state measurements. The pulse will contain a distribution of frequencies up to around $f \approx 1/\Delta t$, where Δt is the time for the massflow to reach a steady state as shown in Figure 3-9.

At the start of the test, the shock wave will rupture the secondary diaphragm and propagate through the nozzle followed by the test gas. The nozzle start-up time, Δt, can be approximated as the time between the arrival of this shock and the test gas at the nozzle exit. For HSCT experiments $\Delta t \approx 80\ \mu s$, which places the break frequency around 12 kHz. As a result, there is some overlap between this signal and the measured frequency range. However, the primary frequencies of interest, 1 to 4 kHz full scale, will be above this range for nozzles smaller than $1/12^{th}$ scale. It is difficult to predict if this noise will be sufficiently damped by the acoustic insulation. Should this prove to be a problem additional insulation can be added.

3.5 Summary of Facility Performance for Various Nozzle Configurations

Tables 3.5 and 3.5 summarize the performance for the 8″ and 12″ shock tube facilities. A wide range of nozzle geometries and operating conditions can be tested with both designs, however the 12″ facility would be more effective for testing mixer/ejector nozzles. The capabilities of each facility are described below.

	Jet Parameters			Nozzle Geometry			Acoustics		Test Times (ms)				
Mixer/Ejectors	p_5/p_0	T_5/T_0	u_e (m/s)	D^* (in)	D_e (in)	A^*/A_{st}	f_{max}	R_{mic}/D_e	t_{exp}	t_{exg}	t_{nozzle}	t_{jet}	t_{net}
1/10 Scale	3.4	2.75	530	4.1	6.2	0.26	8.0	21	16.0	8.9	7.2	4.2	0†
1/12 Scale				3.4	5.2	0.18	6.7	25		13.0	6.1	3.5	3.5†
1/16 Scale				2.6	3.9	0.10	5.0	33		22.2	4.8	2.6	8.6
1/20 Scale				2.1	3.1	0.07	4.0	42		34.1	4.0	2.1	9.9
Unshrouded Nozzles	p_5/p_0	T_5/T_0	u_p (m/s)	D^* (in)	D_p (in)	A^*/A_{st}	α_{max}	R_{mic}/D_p	t_{exp}	t_{exg}	t_{nozzle}	t_{jet}	t_{net}
$M = 1.5$ Nozzle	3.7	2.0	608	3.0	3.3	0.14	11.0	40	18.8	31.1	0.9	1.9	16.0
		2.7	718	2.5	2.7	0.10	7.6	48	16.0	23.5	0.7	1.3	14.0
		4.0	863	2.1	2.3	0.07	5.4	57	13.4	19.8	0.6	0.9	11.9
		5.9	1049	1.8	2.0	0.05	3.9	65	9.1	17.7	0.5	0.7	7.9
$M = 2.5$ Nozzle	17.1	2.0	813	2.0	3.3	0.06	8.2	40	18.8	72.5	0.7	1.4	16.7
		2.7	961	2.0	3.3	0.06	7.0	40	16.0	39.2	0.6	1.2	14.2
		4.0	1155	2.0	3.3	0.06	5.8	40	13.4	23.1	0.5	1.0	11.9
		5.9	1403	1.8	2.9	0.05	4.2	45	9.1	17.7	0.4	0.7	8.0

Table 3.5: Summary of test times and acoustic measurement ranges for the 8″ vertical shock tube facility. † The test gas exhaustion times are upper limits (see Chapter 2) and do no account for various test gas contamination mechanisms. Actual test times in these cases may be substantially less.

	Jet Parameters			Nozzle Geometry			Acoustics		Test Times (ms)				
Mixer/Ejectors	p_5/p_0	T_5/T_0	u_e (m/s)	D^* (in)	D_e (in)	A^*/A_{st}	f_{max}	R_{mic}/D_e	t_{exp}	t_{exg}	t_{nozzle}	t_{jet}	t_{net}
1/10 Scale	3.4	2.75	530	4.1	6.2	0.12	8.0	29 (33)	25.7	31.1	7.2	4.2	14.3
1/12 Scale				3.4	5.2	0.08	6.7	35 (40)		45.2	6.1	3.5	16.1
1/16 Scale				2.6	3.9	0.04	5.0	46 (53)		77.2	4.8	2.6	18.3
1/20 Scale				2.1	3.1	0.03	4.0	58 (67)		118.4	4.0	2.1	19.6
Unshrouded Nozzles	p_5/p_0	T_5/T_0	u_p (m/s)	D^* (in)	D_p (in)	A^*/A_{st}	α_{max}	R_{mic}/D_p	t_{exp}	t_{exg}	t_{nozzle}	t_{jet}	t_{net}
$M = 1.5$ Nozzle	3.7	2.0	608	4.1	4.5	0.12	15.0	40	30.3	56.0	0.9	2.6	26.8
		2.7	714	3.8	4.1	0.10	11.6	44	25.7	36.3	0.7	2.0	23.0
		4.0	863	3.1	3.4	0.07	8.0	53	21.6	30.5	0.6	1.4	19.6
		5.9	1049	2.9	3.1	0.06	6.0	59	14.0		0.5	1.1	12.4
$M = 2.5$ Nozzle	17.1	2.0	813	2.8	4.5	0.05	11.2	40	30.3	134.3	0.7	2.0	27.6
		2.7	955	2.8	4.5	0.05	9.5	40	25.7	72.5	0.6	1.7	23.4
		4.0	1155	2.8	4.5	0.05	7.9	40	21.6	42.7	0.5	1.4	19.7
		5.9	1403	2.8	4.5	0.05	6.5	40	14.0	27.3	0.4	1.1	12.5

Table 3.6: Summary of test times and acoustic measurement ranges for the 12″ horizontal shock tube facility.

3.5.1 8″ Vertical Shock Tube Facility

This facility will be capable of supporting a range of nozzles that sufficiently bracket the design space for the HSCT. Nozzle pressure ratios up to 30 and primary stream total temperatures up to 1750 K can be achieved. There are, however, a number of limitations on the nozzle sizes and acoustic measurements due to the limited space available to house the facility:

- The total shock tube length is limited to the 38′ between the test cell and the sub-basement floor. This allows approximately 16 ms of total test time, and, after jet starting is considered, about 9 ms to take data.
- The limited size of the test cell allows for only a 60° range of directivity angles that can be covered in any given test. The complete range from $60° < \psi < 120°$ can be covered by changing the height of the shock tube and nozzle in the test cell.
- The limited distance to the microphones constrains the nozzle size to $1/20^{th}$ scale if the far-field $R_{mic} = 40D_e$ is to be satisfied. Larger nozzles will require near-field corrections or the measurements of the distributed noise sources along the jet will be difficult to interpret.

As a result, no single nozzle can be used to acquire a complete set of data for full scale frequencies from 100 Hz to 5 kHz (the critical range for mixer/ejector studies) and directivity angles from 60° to 120°. Any nozzle will only give a subset of this range. The combination of a $1/16^{th}$ and a $1/20^{th}$ scale nozzles, however, could be used to cover the entire range.

$1/16^{th} Scale Mixer/Ejector Nozzle$

- *Test time:* 8.6 ms. Approximately 12 tests would be required to resolve full scale frequencies within ± 1 dB [2].
- *Frequency measurement limit:* 80 kHz corresponds to 5 kHz full scale.
- *Primary constraint:* Maximum throat area set by test gas exhaustion time.
- *Strength:* Large scale allows higher frequencies to be investigated.

[2] For 90% confidence that tests will lie within ± 1 dB of mean. Full scale bandwidth $\Delta f = 116$ Hz (1/3 Octave bands over 500 Hz)

- *Weakness:* Microphones can only be placed $20D_e$ from the source; distributed source corrections are required.

$1/20^{th} Scale Mixer/Ejector Nozzle$

- *Test time:* 9.9 ms. Approximately 10 tests would be required to resolve full scale frequencies within ± 1 dB [3]
- *Frequency measurement limit:* 80 kHz corresponds to 4 kHz full scale.
- *Primary constraint:* Nozzle size set by requirement that microphones be located at $40D_e$ from the nozzle exit.
- *Strength:* No distributed source corrections are required.
- *Weakness:* High frequency range ($f > 4$ kHz) is cut off.

Unshrouded Nozzles

In many cases it will be useful to test unshrouded nozzles. In order to validate the facility, simple axisymmetric nozzles can be tested and the results compared with data from continuous facilities. Similarly, the fluid dynamics and acoustics of lobed mixers can be investigated in the absence of a mixing duct.

Examples of various unshrouded nozzles are presented in Table 3.5. The exit diameters were set such that the microphones would be in the far-field and the test duration would not be limited by the exhaustion of the test gas. In general, there will be ample test time for most of the configurations. Both the jet and unshrouded nozzle starting times are significantly less than for the mixer/ejector nozzles. Test time does, however, become shorter at higher total temperatures.

3.5.2 12″ Horizontal Shock Tube Facility

The alternate location of the facility alleviates many of the space constraints allowing the shock tube to be designed to support larger nozzles. The total length of the shock tube can be extended to 60′, which almost doubles the test time. Similarly, the larger test cell

[3] For 90% confidence that tests will lie within ± 1 dB of mean. Full scale bandwidth $\Delta f = 116$ Hz (1/3 Octave bands over 500 Hz)

allows for up to a $1/12^{th}$ scale HSCT nozzle to be employed. Measurements can be taken up to 6.7 kHz full scale at directivity angles of 60° to 120° without moving the shock tube or nozzle. A $1/12^{th}$ scale nozzle scenario is summarized below:

$1/12^{th} Scale Mixer/Ejector Nozzle$

- *Test time:* 16.1 ms. Approximately 12 tests would be required to resolve full scale frequencies within ± 1 dB[4].
- *Frequency measurement limit:* 80 kHz corresponds to 6.7 kHz full scale.
- *Strength:* Microphones can be placed in far-field. Directivity angles of $60° < \psi < 120°$ can be measured in a single test.

3.5.3 Facility Performance Trends

Due to the large number of parameters that can be varied, it is difficult to summarize how the facility will perform for all possible reservoir conditions and nozzle configurations. There are, however, a number of constraints and trends which may illuminate how the facility will perform for nozzles not specifically cited.

- *Reservoir Pressures:* $(p_5/p_0)_{max} \approx 38$ assuming an 8% attenuation of the shock. This corresponds to a perfectly expanded $M = 3.0$ nozzle. To a first order, varying p_5/p_0 does not affect the time-distance history in the shock tube. This is because the strengths of the shocks and expansions are only dependent on pressure ratios and not the absolute pressure in the tube.
- *Reservoir Temperature:* Using an all helium driver and air as a test gas, reservoir temperatures up to 1750 K can be achieved. However, as T_5/T_1 is increased the test time is reduced. Stronger shocks are required to heat the fluid, so reflected waves will arrive at the nozzle more rapidly. Similarly, the time to exhaust the test gas is also reduced; in order to keep the same p_5/p_0 the initial pressure in the driven section must be lower. This results in a lower total mass of test gas.

[4]For 90% confidence that tests will lie within ± 1 dB of mean. Full scale bandwidth $\Delta f = 116$ Hz (1/3 Octave bands over 500 Hz)

- *Nozzle Throat Area:* The time to exhaust all of the test gas is inversely proportional to A^*/A_{st}, therefore the primary effect of increasing the nozzle throat area is to decrease t_{exg}. Less significantly, the strength of the reflected shock is affected by the massflow through the throat area. As the nozzle throat increases, there will be increasing losses in the stagnation pressures and temperatures in the reservoir compared to the ideal case.

- *Nozzle Exit Diameter:* There are a number of constraints that can be related to the nozzle exit diameter, D_e (or D_p in the case of unshrouded nozzles). The distance to the microphones is considered in terms of exit diameters, so the larger the nozzle the further away the microphones must be to take far-field measurements. This is less significant for high frequency noise generated near or inside the nozzle. For the lower frequencies distributed along the jet, $R_{mics} \approx 40D_e$ is required for far field behavior. Due to the limited size of the laboratory, this constrains the nozzles to be less than $3.3''$ diameter for the $8''$ facility or $5.2''$ diameter for the $12''$ facility.

- *Nozzle Scale:* The frequency of the jet noise scales inversely with the diameter of the nozzle. Because frequencies over 80 kHz cannot be easily measured, the minimum nozzle size is set based on the desired full scale frequency range.

Chapter 4

Mechanical Design

One of the many strengths of the shock tube as a research tool is its mechanical simplicity. It requires no moving parts other than those associated with replacing the diaphragms, and the bulk of the tube can be constructed from standard stainless steel flanges and pipe. There are, however, many mechanical details associated with the pipe sections, diaphragms, and instrumentation that require special attention.

This chapter will highlight the mechanical design of the proposed 8″ vertical shock tube and give some recommendations on how this design could be scaled and adapted for 12″ shock tube in the the alternate laboratory space. The shock tube can be divided into three primary sub-assemblies: the tube sections, the primary diaphragm assembly, and the secondary diaphragm/nozzle assembly. These are each described in detail and complete set of mechanical drawings is included in appendix D.

4.1 The Driver and Driven Sections

The driver and driven sections are both of similar construction, each consisting of flanged lengths of stainless steel tubing fitted with instrumentation blocks, fill ports, and lifting lugs as shown in Figures 4-1 and 4-2. The shock tube will pass through a number of public areas, so for safety the design was made to conform to the ASME boiler and pressure vessel codes [20]. Cost was an important factor, so every effort has been made to minimize the number of parts and machining operations.

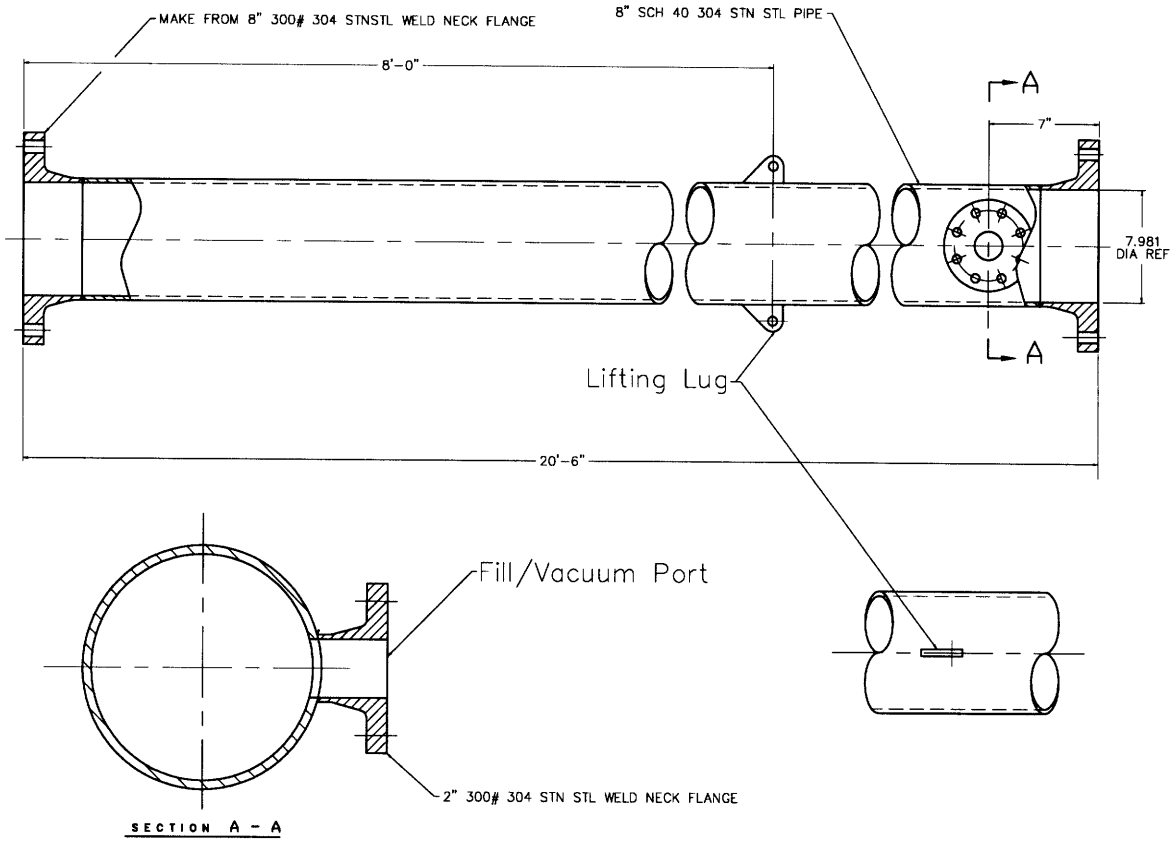

Figure 4-1: Driver Section Schematics

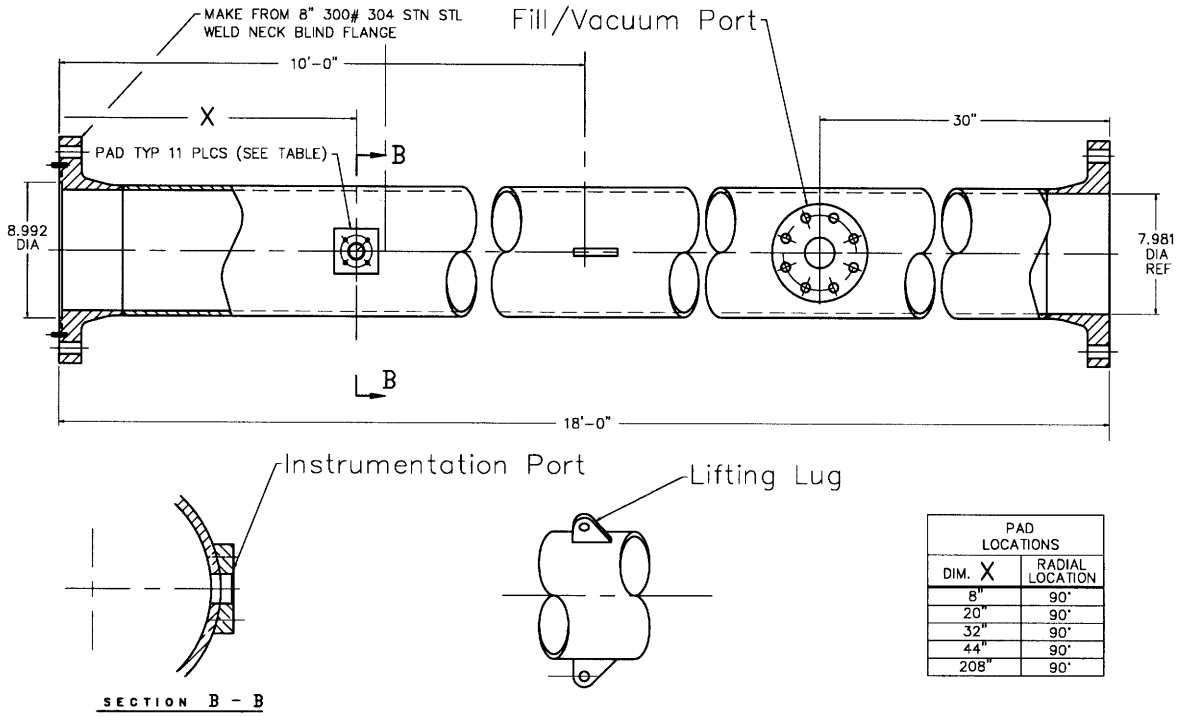

PAD LOCATIONS	
DIM. X	RADIAL LOCATION
8"	90°
20"	90°
32"	90°
44"	90°
208"	90°

Figure 4-2: Driven Section Schematics

Stainless Steel Tubing

The driver and driven sections will be constructed from lengths of schedule 40 seamless stainless steel pipe connected by 300# weld-neck flanges. This configuration gives the required pressure-temperature rating as well as sufficient wall thickness to allow honing of the driven section. Both the driver and driven sections will be constructed out of single lengths of flanged pipe. This will provide a lower cost solution than constructing the tube from shorter flanged sections because it minimizes the number of machining and welding operations. It also eliminates any "steps" between adjacent tube sections that could perturb the flow. It does, on the other hand, result in a loss of versatility. The relative lengths of the two sections cannot be adjusted, so the tube will only be optimized for the HSCT operating point (see Section 2.3.1). However, the section lengths are already tightly constrained in order to keep the primary diaphragm in an accessible location.

In the alternate laboratory space, the shock tube could be oriented horizontally and both its length and diameter increased ($l_{st} \approx 60'$, $D_{st} \approx 12''$). This results in significantly longer test times (see Section 3.5) and also eases the constraints on the diaphragm location. The driver and driven section lengths, therefore, do not need to be fixed lengths but could instead be constructed from shorter interchangeable sections. Commercial pipe is only available in 20' lengths, so a reasonable solution would be to have two $20'$, one $14'$, and one $6'$ section. For operation at relatively low reservoir temperatures and in the tailored interface mode, as will be required for the HSCT experiments, the driver would consist of a $20'$ and the $14'$ section, and the driven a $20'$ and the $6'$ section (see Section 2.3.1). For non-tailored operation or very high reservoir temperatures, the lengths could be changed to $l_{dr} = 14'$ and $l_{dn} = 46'$, providing better performance at these points that would be possible with a tube optimized for the HSCT design range. There will be steps introduced at the intersection of each of these sections, which could effect the fluid-dynamic performance. However, the last $20'$ of the driven section, where the boundary layer is critical, will be constructed from a single length of pipe. As a result, this design would provide both good performance and a large increase in versatility.

Internal Surface Finish

The inside of the driven section will be honed in order to remove any small scale imperfections (scratches, digs, turning marks, etc.) that could perturb the flow. Internal surface finishes vary widely between shock tubes, from a few microinches RMS to the standard hot-rolled finishes of commercial pipe [7]. For this application, a 63 microinch RMS finish will be sufficient for the turbulent wall boundary layer [27]. The boundary layer in the driver section has little impact on shock tube performance, so only the driven section will need to be honed.

Gas Fill/Vacuum Ports

There will be a $2''$ port installed in both the driver and driven section that can be used to both evacuate and pressurize each section. The ports will be constructed from standard $2''$, 300# weld neck flanges welded to the outside wall of the tube. A three way ball-valve can be installed on this port to allow connection to either a $2''$ line running to a vacuum pump or a $1/4''$ line running to the gas bottles. The three way valve will provide a valuable safety, preventing the tube from being pressurized while still connected to the vacuum system. The ports are located close to the primary diaphragm assembly, where they will have little effect on the reservoir conditions or nozzle flow.

Instrumentation Ports

There are five instrumentation ports located along the length of the driven section. Four of these ports are arranged at $12''$ intervals near the tube end-wall and will be used to establish the shock speed immediately before and after shock reflection. The fifth tap is located just downstream of the primary diaphragm assembly and can be used as a trigger to initiate the data acquisition.

At each location, a piezo-electric pressure transducer can be mounted on the $5/8''$ plug. These sensors will detect the sharp pressure increase across shock and can be used to clock its passage time between adjacent taps. The four taps near the end-plate will give the average shock velocity over three adjacent intervals. This allows a quadratic fit to be made that will accurately characterize the shock speed in the neighborhood of the nozzle.

Each instrumentation port consists of a transducer mounted on a stainless-steel plug

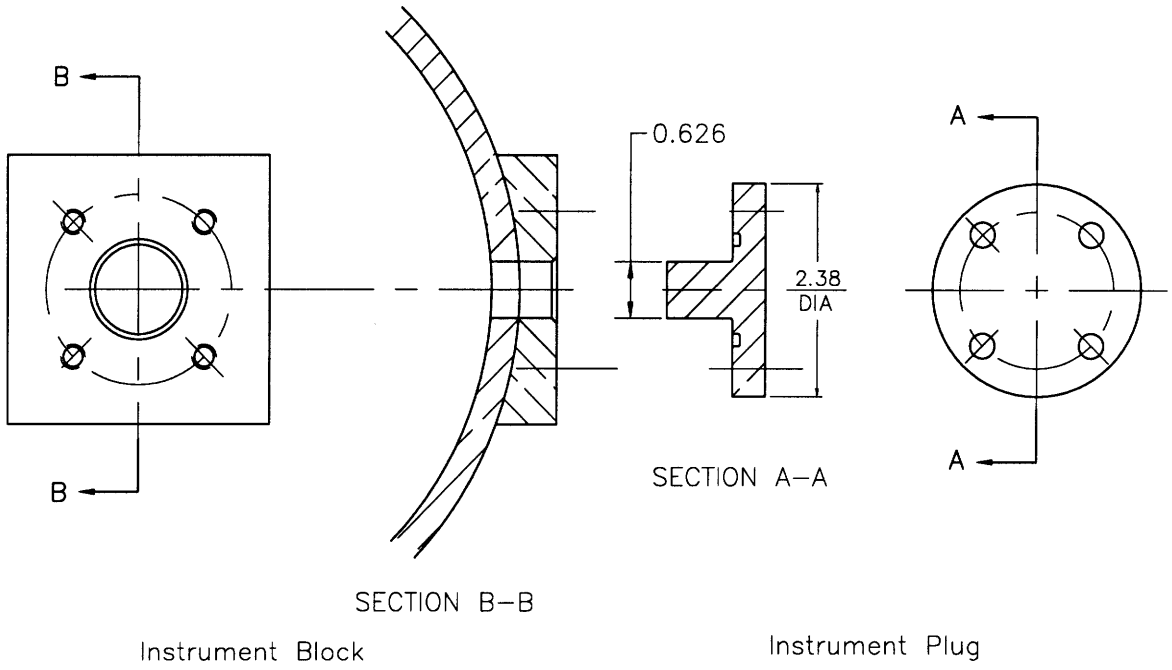

Figure 4-3: Instrumentation port schematic.

(Drawing GTL-103) and a mounting block welded to the tube wall (Drawing GTL-102). The plugs will be interchangeable so that instruments can be swapped or replaced by blind plugs. To save on machining costs, the end of the plugs will be machined flat instead of following the inside contour of the tube. Even with this simplification, at the worst point the plug will only be recessed about 0.018 ± 0.05 from the internal surface. This will not cause a significant perturbation in the flow. However, a flush fit can be achieved if the plugs are left in place during the honing operation. Studs should be installed in the mounting block to avoid damaging the threads through continuous application of the bolts.

4.2 The Primary Diaphragm Assembly

The primary diaphragm assembly consists of three housings clamped between the driver and driven sections by a ring of 7/8″ bolts as shown in Figure 4-4. Diaphragms can be placed both above and below the mid-section housing, enabling either a single or double diaphragm bursting technique to be used. The diaphragms can be accessed by unthreading the 7/8″ bolts from the tapped holes in the lower flange and lifting the counterweighted driven section and upper housing out of the way.

Downstream of each diaphragm will be a cruciform blade cutting device that is used

to both control the burst pressure and to ensure proper petaling. The diaphragms will typically be made of aluminum foil ranging in thickness from $0.006''$ to $0.020''$.

4.2.1 Single Diaphragm Method

The simplest diaphragm bursting technique uses the driver pressure to press the diaphragm against a set of knife blades. The blades are initially set at a predetermined distance, b, behind the diaphragm. The tube is then evacuated and the driven section filled to the desired initial pressure, p_1. The driver gas is then introduced at a constant fill rate, gradually increasing the driver pressure toward p_4. As the pressure across the diaphragm increases, the diaphragm will bulge toward the knife blades, rupturing when it makes contact with the pin at the center. The burst pressure can be controlled either by changing the diaphragm thickness, t_d, or by adjusting the initial separation between the diaphragm and the knife blades. Calibration curves will need to be developed in order to predict the burst pressure based on t_d and b. Provided the driver fill rate is consistent for each run, this technique has proven effective on similar shock tubes [3]

4.2.2 Double Diaphragm Method

If the driver pressure or the test starting time must be controlled more accurately than can be done with a single diaphragm, a double diaphragm technique can be used. A diaphragm is placed on each side of the mid-section housing, creating a short intermediate section separating the expansion and compression chambers. This section is maintained at a pressure around $\frac{1}{2}\Delta p$, where $\Delta p \equiv p_4 - p_1$ is the pressure difference across the diaphragm assembly. A $1/4''$ line is run from this intermediate pressure section through a solenoid switch and into an evacuated vessel. To rupture the diaphragm the solenoid switch is opened, evacuating the mid-section and doubling the pressure difference across the lower diaphragm. If the burst pressure of the diaphragms is set anywhere between $\frac{1}{2}\Delta p$ and Δp, both diaphragms will rupture in quick succession. Less calibration is required than when using the single diaphragm technique because p_4 is no longer entirely dependent on the diaphragm burst pressure. However, the turn-around time for the experiments may be somewhat slower due to the extra steps involved in balancing the tube pressures. This method has been used in a wide variety of shock tubes with driver pressures running from 50 psi to well over 100 atm [3].

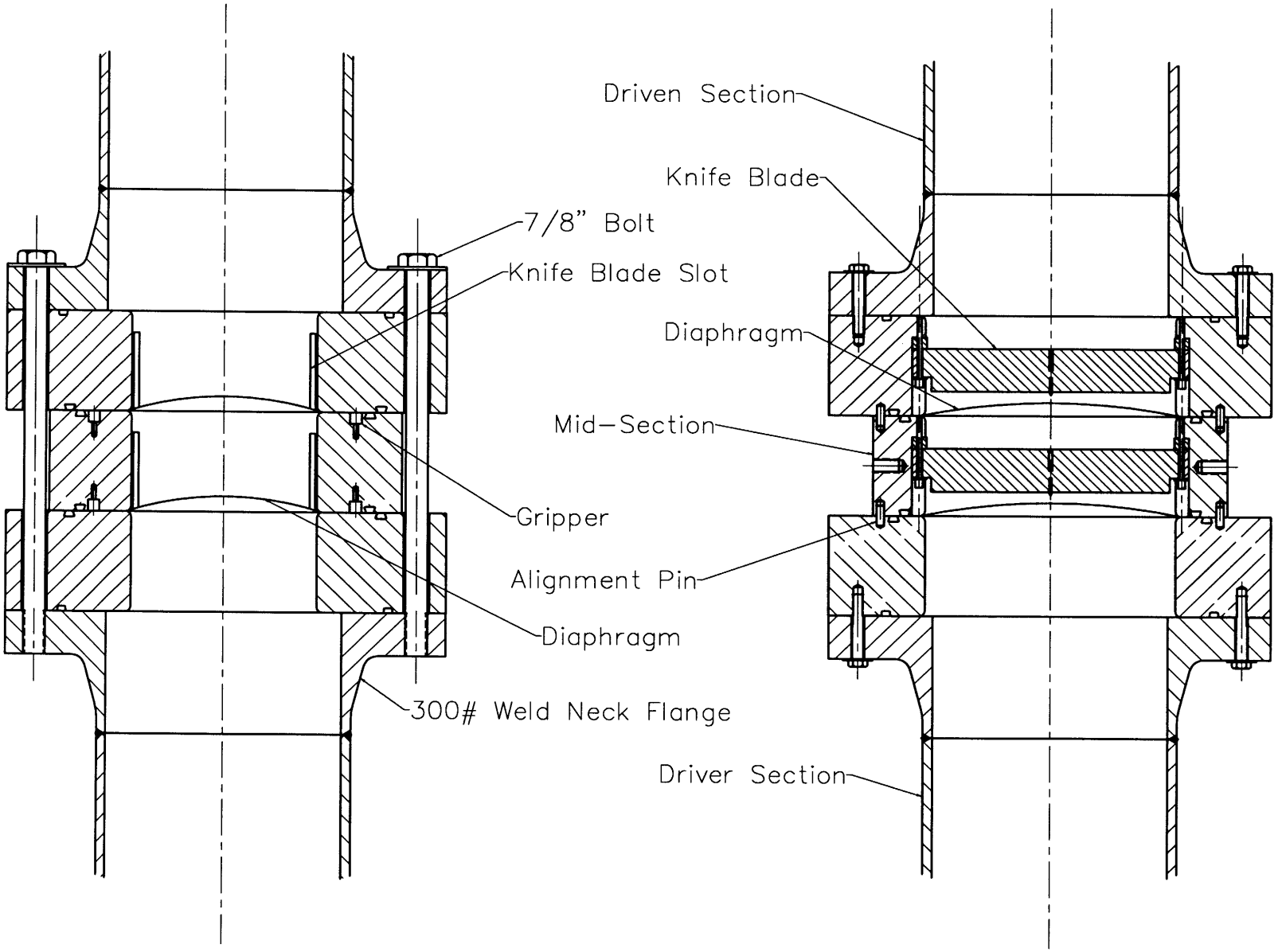

Figure 4-4: Schematic of the primary diaphragm assembly.

4.2.3 The Knife Blades

Knife blades will be installed behind each diaphragm both to ensure clean petaling and control the burst pressure. This technique is commonly used in shock tubes employing thin diaphragms where diaphragm scoring techniques have proven unreliable.

The Knife Blade Design

The diaphragm will be cut by a set of two knife blades joined at right angles in a cruciform configuration (see Figure 4-5 or drawings GTL-116 and GTL-117). When the diaphragm presses against the blades, a crack will be initiated by a sharp pin at the knife blade center. This crack will propagate along the stress concentrations set up by the two blades, cutting the diaphragm into four even petals. This bursting method has a number of advantages over scribing techniques: [31]

- The diaphragm bursting pressure can be precisely controlled by adjusting the distance of the knife blades behind the diaphragm.
- The diaphragm will be cut into four even petals, minimizing the chance of losing fragments. Scribe marks have proven unreliable for diaphragms where $t_d/D_d < 0.001$.
- Opening times are minimized because no extra thickness is required for scribing. The diaphragm can therefore be ruptured at close to its natural bursting pressure.

A straight set of knife blades will be used so the diaphragm will be torn rather than cut close to the edges. If this presents a problem for large diaphragm-knife blade separations, a curved set of blades can be constructed to ensure clean cutting out to the edges.

Knife Blade Retainers and Adjustment

The axial location of the knife blades can be adjusted to provide precise control over the diaphragm burst characteristics. Incremental changes in the burst pressure can be made by changing the diaphragm material or thickness. However, in order achieve a full range of shock speeds, fine adjustments in the burst pressure will need to be made by changing the position of the knife blades. When using a single diaphragm, this allows for accurate resolution of the burst pressure and corresponding shock strength. For the double diaphragm technique, where precise control of the burst pressure is not required, it allows for the burst

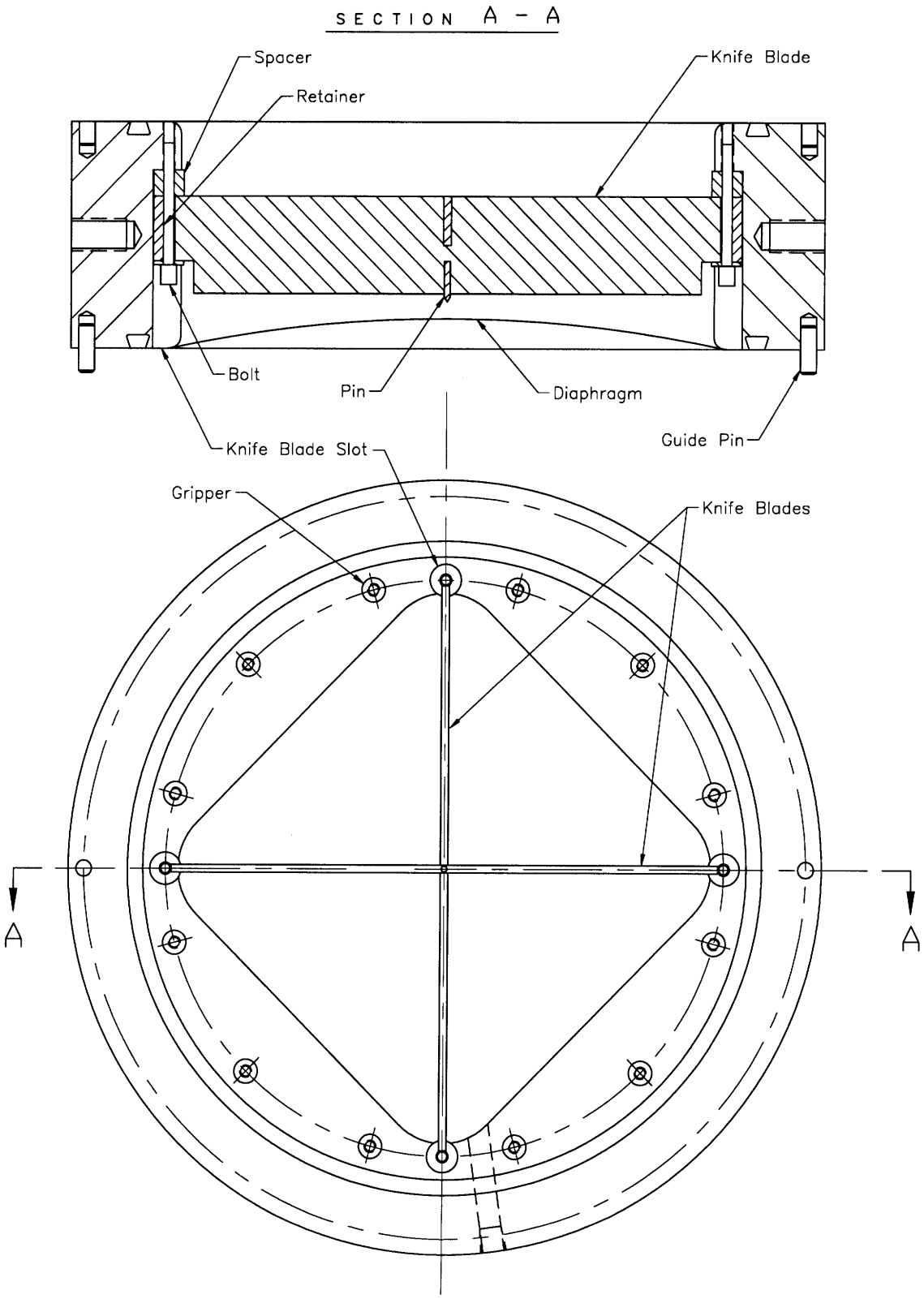

Figure 4-5: Cruciform knife blade schematic.

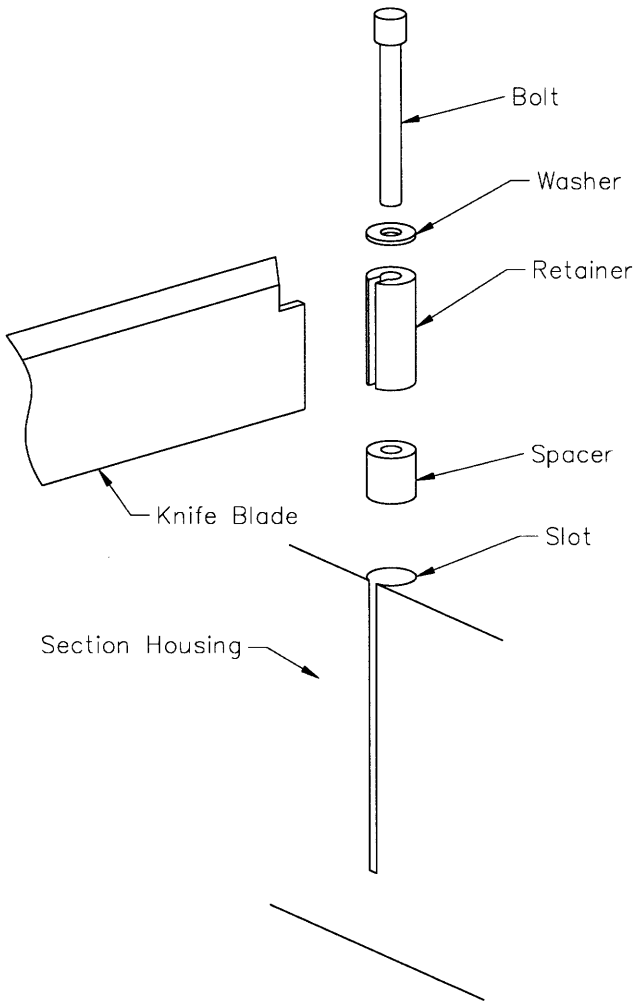

Figure 4-6: Exploded view of knife blade assembly.

pressure to be set close to the natural burst pressure of the diaphragm, thereby minimizing the diaphragm opening time.

The diaphragm adjustment system is shown in Figure 4-6. The cutter is held at the end of each blade by a slotted cylindrical retainer. These retainers fit into corresponding cylindrical slots in the mid-section housing and are bolted in place. The axial location of the blades can be adjusted by adding #10 washers or machined spacers in the slot underneath the retainers.

4.2.4 Cross Section & Transition

The primary diaphragm assembly is designed with a square internal cross section so that the diaphragm petals can fold along a straight edge. This avoids problems encountered with circular cross sections where petals tend to tear at the root. When operating near

the diaphragms natural bursting pressure, circular sections can cause petals to tear off completely, potentially damaging the nozzle or instruments downstream. A square cross section avoids this hazard, but the driven gas must pass from a circular to a square cross section and back again as it crosses over the diaphragm assembly. This will incur some pressure losses and result in a corresponding change in shock tube behavior. However, this region of the flow does not have a strong influence on shock attenuation or reservoir uniformity, so the effect on tube performance will be minimal [7].

The tube and primary diaphragm assembly cross sections have been overlaid in Figure 4-7. In order to minimize machining costs, an abrupt transition will be made between the different cross sections. This will result in flow separations and other effects that could be avoided by creating a smooth transition. In practice, however, the flow over the diaphragm section does not have enough of an effect on performance to warrant the additional construction costs. The square corners were replaced by a $1''$ radius in order to minimize the step heights and change in cross sectional area. As a result, the maximum step height will less than $0.7''$ and the total area change, A_{PDA}/A_{st}, including knife blades blockage, approximately 0.83.

4.2.5 Diaphragm Retention

Carbide-tipped grippers were added to the intermediate pressure section to prevent the diaphragm from being "drawn-in" under the pressure loads. In general, the clamping force of the two o-rings is sufficient to prevent any large movements. However, even a subtle drawing-in of the diaphragm will make calibrating the burst pressures difficult. So, to make the test conditions as repeatable as possible, the diaphragm must be held rigidly between the flanges.

In order to accomplish this, 12 grippers will be installed inside the o-ring circle. Each gripper will be recessed into a 3/8" hole such that the height of the teeth above the surface can be adjusted from $0''$ to $1/16''$ using a stack of $0.005''$ washers. This technique was found to be effective in a previous $6''$ shock tunnel [21].

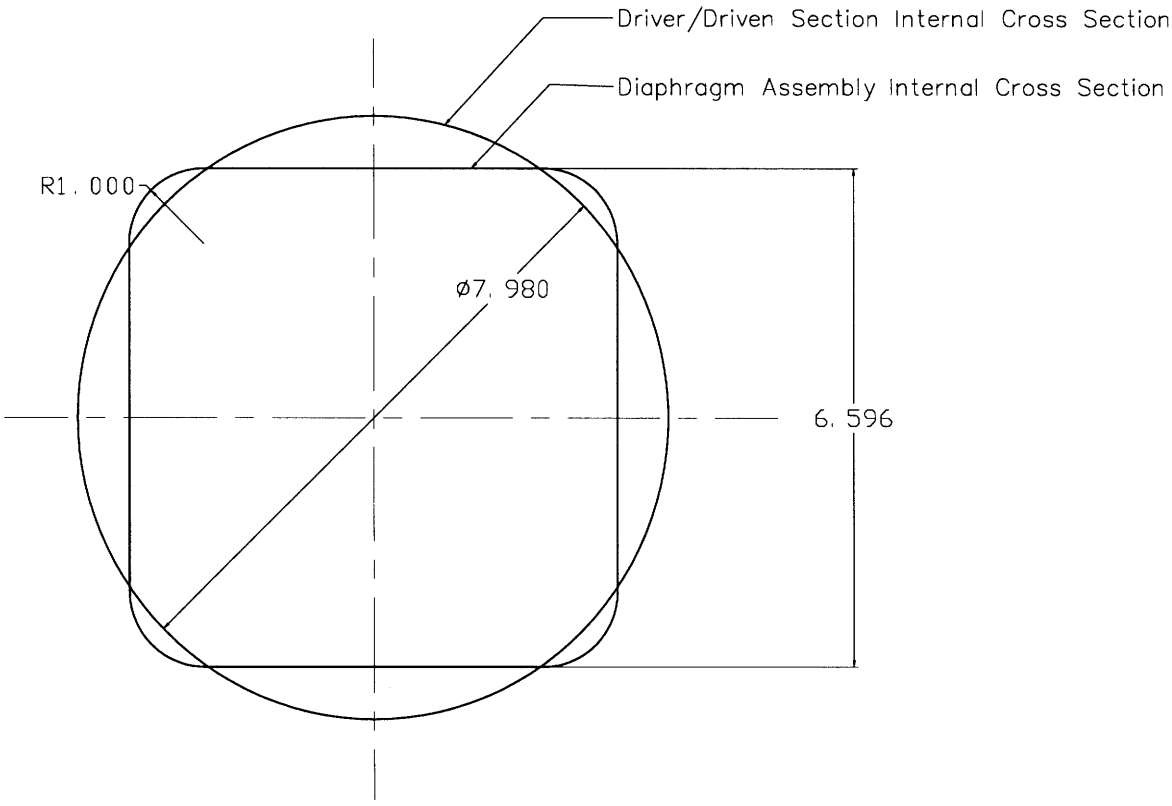

Figure 4-7: Primary diaphragm assembly cross section.

4.3 Secondary Diaphragm/Nozzle Assembly

Figure 4-8 shows a schematic of the secondary diaphragm/nozzle assembly. The nozzle will be mounted on a $3/4''$ end-plate, and aerodynamic farings can be added to ensure clean entrainment of the secondary flow. This plate will also be used to clamp a secondary diaphragm against a $3/8''$ support disc. The whole assembly will be held in place by circle of $7/8''$ bolts.

4.3.1 Secondary Diaphragm

The secondary diaphragm assembly consists of a thin sheet of acetate clamped between the end-plate and the $3/8''$ support disc (see Figure 4-8). The diaphragm serves the purpose of separating the test gas from the atmosphere. This enables the driven section to initially be below atmospheric pressure and also allows for test gases other than air to be used or seeding for diagnostic techniques to be added. The loading on the secondary diaphragm is only a fraction of that of the primary, with a typical $\Delta p = p_a - p_1 \approx 13\ psi$ for HSCT experiments. As a result, thin plastic diaphragms, such as cellophane or acetate, can be

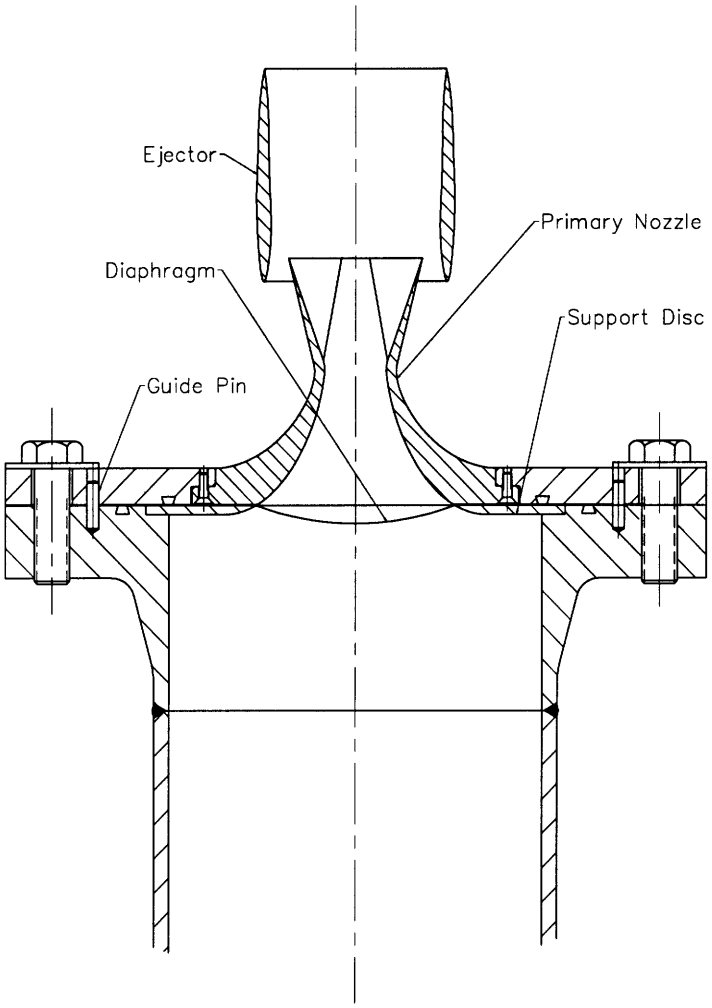

Figure 4-8: Driven section end-plate schematic.

employed.

Acetate is an ideal diaphragm material when high strength is not required because it shatters into small pieces under shock loads. When the shock wave reflects off the end-plate, the diaphragm will burst and the fragments will be convected out from the nozzle. This avoids the petaling problems encountered with the primary diaphragm and eliminates the need for knife blades or a square cross section. There will be no petals left over to interrupt the flow, but there may be a jagged edge where the diaphragm tears away from the clamp. To prevent this from distorting the nozzle inlet flow, the inside diameter of the support disk must be sufficiently large compared to that of the nozzle.

4.4 Mechanical Changes for 12″ Shock Tube Facility

Much of the mechanical design for the 8″ shock tube can be scaled and applied directly to the 12″ facility. However, some additions will be required; flanged tube sections will be needed to extend the overall length to 60′, and the horizontal orientation will necessitate a new system for accessing the diaphragms. Similarly, some parts, such as the diaphragm assemblies, would be prohibitively heavy if kept geometrically similar and therefore need to be modified. The following changes will be required:

Driver and Driven Sections

- *Tube Sections:* Additional 6′ and 14′ flanged pipe sections will be required to extend the driver and driven section lengths.

- *Flanges:* Modifications to the flanges will be needed if the extension sections are to be interchangeable (see Section 4.1). Alignment schemes (pilots, guide pins, etc.) will need to be made consistent.

- *Lifting Lugs:* The horizontal orientation of the shock tube will require a new system for supporting and moving the tube sections. There are several options: (1) the tube could be supported from the ceiling using standard pipe rollers. (2) an I-beam could be bolted to the ceiling to act as a track for casters fixed to the tube sections. (3) Scaffolding can be built up from the laboratory floor to support the tube from underneath.

- *Instrumentation Ports:* Only minor changes will be required to adapt the ports to a 12″ diameter tube.

- *Gas Fill/Vacuum Ports:* No major changes are required, but the ports may need to be resized to accommodate the increased vacuum pump capacity.

Primary Diaphragm Assembly

- *Knife Blade Assembly:* The design can be scaled up to the 12″ diameter so long as allowances are made for the increased diaphragm deflections.

- *Section Housings:* Both the length and diameter of the housings will need to be increased. This would be prohibitively heavy using the 8″ tube design, so a new scheme will be required.

Secondary Diaphragm Assembly

- The secondary diaphragm assembly will also be prohibitively heavy if scaled directly (a 12″, 300# blind flange alone weighs 184 *lbs*). A new design could be devised in which the secondary diaphragm is located on the outside of the end-plate, allowing the blind flange to remain in place.

Base Stand

- The one disadvantage of the 12″ facility is that the loads will not be carried directly by the foundation. There are two possible solutions for supporting the loads: (1) the driven section can be braced to a wall or the ceiling in a way that distributes the shock loads or (2) the entire shock tube can be placed on rollers so that it is free to recoil. An analysis of the tube dynamics will be needed to establish the trade-offs between the two options.

Chapter 5

Closure

5.1 Summary

The design of an acoustic shock tube for jet noise research has been presented. Such a device has a number of strengths; it is mechanically simple, versatile, has low operating costs, and can generate acoustic and fluid dynamic data comparable to that of steady-state facilities. In addition, a shock tube has a number of inherent advantages over its steady-state counterparts:

- Total temperature and pressure profiles at the nozzle inlet will be uniform as a result of shock heating. Thus the jet noise does not contain the core noise often present in steady-state, vitiated air facilities.
- The short run times allow for heat sink nozzles to be employed. Therefore, relatively inexpensive stereo-lithography models can be used for tests at realistic flow conditions.
- The use of rapid-prototyping methods, such as stereo-lithography, enable parametric testing to be performed more economically and faster than in steady-state facilities.
- The absence of core noise reduces the averaging time required for noise power spectrum measurements. Between 4 and 12 shock tube runs will be sufficient to resolve the frequencies to within ± 1 dB.
- The operation of the facility will be inexpensive, each run requiring only a single operator, three diaphragms, and about 150 ft^3 of helium and argon gas.

- With adequate vacuum pumping capabilities, tests can be conducted rapidly. Repetitive runs would each take less than one hour.

Two different potential shock tube configurations were investigated: (1) an $8''$ diameter, $38'$ long, vertical shock tube with a $16' \times 19'$ test cell and (2) a $12''$ diameter, $60'$ long, horizontal shock tube with a $19' \times 26'$ test cell. The $12''$ shock tube, however, has a number of advantages over the $8''$ shock tube. The length and diameter will be 50% larger than those of the vertical shock tube, increasing both the test time and maximum nozzle size. In addition, the test cell is larger and the shock tube can be strategically oriented to maximize the distance to the microphones. The advantages of this facility can be summarized as follows:

- The increased shock tube length extends the duration of constant reservoir conditions to roughly 25 ms at the design point.
- The greater tube diameter and test gas volume allow nozzles up to $1/12^{th}$ the scale of the HSCT to be tested.
- The microphones can be placed $208''$ from the nozzle exit, eliminating the need for near-field corrections for the size nozzles to be tested.
- A full range of directivity angles, $60° < \psi < 160°$, can be covered without moving the shock tube.
- The horizontal orientation of the shock tube eliminates the need for counterweights and spur gears, simplifying access to the diaphragm.

The performance of the $12''$ facility is presented below for a typical mixer/ejector nozzle at roughly $1/12^{th}$ the scale of the HSCT. The nozzle has a 21.2 in^2 ejector exit area ($D_{eq} = 5.2''$), a primary stream Mach number of 1.2, and a primary nozzle throat area of 9.1 in^2.

- Test time: 16.1 ms (25.7 ms of constant reservoir conditions $-$ 11.4 ms for jet to develop to a length of $7D_e$)
- Maximum measurable frequency: 80 kHz, corresponding to 6.7 kHz full scale.
- Distance to microphones: $R_{mic} = 40D_e$ for downstream arc, $R_{mic} = 35D_e$ at sideline.

- Total required test time: 108 ms (7 shots) to resolve noise power spectrum measurements to within ± 1 dB of mean at a full scale bandwidth of 116 Hz. (80% confidence)

These capabilities would complement those of steady-state facilities, and would be advantageous for the testing of small scale nozzles.

5.2 Conclusion

When built, this facility will allow issues of jet noise suppressor design to be explored in a low cost facility ideally suited for a university environment. Analytical estimates of the performance show that fluid mechanic and acoustic data can be obtained that is comparable to that from steady-state facilities. Furthermore, the short duration of the test enables nozzles to be made using inexpensive, rapid-prototyping methods such as stereo lithography. Parametric testing can therefore be performed more economically and faster than in steady-state facilities. Such a tool will provide valuable data on the impact of noise suppressor geometry changes on both fluid mixing and far-field noise. With such an understanding of the fluid mechanics and acoustics, it is possible to design mixer geometries that not only to increase the rapidity and spatial uniformity of the mixing process but also tailor the flow structures responsible for mixing, thus affecting the magnitude, directivity and frequency of the radiated noise.

Bibliography

[1] A. Brabbs and Frank E. Belles. Contact-surface tailoring in real shock tubes. page 955. Proceedings of the 5^{th} International Symposium on Shock Tubes and Shock Waves, 1965.

[2] A. B. Britan, A. Ya. Rudintskii, and A. M. Starik. Parameter formation behind the reflected wave in a shock tube with a nozzle. *Journal of Fluid Dynamics*, 22:622–628, 1987.

[3] David Davidson. *Personal communication.* 1995.

[4] A. Dravet, J. Julliard, and M. Ah-Fa. Jet noise experimental studies of two exhaust concepts for hsct application. Technical Report CEAS/AIAA-95-148, AIAA, 1995.

[5] J. K. Elliot, T. A. Manning, Y. J. Qiu, E. M. Greitzer, C. S. Tan, and T. G. Tillman. Computational and experimental studies of flow in multi-lobed forced mixers. Technical Report AIAA-92-3568, AIAA/SAE/ASME/ASEE 28^{th} Joint Propulsion Conference, 1992.

[6] A. Fung. Modeling of mixer-ejector nozzle flows. Master's thesis, Massachusetts Institute of Technology, 1995.

[7] I. I. Glass. Theory and performance of simple shock tubes. Technical Report 12, UTIA, 1958.

[8] Jay C. Hardin. Introduction to time series analysis. Technical Report RP1145, NASA, 1986.

[9] R. A. Hartunian, A. L. Russo, and P. V. Marrone. Boundary layer transition and heat transfer in shock tubes. *Journal of Aerospace Science*, 27:587, 1960.

[10] S. Hickman and J. B. Kyser. Refinements in high-reynolds number shock-tunnel technology. *AIAA Journal*, pages 961–967, 1973.

[11] U. Ingard. *Personal communication.* 1995.

[12] J. L. Kerrebrock. *Aircraft Engines and Gas Turbines.* The MIT Press, 1992.

[13] J. K. Krasnodebski. Numerical investigations of lobed mixer flow fields. Master's thesis, Massachusetts Institute of Technology, 1995.

[14] H. W. Liepmann and A. Roshko. *Elements of Gasdynamics.* John Wiley & Sons, Inc., 1957.

[15] G. M. Lilley. Jet noise classical theory and experiments. Technical Report RP-1258, NASA, 1991.

[16] W. K. Lord, C. W. Jones, A. M. Stern, V. L. Head, and E. A. Krejsa. Mixer ejector nozzle for jet nose supression. Technical Report AIAA-90-1909, AIAA, 1990.

[17] Jean F. Louis. A systematic study of supersonic jet noise. Technical Report DOT-TSC-142-1, Department of Transporstation, 1971.

[18] Herman Mark. The interaction of a reflected shock wave with the boundary layer in a shock tube. *Journal of Aeronautical Sciences*, pages 304–306, 1957.

[19] W. A. Martin. An experimental study of the boundary layer behind a moving plane shock wave. Technical Report 47, UTIA, 1957.

[20] Eugene F. Megyesy. *Pressure Vessel Handbook.* Pressure Vessel Handbook Publishing Inc., 1972.

[21] M. Miller. *Personal communication.* 1995.

[22] H. Mirels. Attenuation in a shock tube due to unsteady boundary-layer action. Technical Report RP-1333, NACA, 1957.

[23] H. Mirels. Boundary layer growth effects in shock tubes. *Shock Tube Research-Proceedings of the 8th International Shock Tube Symposium*, 1971.

[24] R. Mirels and J. Kyser. The reflection of shock waves from an orifice at the end of a duct. Technical Report 72-996, AIAA, 1972.

[25] Herbert Oertel. Jet noise research by means of shock tubes. In *Modern Developments in Shock Tube Research*, page 488. Proceedings of the 10^{th} International Syposium on Shock Tubes and Waves, 1975.

[26] Robert K. Otnes. *Digital Time Series Analysis.* John Wiley & Sons, Inc., 1972.

[27] Terry Parker. *Personal communication.* 1995.

[28] Clemans A. Powell and James M. Fields. Human response to aircraft noise. Technical Report RP-1258, NASA, 1991.

[29] W. M. Presz and E. M. Greitzer. Forced mixer lobes in ejector designs. Technical Report AIAA-88-3001, AIAA, 1988.

[30] H. Reichardt. *Gesetzmäßigkeiten der freien Turbulenz.* VDI-Forschungsheft, 1942.

[31] A. Roshko and D. Baganoff. A novel device for bursting shock-tube diaphragms. *Physics of Fluids*, 4:1445, 1961.

[32] H. Schlichting. *Boundary-Layer Theory.* McGraw-Hill, Inc., 1955.

[33] J. Seiner. *Personal communication.* 1995.

[34] J. Seiner. *Personal communication.* 1996.

[35] D. E. Tew. A computational study of mixing downstream of a lobed mixer with a velocity difference between the co-flowing streams. Master's thesis, Massachusetts Institute of Technology, 1992.

[36] D. S. Underwood. Effec of heat release on streamwise vorticity enhanced mixing. Master's thesis, Massachusetts Institute of Technology, 1995.

[37] F. M. White. *Viscous Fluid Flow.* McGraw-Hill, Inc., 1974.

Appendix A

Gas Dynamic Model

A.1 Fundamental Gas Dynamic Equations

There are a number of fundamental gas-dynamic relations that are used as the basis for deriving the governing shock tube equations. A detailed description of these equations can be found in Liepmann and Roshko [14]. However, for completeness, the relevant relations will be outlined here.

The normal shock relations are most easily described in a shock stationary frame, so a change of reference will typically be employed to describe moving shocks (see Figure A-1). In this frame, the jump conditions can be related to each other or to the fluid Mach number on each side of the shock. Frequently the pressure ratio across the shock, p_2/p_1, is the most convenient independent parameter. For example, the density and temperature ratios across the shock can be described by the Rankine-Hugonoit relations:

$$\frac{\rho_2}{\rho_1} = \frac{u_1'}{u_2'} = \frac{1 + \frac{\gamma+1}{\gamma-1}\frac{p_2}{p_1}}{\frac{\gamma+1}{\gamma-1} + \frac{p_2}{p_1}} \tag{A.1}$$

$$\frac{T_2}{T_1} = \frac{p_2}{p_1}\frac{\frac{\gamma+1}{\gamma-1} + \frac{p_2}{p_1}}{1 + \frac{\gamma+1}{\gamma-1}\frac{p_2}{p_1}} \tag{A.2}$$

where u' denotes the fluid velocity relative to the stationary shock.

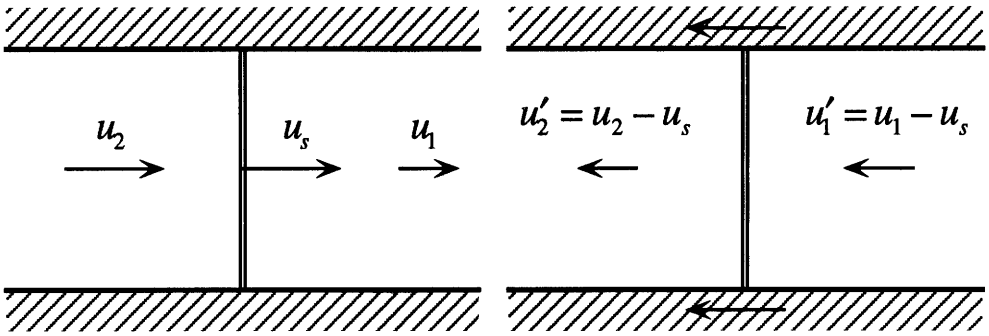

(a) Laboratory reference frame (b) Shock stationary reference frame

Figure A-1: Change of reference used to simplify analysis of moving shocks

Similarly, for a perfect gas, p_2/p_1 can be related to the shock Mach number by

$$M_1 = \frac{u_1'}{a_1} = \left(\frac{\gamma - 1}{2\gamma} + \frac{\gamma + 1}{2\gamma}\frac{p_2}{p_1}\right)^{\frac{1}{2}} \tag{A.3}$$

Combining Equations A.3 and A.1 gives a relation for the velocity change across the shock:

$$\Delta u = \frac{a_1}{\gamma}\left(\frac{p_2}{p_1} - 1\right)\left[\frac{2\gamma}{(\gamma+1)\frac{p_2}{p_1} + (\gamma - 1)}\right]^{\frac{1}{2}} \tag{A.4}$$

where $\Delta u \equiv u_1 - u_2 = u_1' - u_2'$. This velocity change can also be described in terms of the shock Mach number:

$$\frac{\Delta u}{a_2} = \frac{2}{\gamma_1 + 1}\left[M_s - \frac{1}{M_s}\right] \tag{A.5}$$

Similarly, the velocity change across an expansion fan can be expressed as a function of the pressure drop across the fan

$$\Delta u = \frac{2a_1}{\gamma_1 - 1}\left[1 - \left(\frac{p_2}{p_1}\right)^{\frac{\gamma_1 - 1}{2\gamma_1}}\right] \tag{A.6}$$

These expressions provide the basic tools from which the the ideal gas-dynamic model of the shock tube is derived.

A.2 Derivation of the Shock Tube Model

The ideal gas-dynamic model of the shock tube was derived using a number of simplifying assumptions. Most of these assumptions are valid for the temperature and pressure ranges that will be employed in the shock tube. Some of the non-ideal behaviors, however, significantly affect the performance so corrections will need to be made to the ideal model. The ideal model assumptions are as follows:

- The diaphragm removal is assumed to be instantaneous, resulting in a step discontinuity in pressure between the two sections at $t = 0$. Any effects due to the diaphragm curvature or finite bursting time are ignored.
- There is assumed to be no mixing between the two gases such that a distinct contact surface exists at the interface between them.
- The flow is assumed to be inviscid, except across the shock. This is generally a poor assumption because the boundary layer that results along the tube walls has a significant effect.
- One-dimensional flow is assumed throughout the tube. The three-dimensional effects associated with diaphragm bursting or the nozzle flow are ignored.
- Real-gas effects are ignored and γ is assumed to be constant for each gas.

A schematic of the shock tube time-distance history is presented in Figure A-2.

Basic Shock Tube Equation

At $t = 0$ the diaphragm is removed, resulting in a step change in pressure between the expansion and compression sections. This discontinuity will resolve in to a shock propagating through the low pressure section, and an expansion fan propagating through the driver gas. If the strength of the shock is expressed as p_2/p_1, then the velocity behind the shock, u_2, comes directly from Equation A.7:

$$u_2 = a_1 \left(\frac{p_2}{p_1}\right) \sqrt{\frac{2/\gamma_1}{(\gamma_1 + 1)p_2/p_1 + (\gamma_1 + 1)}} \tag{A.7}$$

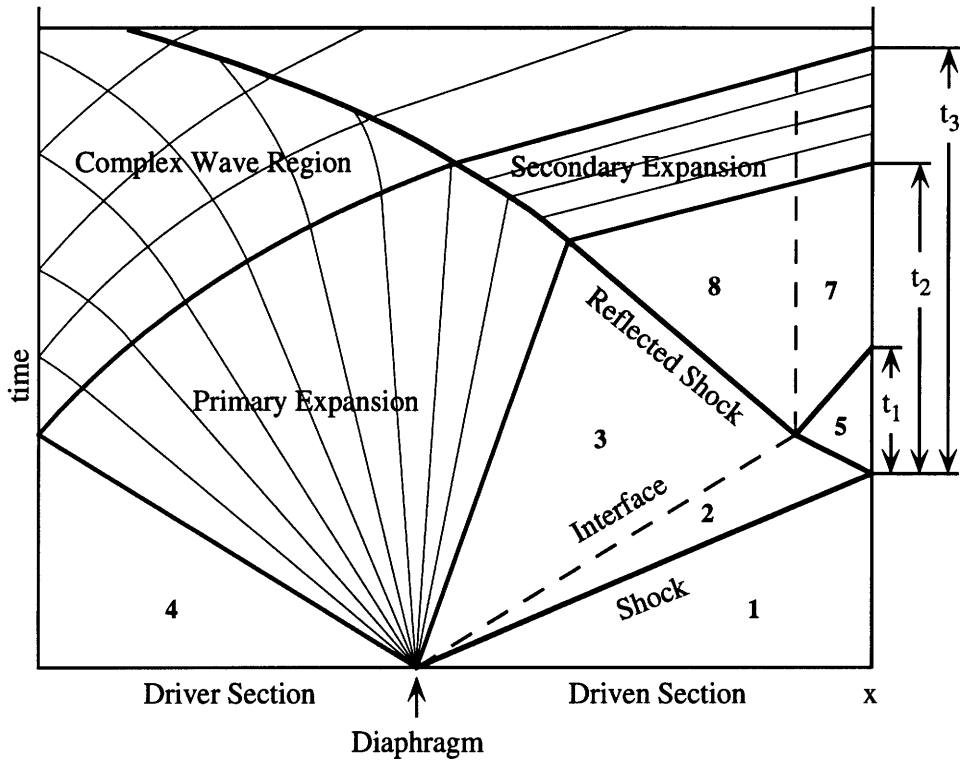

Figure A-2: Time-Distance History of Wave System in Shock Tube

Likewise, the velocity behind the expansion, u_3, can be expressed as a function of p_3/p_4 from Equation A.6:

$$u_3 = \frac{2a_4}{\gamma_4 - 1}\left[1 - \left(\frac{p_3}{p_4}\right)^{\frac{\gamma_4 - 1}{2\gamma_4}}\right] \tag{A.8}$$

There can exist a discontinuity in temperature and density between regions 2 and 3, but the pressure and velocity must be continuous across the contact surface. So, by imposing that $p_2 = p_3$ and $u_2 = u_3$, Equations A.7 and A.8 can be combined to give the basic shock tube equation:

$$\frac{p_4}{p_1} = \frac{p_2}{p_1}\left[1 - \frac{(\gamma_4 - 1)(a_1/a_4)(p_2/p_1 - 1)}{\sqrt{2\gamma_1}\sqrt{2\gamma_1 + (\gamma_1 + 1)(p_2/p_1 - 1)}}\right]^{\frac{-2\gamma_4}{\gamma_4 - 1}} \tag{A.9}$$

The shock speed, c_s, and the parameters in region 2 can now be found from the normal shock relations presented in Section A.1.

The expansion fan can also be characterized at this point. The head of the expansion will propagate into the driver section at a speed of $-a_4$ while the tail trails at a velocity

$u_3 - a_3$. The strength of the expansion can be related to that of the shock by

$$\frac{p_3}{p_4} = \frac{p_3}{p_1}\frac{p_1}{p_4} = \frac{p_2/p_1}{p_4/p_1} \tag{A.10}$$

and the temperature in region 3 may be found from the isentropic relation

$$\frac{T_3}{T_4} = \left(\frac{p_3}{p_4}\right)^{\frac{\gamma_4-1}{\gamma_4}} \tag{A.11}$$

This characterizes all the waves directly initiated by the diaphragm bursting.

Parameters Behind the Reflected Shock Including Nozzle Effects

After the shock reflects from the end wall, a steady drift velocity will be established in the reservoir (region 5) due to the massflow through the nozzle. Ignoring three-dimensional effects at the nozzle inlet, this drift velocity can be found from one-dimensional nozzle theory. The mass flow through the nozzle can be written [12]

$$\dot{m} = (\rho u A)^* = \rho_t a_t A^* \left(\frac{2}{\gamma+1}\right)^{\frac{\gamma+1}{2(\gamma-1)}} \tag{A.12}$$

Equating this to the axial flow in the reservoir, $\dot{m} = \rho_5 u_5 A_{st}$, gives a relation for the drift Mach number:

$$M_5 = \left[1 + \frac{\gamma-1}{2}\right]^{-\frac{\gamma+1}{2(\gamma-1)}} \left[\frac{\rho_{t_5}}{\rho_5}\right] \left[\frac{T_{t_5}}{T_5}\right]^{\frac{1}{2}} \left[\frac{A^*}{A_{st}}\right] \tag{A.13}$$

Notice that M_5 is only a function of γ and the nozzle area ratio (ρ_t/ρ_5, $T_t/T = f(M,\gamma)$). Combining Equation A.13 with Equation A.5 gives a relation for the reflected shock Mach number:

$$\frac{\Delta u}{a_2} = M_2 - M_5\frac{a_5}{a_2} = \frac{2}{\gamma_1+1}\left[M_r - \frac{1}{M_r}\right] \tag{A.14}$$

Where $a_5 = f(M_r)$ so Equation A.14 must be solved iteratively to get a value for M_5.

In the limiting case that $A^*/A = 0$, the reflected shock Mach number can be found

explicitly. Imposing that $u_5 = 0$ gives the relation for M_r

$$M_r = \frac{1}{M'_{2(s)}} \tag{A.15}$$

where $M'_{2(s)} = a_2/(u_2 - u_s)$ is the Mach number of the fluid in region 2 relative to the incident shock. Likewise, in this limiting case the reservoir temperature and pressure ratios are simple functions of the incident shock Mach number:

$$\frac{T_5}{T_1} = \frac{[2(\gamma_1 - 1)M_s^2 + (3 - \gamma_1)]\,[(3\gamma_1 - 1)M_s^2 - 2(\gamma_1 - 1)]}{(\gamma_1 + 1)^2 M_s^2} \tag{A.16}$$

$$\frac{p_5}{p_1} = \left[\frac{2\gamma_1 M_s^2 - 1(\gamma_1 - 1)}{(\gamma_1 + 1)}\right]\left[\frac{(3\gamma_1 - 1)M_s^2 - 2(\gamma_1 - 1)}{(\gamma_1 - 1)M_s^2 + 2}\right] \tag{A.17}$$

To find the velocity of the reflected shock relative to the inertial reference frame, a transformation must be made from shock stationary coordinates. U_{rs} can be expressed as:

$$u_{rs} = u_2 - u'_{2(rs)} = u_2 - M_{rs}a_2 \tag{A.18}$$

where $u'_{2(rs)}$ is the fluid velocity ahead of the reflected shock in the shock stationary frame.

Interaction of the Reflected Shock with the Contact Surface

When the shock crosses the interface between (2) and (3), there are three possible interactions depending on the shock strength, p_5/p_2, and the speed of sound and γ in each region.

- No change in shock strength and a reflected Mach wave.
- A strengthening of the shock across across the interface and a reflected shock.
- A weakening of the shock and a reflected expansion.

In all cases, the strength of the transmitted and reflected waves can be found with a similar derivation to that of the basic shock tube equation. First, the conservation equations are applied to an infinitesimal volume surrounding the contact surface. This imposes that $u_7 = u_8$ and $p_7 = p_8$. In the first case, when there is no significant reflected disturbance,

the conditions in regions 5 and 7 will be the same. Thus, the shock strength will be unchanged ($p_8/p_3 = p_5/p_2$) and the velocity change across the shock must remain constant ($\Delta u_{rs} = \Delta u_{ts}$). Combining these relations with equation A.4 gives the "tailoring condition":

$$\frac{\gamma_2}{a_2^2}\left[(\gamma_2+1)\frac{p_5}{p_2}+\gamma_2-1\right] = \frac{\gamma_3}{a_3^2}\left[(\gamma_3+1)\frac{p_5}{p_2}+\gamma_3-1\right] \tag{A.19}$$

If this condition is met, there will be no reflected disturbance resulting in a significantly augmented test time.

If the tailoring condition is not met, there will be a reflected disturbance. In the case that

$$\frac{\gamma_2}{a_2^2}\left[(\gamma_2+1)\frac{p_5}{p_2}+\gamma_2-1\right] > \frac{\gamma_3}{a_3^2}\left[(\gamma_3+1)\frac{p_5}{p_2}+\gamma_3-1\right] \tag{A.20}$$

there will be a reflected shock. The strength of the transmitted and reflected shocks can be found by once again matching the velocities on each side of the interface. From Equation A.4 it can be shown that

$$u_8 = u_2 - \frac{a_3}{\gamma_4}\left(\frac{p_8}{p_3}-1\right)\left[\frac{\gamma_4+1}{2\gamma_4}\frac{p_8}{p_3}+\frac{\gamma_4-1}{2\gamma_4}\right]^{-\frac{1}{2}} \tag{A.21}$$

Likewise, the velocity behind the reflected shock can be written

$$u_7 = u_5 + \frac{a_5}{\gamma_1}\left(\frac{p_7}{p_5}-1\right)\left[\frac{\gamma_1+1}{2\gamma_1}\frac{p_7}{p_5}+\frac{\gamma_1-1}{2\gamma_1}\right]^{-\frac{1}{2}} \tag{A.22}$$

Equating these two and imposing that

$$\frac{p_7}{p_5} = \frac{p_8/p_3}{p_5/p_2} \tag{A.23}$$

from equilibrium across the interface gives an expression for the transmitted shock strength. Substituting this result back into the above equations will give the value for the parameters in region 7 and 8 as well as the reflected shock strength.

Similarly, in the case that

$$\frac{\gamma_2}{a_2^2}\left[(\gamma_2+1)\frac{p_5}{p_2}+\gamma_2-1\right] < \frac{\gamma_3}{a_3^2}\left[(\gamma_3+1)\frac{p_5}{p_2}+\gamma_3-1\right] \tag{A.24}$$

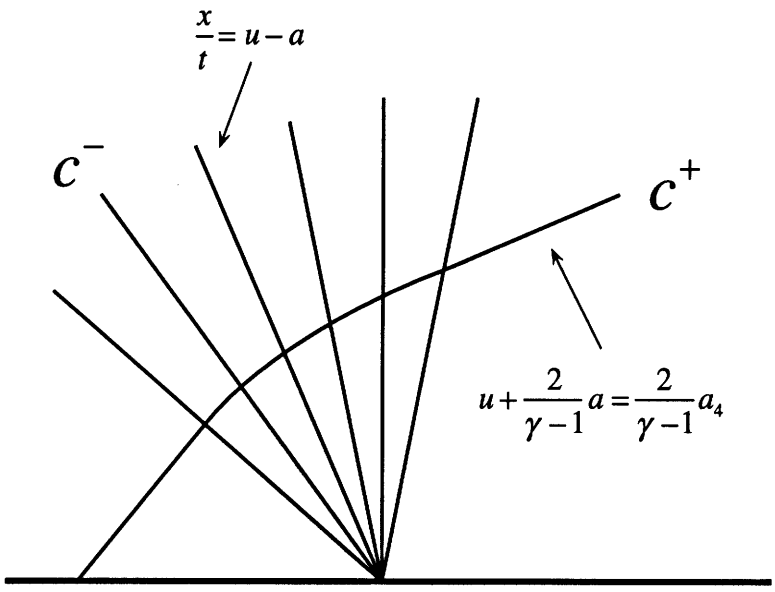

Figure A-3: Primary Expansion Fan and Characteristics

the reflected disturbance will be an expansion fan. The solution in this case in analogous to that of the reflected shock, except for the expression for the velocity in region 7 which is instead (Equation A.6)

$$u_7 = \frac{2a_5}{\gamma_1 - 1}\left[1 - \left(\frac{p_7}{p_5}\right)^{\frac{\gamma_1 - 1}{2\gamma_1}}\right] \tag{A.25}$$

The other parameters are obtained from this relation as before.

Conditions Across the Centered Expansion

The conditions across the simple region of the centered expansion can be found by employing the method of characteristics. For a wave traveling in the $-x$ direction and centered at the origin, the c^+ characteristic can be described by

$$\frac{dx}{dt} = u + a \tag{A.26}$$

$$u + \frac{2}{\gamma - 1} a = \frac{2}{\gamma - 1} a_4 \tag{A.27}$$

The c^- characteristics will be straight lines and can similarly be described by

$$\frac{dx}{dt} = \frac{x}{t} = u - a \tag{A.28}$$

Combining Equations A.27 and A.28 gives an expression for the fluid velocity and local speed of sound everywhere in the simple wave region:

$$a = \frac{2a_4 - (\gamma_4 - 1)\frac{x}{t}}{\gamma_4 + 1} \tag{A.29}$$

$$u = \frac{2}{\gamma_4 + 1}\left(\frac{x}{t} + a_4\right) \tag{A.30}$$

Time-Distance History of the Centered Expansion

The time-distance history of the expansion fan can be found by following the trajectory of the wave head and tail. Mach waves travel at the local speed of sound relative to fluid medium; therefore, in any region of constant velocity and temperature, the path of the waves will appear as straight lines on a time-distance diagram. The expansion head, for instance, will initially travel at a velocity $u = -a_4$ and the expansion tail at $u = u_2 - a_3$.

After the expansion head reflects from the driver end-wall, it will encounter a gradient in both fluid velocity and temperature. As a result, the wave will no longer follow a straight path. In order to find an expression for the expansion head trajectory, the method of characteristics is once again employed. Combining Equations A.26, A.27, and A.28 gives the relation

$$\frac{dx}{dt} + \frac{\gamma - 3}{\gamma + 1}\frac{x}{t} - \frac{4}{\gamma + 1}a_4 = 0 \tag{A.31}$$

which will describe the path of the c^+ characteristic crossing the simple wave region. Integrating this equation from $x = -L_{dr}$, $t = L_{dr}/a_4$ gives the trajectory of the expansion head as it crosses the expansion fan after reflecting from the end-wall:

$$-\frac{x}{L_{dr}} = \frac{\gamma_4 + 1}{\gamma_4 - 1}\left(\frac{a_4 t}{L_{dr}}\right)\left[\left(\frac{a_4 t}{L_{dr}}\right)^{-2\frac{\gamma_4 - 1}{\gamma_4 + 1}} - \frac{2}{\gamma_4 + 1}\right] \tag{A.32}$$

The expansion head will follow this path until crosses the expansion tail into region (3).

The time and location of this intersection is given by

$$\left(\frac{a_4 t}{L_{dr}}\right)_B = \left(\frac{p_4}{p_3}\right)^{\frac{\gamma+1}{4\gamma}} \tag{A.33}$$

$$\left(-\frac{x}{L_{dr}}\right)_B = \frac{2}{\gamma-1}\left[\frac{\gamma+1}{2}\left(\frac{p_3}{p_4}\right)^{\frac{\gamma-1}{2\gamma}} - 1\right]\left(\frac{p_3}{p_4}\right)^{\frac{\gamma-1}{4\gamma}} \tag{A.34}$$

The expansion head will then follow straight paths at a velocity $u + a$ through regions (2), (7), and (8) to the end of the tube.

Shock-Expansion Interaction

In many cases, the reflected shock wave will overtake the tail of the centered expansion. In this event, the shock will encounter an adverse pressure gradient as well as a reduction in adverse velocity. As a result, the shock will be attenuated and a weak reflected expansion will result. Although the shock is weaker, the reduction in adverse velocity, and the increase in sonic speed will result in the acceleration of the shock.

The shock speed and jump conditions across the shock can be found at any point in the centered expansion using the following relations. First, the shock speed is defined as

$$u_s = u_a - M_t a_a \tag{A.35}$$

where the conditions at a can be found from Equations A.30 and A.29. The local speed of sound on each side of the shock can be found from the normal shock relations:

$$\left(\frac{a_b}{a_a}\right) = \frac{\left(\gamma_4 M_t^2 - \frac{\gamma_4-1}{2}\right)^{\frac{1}{2}}\left(\frac{\gamma_4-1}{2}M_t^2 + 1\right)^{\frac{1}{2}}}{\left(\frac{\gamma_4+1}{2}\right)M_t} \tag{A.36}$$

Similarly, the velocity behind the shock can also be expressed as a function of the shock Mach number:

$$u_b - u_t = \left[\frac{1 + \frac{\gamma_4-1}{2}M_t^2}{\gamma_4 M_t^2 - \frac{\gamma_4-1}{2}}\right]^{\frac{1}{2}} a_b \tag{A.37}$$

Finally, employing the method of characteristics on the weak reflected expansion gives a

relation between the velocity and local speed of sound behind the shock:

$$u_b - \frac{2}{\gamma_4 - 1} a_b = u_8 - \frac{2}{\gamma_4 - 1} a_8 \tag{A.38}$$

This system of equations can be numerically solved to give an expression for the shock velocity at any point along its path through the centered expansion.

Appendix B

Boundary Layer Model

Using the shock stationary reference frame described in Chapter 2, the boundary layer is approximated as a steady flow over an apparently moving semi-infinite flat plate as shown in Figure 2-5. This model can be found in reference [7] along with a comparison to experimental data. Agreement with the experimental data was within 15% for $p_1 = 300$ $mmHg$ and $M_s = 1.58$.

In the transformed coordinate system, the steady state mass and momentum conservation equations can be written:

$$\int_0^\infty \rho v dy = \int_0^\infty \rho_2 v_2 dy \tag{B.1}$$

$$\int \tau_x dx = \int_0^\infty \rho_2 v_2^2 dy - \int_0^\infty \rho v^2 dy \tag{B.2}$$

Substituting Equation B.1 into Equation B.2 and integrating with respect to x gives an expression for the derivative of the momentum thickness with respect to x.

$$\frac{\tau_x}{\rho_2 v_2^2} = \frac{\partial}{\partial x} \int_0^\infty \frac{\rho v}{\rho_2 v_2} \left(1 - \frac{v}{v_2}\right) dy \equiv \frac{d\theta}{dx} \tag{B.3}$$

The velocity profile is assumed to follow a power-law profile. Relative to the stationary shock, the velocities can be described as

$$\left|\frac{v - v_1}{v_2 - v_1}\right| = \left(\frac{y}{\delta}\right)^{\frac{1}{n}} = \zeta^{\frac{1}{n}} \qquad 0 \leq \zeta \leq 1 \tag{B.4}$$

$$\left|\frac{v-v_1}{v_2-v_1}\right| = 1 \qquad 1 \leq \zeta \tag{B.5}$$

Where $n = 5$ has been found to produce the best correlation with experimental data for shock tube flows [19]. This velocity distribution can also be written as $\frac{u}{u_2} = \zeta^{\frac{1}{n}}$ in the laboratory frame.

The thermal boundary layer is similarly defined using the Crocco-Busemann relation between temperature and velocity. Typically this relation is used for laminar flows, however it is also a valid approximation for turbulent flows in the absence of a strong axial pressure gradient [37]. This relation can be written

$$\frac{T}{T_2} = \frac{T_w}{T_2} + \frac{T_r - T_w}{T_2}\left(\frac{u}{u_2}\right) - \frac{1}{2}PrEc\left(\frac{u}{u_2}\right)^2 \tag{B.6}$$

where Ec, the Eckert Number, is defined for a perfect gas as

$$Ec \equiv \frac{u_e^2}{C_{pe}T_e} = (1-\gamma)M_e^2 \tag{B.7}$$

Similarly, the adiabatic recovery temperature is described by

$$\frac{T_r}{T_2} \equiv 1 + \frac{1}{2}PrEc = 1 + Pr\frac{\gamma-1}{2}M_2^2 \tag{B.8}$$

where $Pr \approx 0.72$ for air. Substituting the above definitions into the Crocco-Busemann relation gives a relation for the temperature distribution in terms of known parameters.

$$\frac{T}{T_2} = \frac{\rho_2}{\rho} = \frac{T_w}{T_2}\left[1 + \left(\frac{T_r}{T_w} - 1\right)\zeta^{\frac{1}{n}} - \frac{T_2}{T_w}\left(\frac{T_r}{T_2} - 1\right)\zeta^{\frac{2}{n}}\right] \tag{B.9}$$

The displacement thickness, δ^*, and the momentum thickness, θ, can also be defined in the shock stationary coordinates:

$$\delta^* \equiv \int_0^\infty \left(1 - \frac{\rho v}{\rho_2 v_2}\right) dy \tag{B.10}$$

$$\theta \equiv \int_0^\infty \frac{\rho v}{\rho_2 v_2}\left(1 - \frac{v}{v_2}\right) dy \tag{B.11}$$

where both δ^* and θ will be negative due to the increase of mass flow in the boundary layer,

i.e. $\rho v \geq \rho_2 v_2$ due to the apparent moving walls in the shock frame.

Substituting in the power law relations for density and velocity gives an expression δ^*/δ and θ/δ in terms of known parameters:

$$\frac{\delta^*}{\delta} = 1 - \frac{nT_2}{T_w}\left[\frac{v_1}{v_2}I(n-1) + \left(1 - \frac{v_1}{v_2}\right)I(n)\right] \tag{B.12}$$

$$\frac{\theta}{\delta} = \frac{nT_2}{T_w}\left(1 - \frac{v_1}{v_2}\right)\left[\frac{v_1}{v_2}I(n-1) + \left(1 - 2\frac{v_1}{v_2}\right)I(n) - \left(1 - \frac{v_1}{v_2}\right)I(n+1)\right] \tag{B.13}$$

$$I(a) \equiv \int_0^1 \frac{z^a}{1 + \left(\frac{T_r}{T_w} - 1\right)z - \left(\frac{T_r}{T_w} - \frac{T_2}{T_w}\right)z^2} dz \tag{B.14}$$

The boundary layer thickness and wall shear force can be found from the Blausius relation for compressible turbulent flow over a semi-infinite flat plate:[19]

$$\delta \approx (0.130)\left[\frac{\mu_m}{\mu_2}\right]^{\frac{1}{4}}\left[\frac{T_2}{T_m}\right]^{\frac{9}{16}}\left[\frac{1 - \frac{v_1}{v_2}}{\frac{\theta}{\delta}}\right]^{\frac{3}{4}}\left|1 - \frac{v_1}{v_2}\right|^{\frac{1}{2}}\left[\frac{\nu_2}{v_2 x}\right]^{\frac{1}{4}} x \tag{B.15}$$

$$\frac{\partial\theta}{\partial x} = \frac{\tau_x}{\rho_2 v_2^2} \approx (0.0488)\left(\frac{\mu_m}{\mu_2}\right)^{\frac{1}{3}}\left(\frac{T_2}{T_m}\right)^{\frac{2}{3}}\left(1 - \frac{v_1}{v_2}\right)\left|1 - \frac{v_1}{v_2}\right|^{\frac{2}{3}}\left(\frac{mu_2}{\rho_2 v_2 \delta}\right)^{\frac{1}{4}} \tag{B.16}$$

where the mean temperature is taken to be

$$T_m \equiv (0.5)(T_w + T_2) + (0.22)(T_r - T_2) \tag{B.17}$$

Finally, it is useful to find an expression for the displacement and momentum thicknesses in the laboratory reference frame. Using a similar derivation as before gives

$$\frac{\delta^*}{\delta} = 1 - \frac{nT_2}{T_w}I(n) \tag{B.18}$$

Similarly

$$\frac{\theta}{\delta} = \frac{nT_2}{T_w}\left[I(n) - I(n+1)\right] \tag{B.19}$$

The maximum boundary layer thickness at the contact surface is a useful parameter in the shock tube design. It will correspond to the time in which the reflected shock encounters the contact surface. This gives a measure of the maximum thickness that the boundary layer will reach during any given run. More importantly, however, it will influence the distortion of the reflected shock as it encounters the interface between the two gases. This has an impact on driver gas contamination and total test time (see section 2.2.5).

The point of maximum boundary layer thickness in the shock tube flow corresponds to a distance downstream of the shock

$$\frac{x_{max}}{L_{dn}} = \frac{\left(\frac{u_r}{u_s}+1\right)\left(\frac{u_s}{u_2}-1\right)}{\left(\frac{u_r}{u_2}+1\right)} \tag{B.20}$$

in the boundary-layer model.

Variation of Free Stream Mass flow

The variation in free stream properties in region (2) can be found as a function of the displacement thickness and the mass flow across the shock. From mass conservation it can be shown that

$$\frac{\rho_2 v_2}{(\rho_2 v_2)_o} = \frac{D_{st}}{D_{st} - 4\delta^*} \tag{B.21}$$

where δ^* is the displacement thickness in the shock stationary frame. The temperature and density can then be related by the isentropic flow relations

$$\frac{a_2}{a_{2,o}} = \left[\frac{1+\frac{\gamma-1}{2}M_{2,o}^2}{1+\frac{\gamma-1}{2}M_2^2}\right]^{\frac{1}{2}} \tag{B.22}$$

$$\frac{\rho_2}{\rho_{2,o}} = \left[\frac{1+\frac{\gamma-1}{2}M_{2,o}^2}{1+\frac{\gamma-1}{2}M_2^2}\right]^{\frac{1}{\gamma-1}} \tag{B.23}$$

Finally, the free stream velocity in the tube frame can be written as a function of the shock speed and the shock frame freestream velocity:

$$\frac{u_2}{u_{2,o}} = \frac{v_2}{v_{2,o}}\left(1 - \frac{u_s}{u_{2,o}}\right) + \frac{u_s}{u_{2,o}} \tag{B.24}$$

Appendix C

Jet Starting Model

The jet was assumed to develop at a rate of $u_c/2$ where u_c is the centerline velocity of the jet. In order to solve for the jet development time, the jet was divided into two regions:

- *Linear Growth Region:* In this region, there is a potential core in which $u_c = u_e$ and a linearly growing mixing region of lower velocity.
- *Fully-Developed Region:* Once the linearly growing mixing layer has reached the centerline, u_c is assumed to decrease with a $1/x$ dependence.

The centerline velocity in the fully developed region of an axisymmetric, turbulent, free jet can be described by [32]

$$u_c = \frac{3}{8\pi}\frac{K}{\varepsilon_o x} \tag{C.1}$$

where K, the kinematic momentum, is defined as

$$K \equiv 2\pi \int_0^\infty u^2 r dr \tag{C.2}$$

Using momentum conservation, K can be expressed in terms of the jet exit velocity

$$K = K_e = u_e^2 \frac{\pi}{4} D_e^2 \tag{C.3}$$

The virtual kinematic viscosity, ε_o, is assumed to be constant over the entire jet and, from experimental correlations, is approximately [30]

$$\varepsilon_o \approx (0.0161)\sqrt{K} \tag{C.4}$$

Combining the above relations gives an expression for the centerline velocity as a function of downstream distance:

$$\frac{x}{D_e} \approx \frac{3}{16\sqrt{\pi}(0.0161)}\frac{u_e}{u_c} \approx (6.57)\frac{u_e}{u_c} \tag{C.5}$$

The beginning of the fully developed region will be at the point $u_c = u_e$. This will also define the length of the potential core.

$$\frac{l_{pc}}{D_e} = c \approx 6.57 \tag{C.6}$$

Therefore, in this approximation the length of the potential core is only a function of the nozzle exit diameter.

Having established the development speed of the jet in each region, the change in jet length is

$$D_e d\left(\frac{x}{D_e}\right) = \frac{1}{2}u_c dt \tag{C.7}$$

Integrating each side gives

$$\frac{t_{start}}{D_e} = \int_0^{\frac{l_{pc}}{D_e}} \frac{2}{U_e} d\left(\frac{x}{D_e}\right) + \int_{\frac{l_{pc}}{D_e}}^{\frac{l_{jet}}{D_e}} \frac{2\left(\frac{x}{D_e}\right)}{cu_e} d\left(\frac{x}{D_e}\right) \tag{C.8}$$

The result is an expression for the jet starting time as a function of jet exit velocity, diameter, and the required jet length:

$$\frac{t_{start}u_e}{D_e} = 2\left(\frac{l_{pc}}{D_e}\right) + \left(\frac{l_{pc}}{D_e}\right)^{-1}\left[\left(\frac{l_{jet}}{D_e}\right)^2 - \left(\frac{l_{pc}}{D_e}\right)^2\right] \tag{C.9}$$

Appendix D

Mechanical Drawings

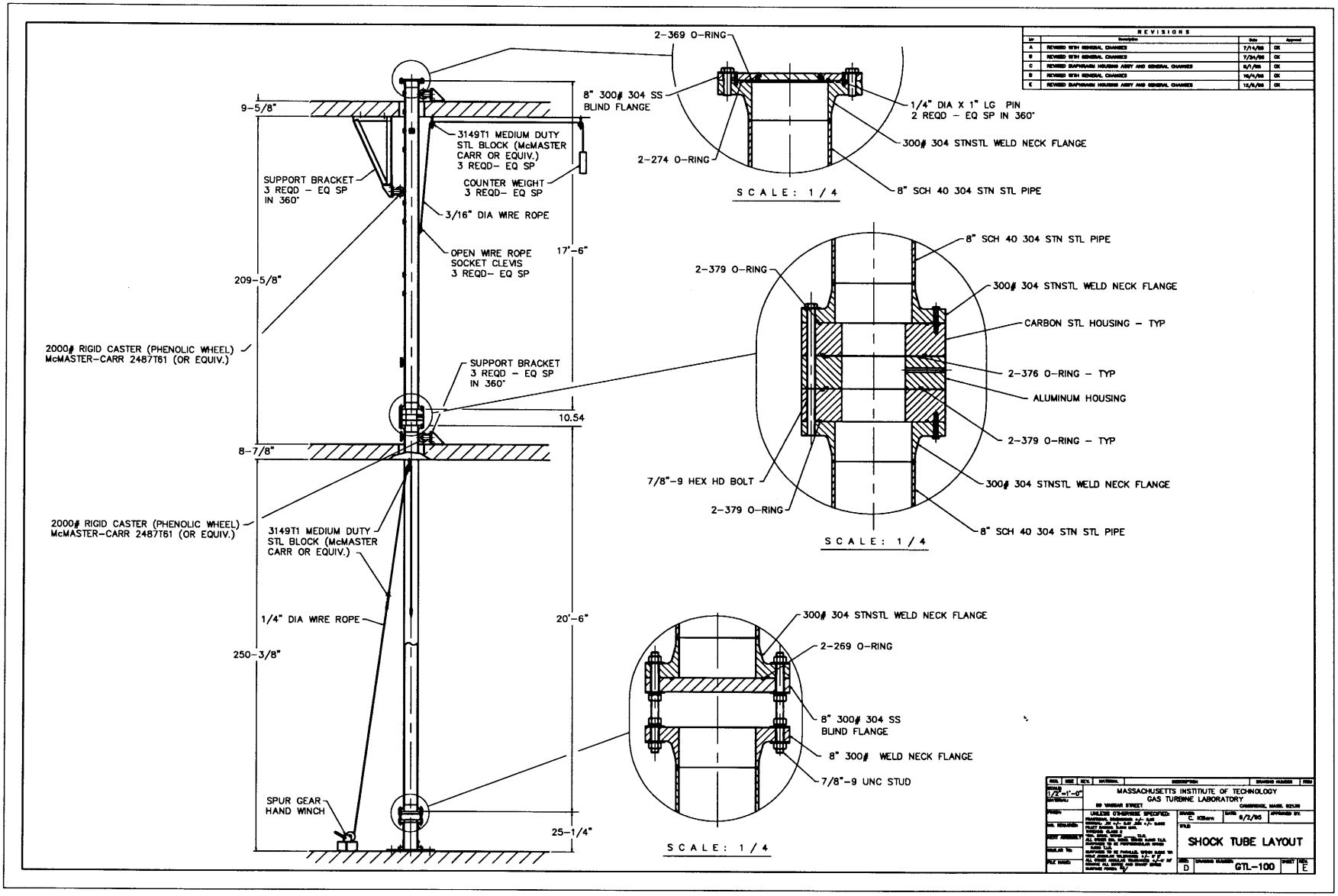
2-369 O-RING
8" 300# 304 SS
BLIND FLANGE
1/4" DIA X 1" LG PIN
2 REQD - EQ SP IN 360°
300# 304 STNSTL WELD NECK FLANGE
2-274 O-RING
8" SCH 40 304 STN STL PIPE
SCALE: 1/4
9-5/8"
3149T1 MEDIUM DUTY
STL BLOCK (McMASTER
CARR OR EQUIV.)
3 REQD- EQ SP
SUPPORT BRACKET
3 REQD - EQ SP
IN 360°
COUNTER WEIGHT
3 REQD- EQ SP
3/16" DIA WIRE ROPE
OPEN WIRE ROPE
SOCKET CLEVIS
3 REQD- EQ SP
17'-6"
209-5/8"
2000# RIGID CASTER (PHENOLIC WHEEL)
McMASTER-CARR 2487T61 (OR EQUIV.)
SUPPORT BRACKET
3 REQD - EQ SP
IN 360°
10.54
8-7/8"
2000# RIGID CASTER (PHENOLIC WHEEL)
McMASTER-CARR 2487T61 (OR EQUIV.)
3149T1 MEDIUM DUTY
STL BLOCK (McMASTER
CARR OR EQUIV.)
1/4" DIA WIRE ROPE
20'-6"
250-3/8"
SPUR GEAR
HAND WINCH
25-1/4"
8" SCH 40 304 STN STL PIPE
2-379 O-RING
300# 304 STNSTL WELD NECK FLANGE
CARBON STL HOUSING - TYP
2-376 O-RING - TYP
ALUMINUM HOUSING
2-379 O-RING - TYP
7/8"-9 HEX HD BOLT
300# 304 STNSTL WELD NECK FLANGE
2-379 O-RING
8" SCH 40 304 STN STL PIPE
SCALE: 1/4
300# 304 STNSTL WELD NECK FLANGE
2-269 O-RING
8" 300# 304 SS
BLIND FLANGE
8" 300# WELD NECK FLANGE
7/8"-9 UNC STUD
SCALE: 1/4
REVISIONS
A REVISED WITH GENERAL CHANGES 7/14/98 CK
B REVISED WITH GENERAL CHANGES 7/24/98 CK
C REVISED BAFFRAIN HOUSING ASSY AND GENERAL CHANGES 9/1/98 CK
D REVISED WITH GENERAL CHANGES 10/9/98 CK
E REVISED BAFFRAIN HOUSING ASSY AND GENERAL CHANGES 12/8/98 CK
MASSACHUSETTS INSTITUTE OF TECHNOLOGY
GAS TURBINE LABORATORY
SHOCK TUBE LAYOUT
GTL-100
D
E

REVISIONS			
Ltr	Description	Date	Approved
A	WAS (1) LIFTING LUG	7/25/95	CK
B	ADDED 2" PORTS (3)	9/1/95	CK
C	ADDED PILOT TO TOP FLANGE & PINS ON PORTS	10/4/95	CK
D	REVISED WITH GENERAL CHANGES	11/21/95	CK

NOTES:

1 – FLANGES (2) AND PIPE INSIDE DIA TO BE CONCENTRIC WITHIN .005 TIR.

2 – WELDING SHALL COMPLY WITH THE REQUIREMENTS OF ASME B31.1
WELDER SHALL BE QUALIFIED WITH THE REQUIREMENTS OF THE ASME BOILER AND PRESSURE VESSEL CODE SECTION IX.

3 – HYDROSTATIC PRESSURE TEST TO 1125 PSIG.

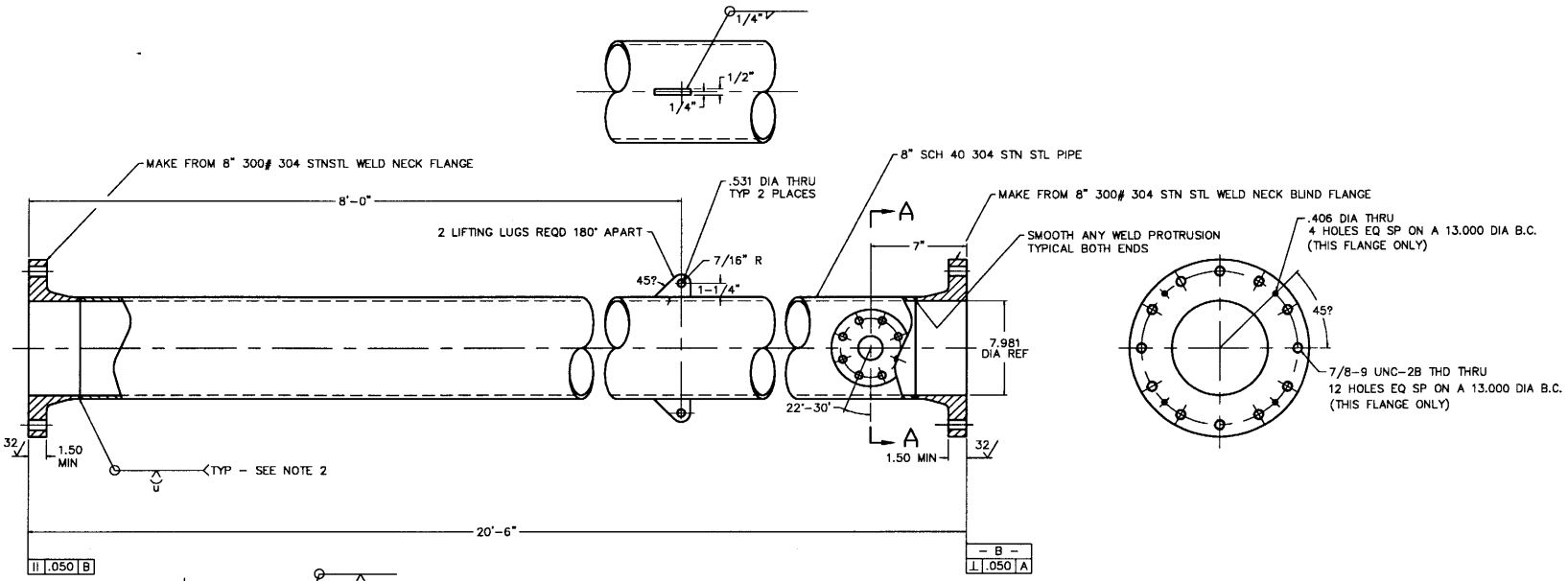

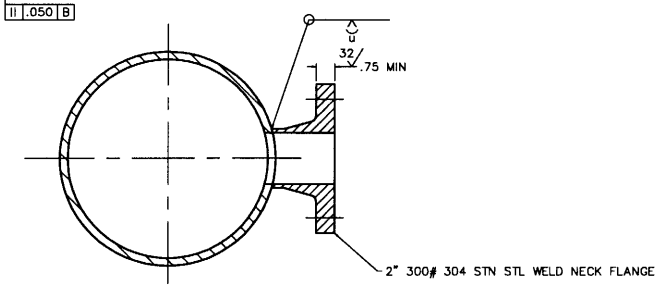

SECTION A – A

SCALE: 1 / 2

SCALE: 1/4	MASSACHUSETTS INSTITUTE OF TECHNOLOGY GAS TURBINE LABORATORY 80 VASSAR STREET CAMBRIDGE, MASS. 02139					
MATERIAL: AS NOTED	UNLESS OTHERWISE SPECIFIED:	DRAWN: C. Kilborn	DATE: 7/18/95	APPROVED BY:		
FINISH:		TITLE: PIPE SECTION, LOWER-SHOCK TUBE ASSY				
NEXT ASSEMBLY:		SIZE: D	DRAWING NUMBER: GTL-101		SHEET	REV: D
FILE NAME:						

NOTES:

1 – FLANGES (2) AND PIPE INSIDE DIA TO BE CONCENTRIC WITHIN .005 TIR.

2 – WELDING SHALL COMPLY WITH THE REQUIREMENTS OF ASME B31.1
WELDER SHALL BE QUALIFIED WITH THE REQUIREMENTS OF THE ASME BOILER AND PRESSURE VESSEL CODE SECTION IX.

3 – HYDROSTATIC PRESSURE TEST TO 1125 PSIG.

4 – PERMANENT MARK EACH PORT (5/8" DIA) WITH RESPECTIVE MARK ON EACH COVER (DWG GTL-103) MATCHED FOR EACH LOCATION. 2 COVERS TO BE MADE FOR EACH LOCATION.

REVISIONS			
Ltr	Description	Date	Approved
A	ADDED INSTRUMENTATION PORTS	7/24/95	CK
B	REVISED WITH GENERAL CHANGES	9/7/95	CK
C	REVISED WITH GENERAL CHANGES	10/4/95	CK
D	REVISED WITH GENERAL CHANGES	11/20/95	CK

PAD LOCATIONS	
DIM. X	RADIAL LOCATION
8"	90°
20"	90°
32"	90°
44"	90°
208"	90°

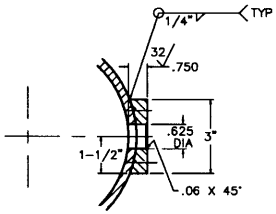

SECTION B – B
TYPICAL 5 PLACES
SCALE: 1/2

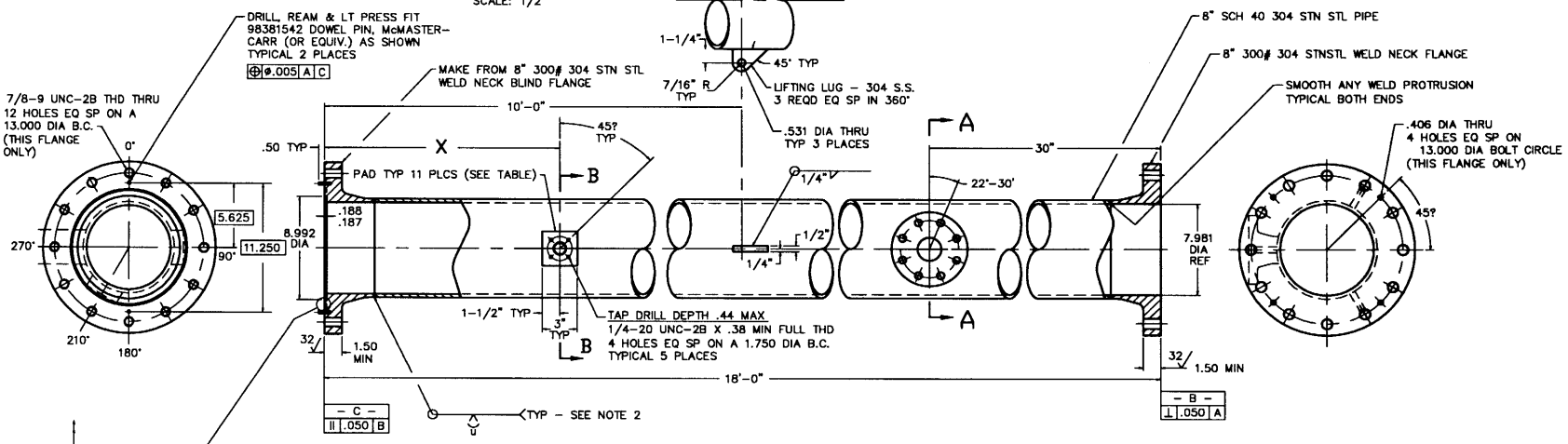

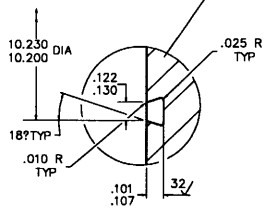

SCALE: 2 / 1
O-RING 2-274

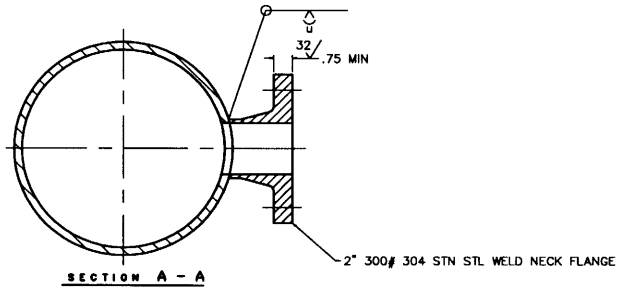

SECTION A – A
SCALE: 1 / 2

MASSACHUSETTS INSTITUTE OF TECHNOLOGY
GAS TURBINE LABORATORY
68 VASSAR STREET CAMBRIDGE, MASS. 02139

SCALE	1/4
MATERIAL	AS NOTED
FINISH	UNLESS OTHERWISE SPECIFIED:
DRAWN	C. Kilfoyle
DATE	7/19/95
TITLE	PIPE SECTION, UPPER-SHOCK TUBE ASSY
SIZE	D
DRAWING NUMBER	GTL-102
REV	D

REVISIONS			
Ltr	Description	Date	Approval
A	REVISED BOLT HOLES	9/1/95	CK
B	ADDED PIN HOLES	10/2/95	CK
C	REVISED WITH GENERAL CHANGES	11/21/95	CK

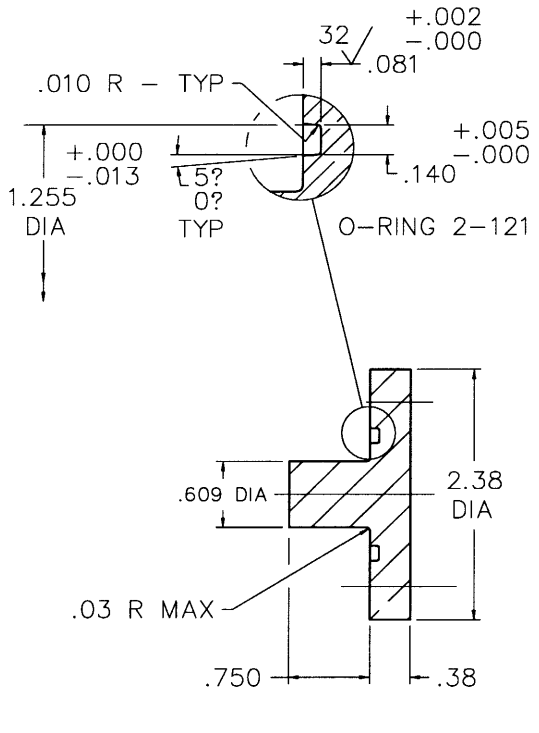

SECTION A − A

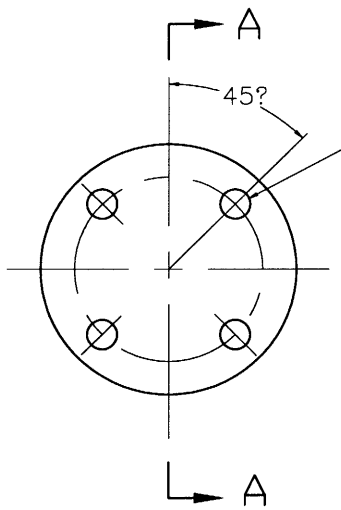

.281 DIA THRU
4 HOLES EQ SP ON A 1.750 DIA B.C.

N O T E S :

1 − MATCH END OF PLUG WITH TANGENT POINT OF INSIDE DIA OF PIPE SECTION, DWG NO. GTL−102, WITHIN +.000 −.005 PERMANENT MARK COVER WITH RESPECTIVE PORT ON PIPE. 2 COVERS TO BE MADE FOR EA PORT LOCATION.

REQ.	SIZE	REV.	MATERIAL	DESCRIPTION	DRAWING NUMBER	ITEM
SCALE: 1/1				MASSACHUSETTS INSTITUTE OF TECHNOLOGY GAS TURBINE LABORATORY 60 VASSAR STREET CAMBRIDGE, MASS. 02139		
MATERIAL: 304 S.S.						
FINISH:				UNLESS OTHERWISE SPECIFIED: FRACTIONAL DIMENSIONS: +/− 0.03 DECIMAL: .XX +/− 0.01 .XXX +/− 0.005 FILLET RADIUS: 0.010 MAX. THREADS: CLASS 2 *DIA. CONC. WITHIN ____ T.I.R. ALL OTHER DIA. CONC. WITHIN 0.005 T.I.R. SURFACES TO BE PERPENDICULAR WITHIN 0.005 T.I.R. SURFACES TO BE PARALLEL WITHIN 0.005 TIR HOLE ANGULAR TOLERANCE: +/− 0° 5' ALL OTHER ANGULAR TOLERANCE: +/−0° 30' REMOVE ALL BURRS AND SHARP EDGES SURFACE FINISH: 63	DRAWN: C. Killam	DATE: 7/18/95	APPROVED BY:
NO. REQUIRED: 10					TITLE: COVER, 5/8" INSTRUMENTATION PORT− SHOCK TUBE ASSY	
NEXT ASSEMBLY						
SIMILAR TO:						
FILE NAME:					SIZE: B DRAWING NUMBER: GTL−103	SHEET REV. C

REVISIONS			
Ltr	Description	Date	Approval
A	ADDED PIPE AND FLANGE	10/3/95	CK
B	PARALLELISM GEO. TOL. WAS .030	11/21/95	CK

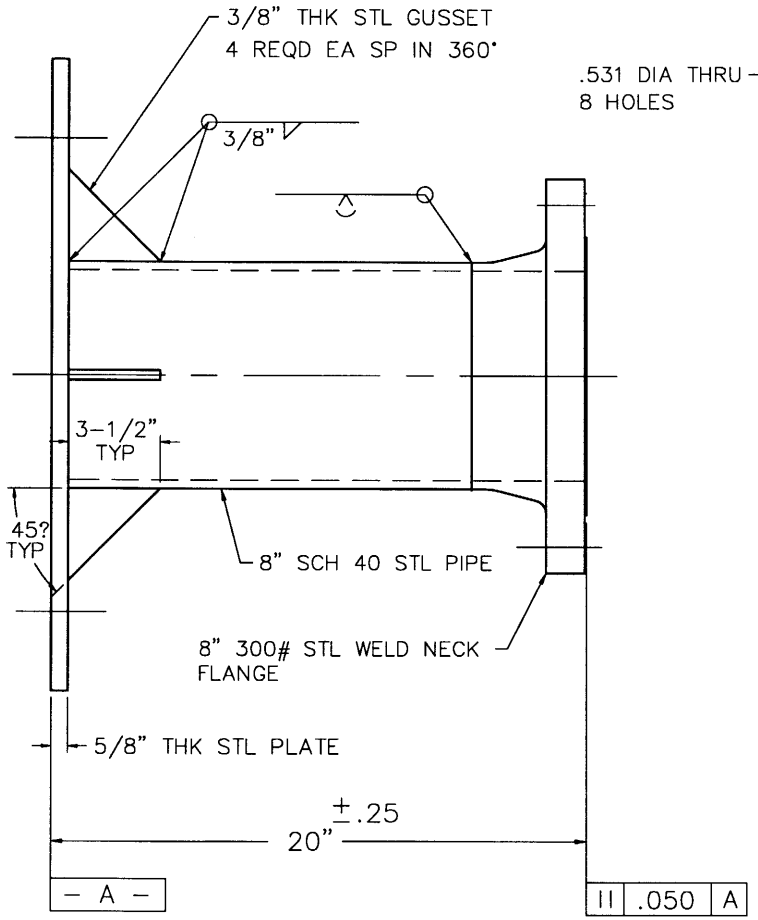

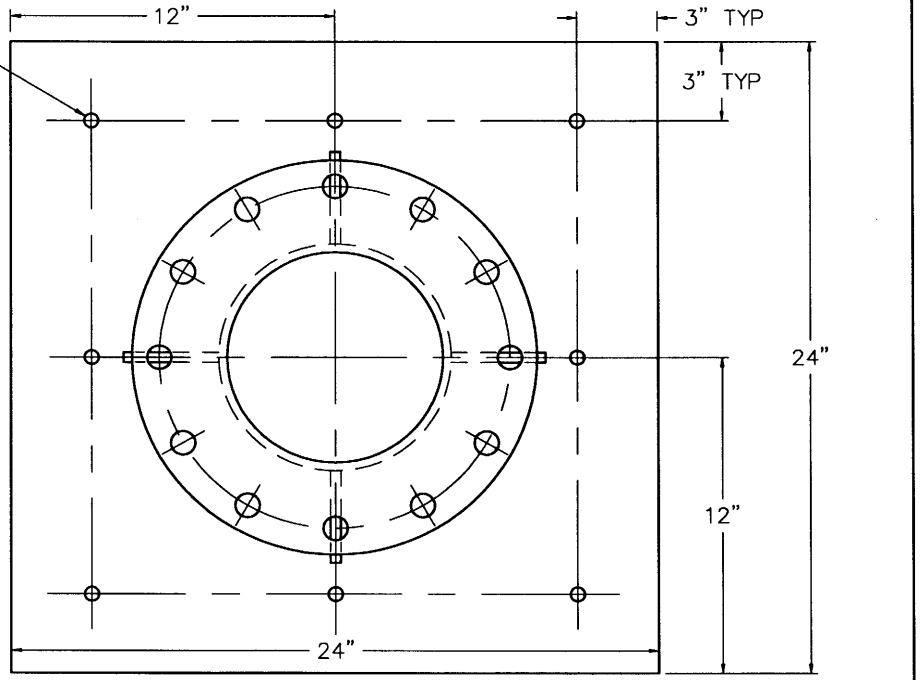

REQ.	SIZE	REV.	MATERIAL	DESCRIPTION	DRAWING NUMBER	ITEM

SCALE: 1/4

MATERIAL: CARBON STL

FINISH:

NO. REQUIRED: 1

NEXT ASSEMBLY

SIMILAR TO:

FILE NAME:

MASSACHUSETTS INSTITUTE OF TECHNOLOGY
GAS TURBINE LABORATORY
60 VASSAR STREET
CAMBRIDGE, MASS. 02139

UNLESS OTHERWISE SPECIFIED:
FRACTIONAL DIMENSIONS: +/- 0.03
DECIMAL: .XX +/- 0.01 .XXX +/- 0.005
FILLET RADIUS: 0.010 MAX.
THREADS: CLASS 2
*DIA. CONC. WITHIN _____ T.I.R.
ALL OTHER DIA. CONC. WITHIN 0.005 T.I.R.
SURFACES TO BE PERPENDICULAR WITHIN 0.005 T.I.R.
SURFACES TO BE PARALLEL WITHIN 0.005 TIR
HOLE ANGULAR TOLERANCE: +/- 0° 5'
ALL OTHER ANGULAR TOLERANCE: +/-0° 30'
REMOVE ALL BURRS AND SHARP EDGES
SURFACE FINISH: 63

DRAWN: C. Killam
DATE: 7/24/95
APPROVED BY:

TITLE: BASE PLATE, SHOCK TUBE ASSY

SIZE: B
DRAWING NUMBER: GTL-104
SHEET
REV. B

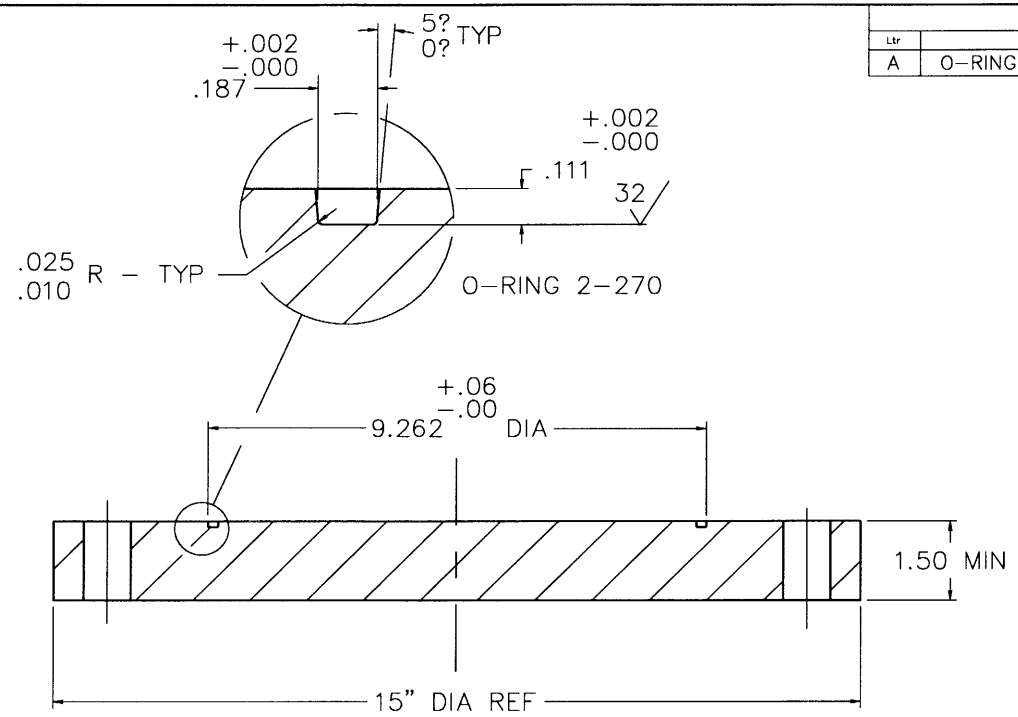

REVISIONS			
Ltr	Description	Date	Approval
A	O–RING GROOVE WAS DOVETAIL	9/1/95	CK

MAKE FROM 8" 300# BLIND FLANGE – 304 STN STL

REQ.	SIZE	REV.	MATERIAL	DESCRIPTION	DRAWING NUMBER	ITEM

SCALE: 1/2

MATERIAL: AS NOTED

FINISH:

NO. REQUIRED: 1

NEXT ASSEMBLY:

SIMILAR TO:

FILE NAME:

MASSACHUSETTS INSTITUTE OF TECHNOLOGY
GAS TURBINE LABORATORY
60 VASSAR STREET CAMBRIDGE, MASS. 02139

UNLESS OTHERWISE SPECIFIED:
FRACTIONAL DIMENSIONS: +/– 0.03
DECIMAL: .XX +/– 0.01 .XXX +/– 0.005
FILLET RADIUS: 0.010 MAX.
THREADS: CLASS 2
*DIA. CONC. WITHIN ____ T.I.R.
ALL OTHER DIA. CONC. WITHIN 0.005 T.I.R.
SURFACES TO BE PERPENDICULAR WITHIN 0.005 T.I.R.
SURFACES TO BE PARALLEL WITHIN 0.005 TIR
HOLE ANGULAR TOLERANCE: +/– 0° 5'
ALL OTHER ANGULAR TOLERANCE: +/–0° 30'
REMOVE ALL BURRS AND SHARP EDGES
SURFACE FINISH: 63

DRAWN: C. Killam
DATE: 7/18/95
APPROVED BY:

TITLE:
END PLATE, SHOCK TUBE ASSY

SIZE: B
DRAWING NUMBER: GTL–107
SHEET:
REV. A

REVISIONS			
Ltr	Description	Date	Approved
A	FLANGE THK WAS 1.50 MIN & GENERAL CHANGES	9/5/95	CK
B	.375 DEPTH WAS .250 DEEP	10/4/95	CK
C	DELETED O-RING GROOVE	12/4/95	CK

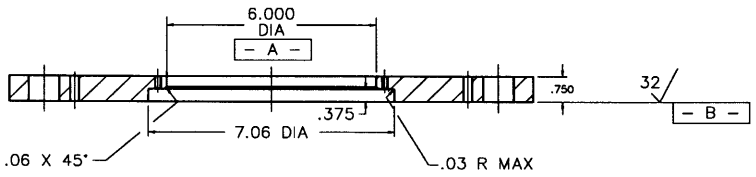

SECTION A - A

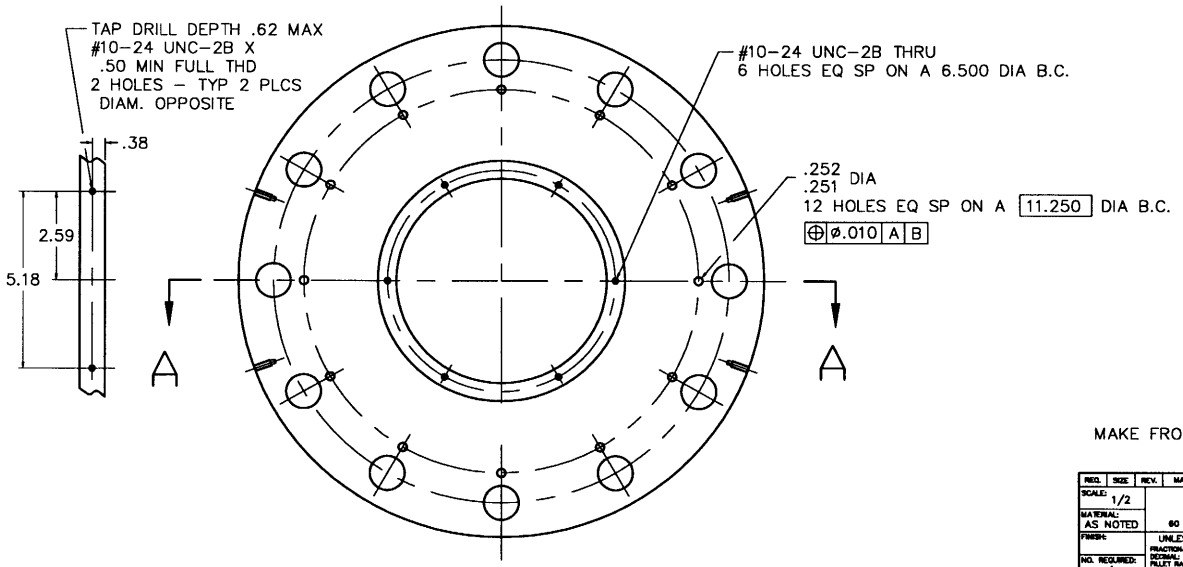

MAKE FROM 8" 300# 304 STN STL BLIND FLANGE

REQ.	SIZE	REV.	MATERIAL	DESCRIPTION	DRAWING NUMBER	ITEM

SCALE: 1/2

MATERIAL: AS NOTED

FINISH:

NO. REQUIRED: 1

NEXT ASSEMBLY

SIMILAR TO:

FILE NAME:

MASSACHUSETTS INSTITUTE OF TECHNOLOGY
GAS TURBINE LABORATORY
60 VASSAR STREET CAMBRIDGE, MASS. 02139

UNLESS OTHERWISE SPECIFIED:
FRACTIONAL DIMENSIONS +/- .03
DECIMAL: .XX +/- .01 .XXX +/- .005
FILLET RADIUS .010 MAX.
THREADS: CLASS 2
.XXX CONC WITH ⌖ T.I.R.
ALL OTHER DIA. CONC. WITHIN 0.005 T.I.R.
SURFACES TO BE PERPENDICULAR WITHIN 0.005 T.I.R.
SURFACES TO BE PARALLEL WITHIN 0.005 T.I.R.
HOLE ANGULAR TOLERANCE: +/- 0° 5'
ALL OTHER ANGULAR TOLERANCE: +/- 0° 30'
REMOVE ALL BURRS AND SHARP EDGES
SURFACE FINISH: 63

DRAWN: C. Kitiam DATE: 7/25/95 APPROVED BY:

TITLE: END PLATE, NOZZLE-SHOCK TUBE ASSY

SIZE: C DRAWING NUMBER: GTL-110 SHEET REV. C

REVISIONS			
Ltr	Description	Date	Approved
A	WAS (1) LIFTING LUG	7/25/95	CK
B	ADDED 2" PORTS (3)	9/1/95	CK
C	ADDED PILOT TO TOP FLANGE & PINS ON PORTS	10/4/95	CK
D	REVISED WITH GENERAL CHANGES	11/21/95	CK

NOTES:

1 – FLANGES (2) AND PIPE INSIDE DIA TO BE CONCENTRIC WITHIN .005 TIR.

2 – WELDING SHALL COMPLY WITH THE REQUIREMENTS OF ASME B31.1
WELDER SHALL BE QUALIFIED WITH THE REQUIREMENTS OF THE ASME BOILER AND PRESSURE VESSEL CODE SECTION IX.

3 – HYDROSTATIC PRESSURE TEST TO 1125 PSIG.

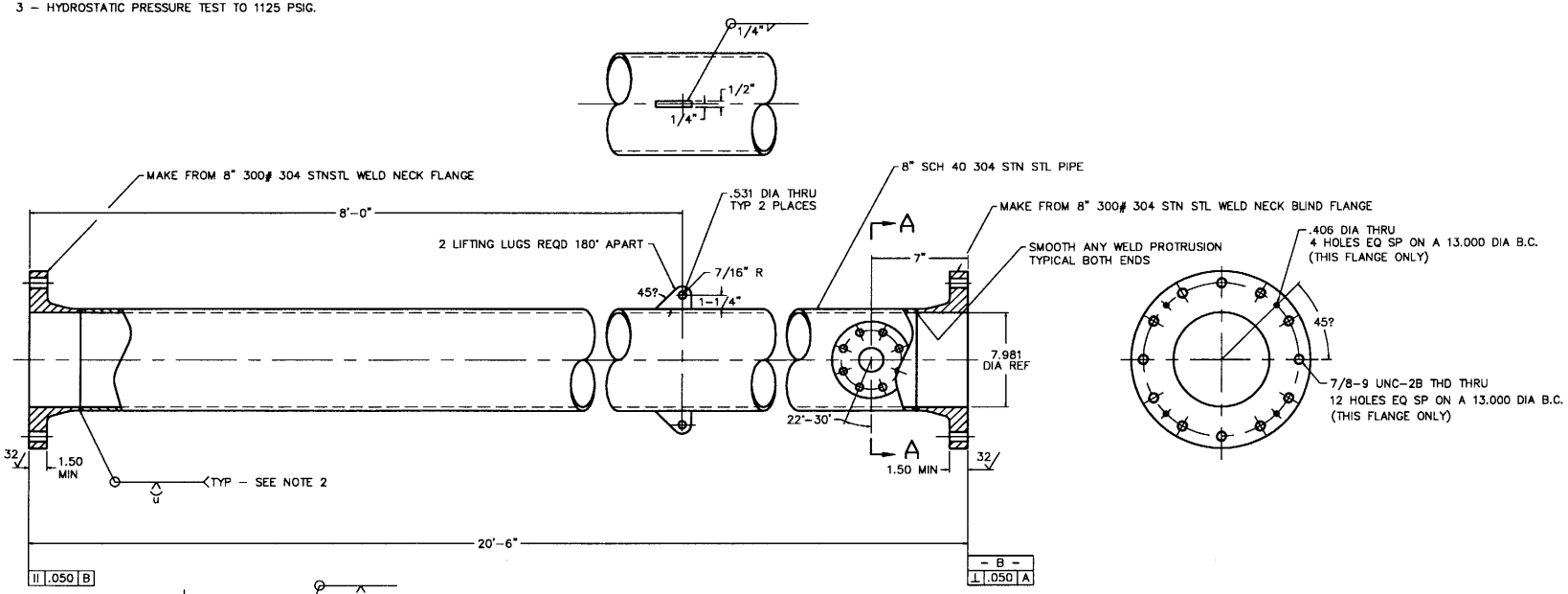

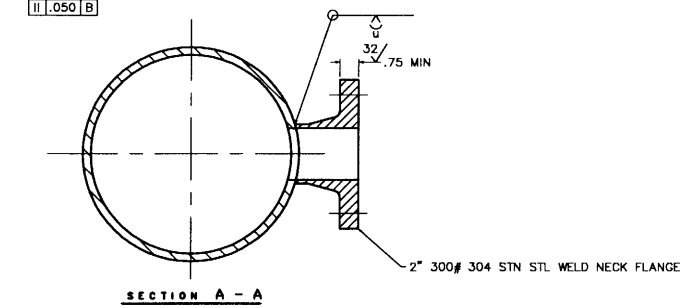

SECTION A – A

SCALE: 1 / 2

SCALE: 1/4	MASSACHUSETTS INSTITUTE OF TECHNOLOGY GAS TURBINE LABORATORY CAMBRIDGE, MASS. 02139				
DIMENSIONS: AS NOTED	60 VASSAR STREET				
FINISH:	UNLESS OTHERWISE SPECIFIED:	DRAWN: C. Killam	DATE: 7/18/95	APPROVED BY:	
MFG. REQUIRED:		TITLE: PIPE SECTION, LOWER-SHOCK TUBE ASSY			
NEXT ASSEMBLY:		SIZE: D	DRAWING NUMBER: GTL-101	SHEET:	REV: D
TEMPLATE NO:					
FILE NAME:					

REVISIONS			
Ltr	Description	Date	Approved
A	FLANGE THK WAS 1.50 MIN & GENERAL CHANGES	9/5/95	CK
B	.375 DEPTH WAS .250 DEEP	10/4/95	CK
C	DELETED O-RING GROOVE	12/4/95	CK

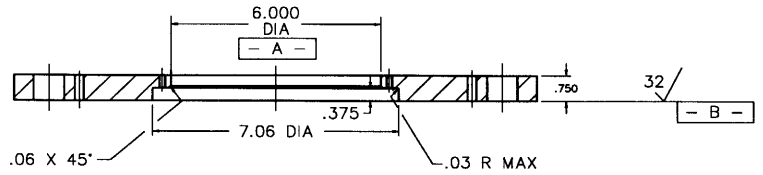

SECTION A – A

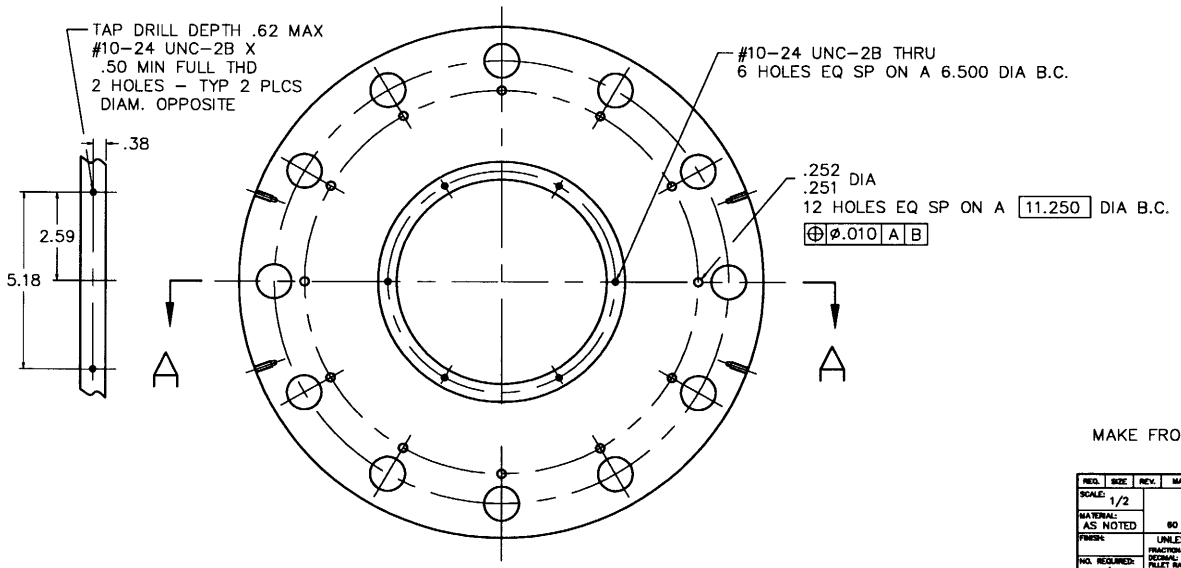

MAKE FROM 8" 300# 304 STN STL BLIND FLANGE

REQ.	SIZE	REV.	MATERIAL	DESCRIPTION	DRAWING NUMBER	ITEM
SCALE: 1/2				MASSACHUSETTS INSTITUTE OF TECHNOLOGY GAS TURBINE LABORATORY 60 VASSAR STREET CAMBRIDGE, MASS. 02139		
MATERIAL: AS NOTED						
FINISH:				UNLESS OTHERWISE SPECIFIED:	DRAWN: C. Killam	DATE: 7/25/95
NO. REQUIRED: 1				FRACTIONAL DIMENSIONS +/– 0.03 DECIMAL .XX +/– 0.01 .XXX +/– 0.005 FILLET RADIUS 0.010 MAX. THREADS CLASS 2 VISI. CONC. WITHIN ___ T.I.R. ALL OTHER DIA. CONC. WITHIN 0.005 T.I.R. SURFACES TO BE PERPENDICULAR WITHIN 0.005 T.I.R. SURFACES TO BE PARALLEL WITHIN 0.005 TIR HOLE ANGULAR TOLERANCE: +/– 0° 5' ALL OTHER ANGULAR TOLERANCE: +/–0° 30' REMOVE ALL BURRS AND SHARP EDGES SURFACE FINISH: 63	APPROVED BY:
NEXT ASSEMBLY					TITLE: END PLATE, NOZZLE–SHOCK TUBE ASSY	
SIMILAR TO:					SIZE: C	DRAWING NUMBER: GTL–110
FILE NAME:						SHEET
						REV. C

REVISIONS			
Ltr	Description	Date	Approval
A	REVISED LENGTH	11/21/95	CK

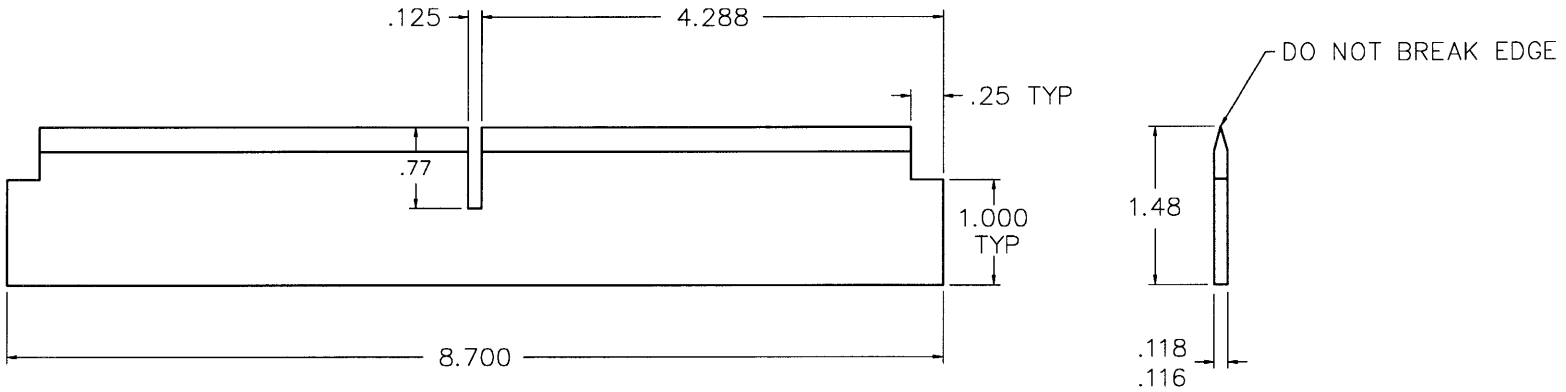

REQ.	SIZE	REV.	MATERIAL	DESCRIPTION	DRAWING NUMBER	ITEM

SCALE: 1/1

MATERIAL: 304 S.S.

FINISH:

NO. REQUIRED: 2

NEXT ASSEMBLY

SIMILAR TO:

FILE NAME:

MASSACHUSETTS INSTITIUTE OF TECHNOLOGY
GAS TURBINE LABORATORY
60 VASSAR STREET CAMBRIDGE, MASS. 02139

UNLESS OTHERWISE SPECIFIED:
FRACTIONAL DIMENSIONS: +/- 0.03
DECIMAL: .XX +/- 0.01 .XXX +/- 0.005
FILLET RADIUS: 0.010 MAX.
THREADS: CLASS 2
*DIA. CONC. WITHIN ____ T.I.R.
ALL OTHER DIA. CONC. WITHIN 0.005 T.I.R.
SURFACES TO BE PERPENDICULAR WITHIN 0.005 T.I.R.
SURFACES TO BE PARALLEL WITHIN 0.005 TIR
HOLE ANGULAR TOLERANCE: +/- 0° 5'
ALL OTHER ANGULAR TOLERANCE: +/-0° 30'
REMOVE ALL BURRS AND SHARP EDGES
SURFACE FINISH: 63√

DRAWN: C. Killam
DATE: 9/5/95
APPROVED BY:

TITLE:
KNIFE BLADE, SHOCK TUBE ASSY

SIZE: B
DRAWING NUMBER: GTL-117
SHEET
REV. A

REVISIONS			
Ltr	Description	Date	Approval
A	PARALLELISM TOL. WAS .030	11/21/95	CK

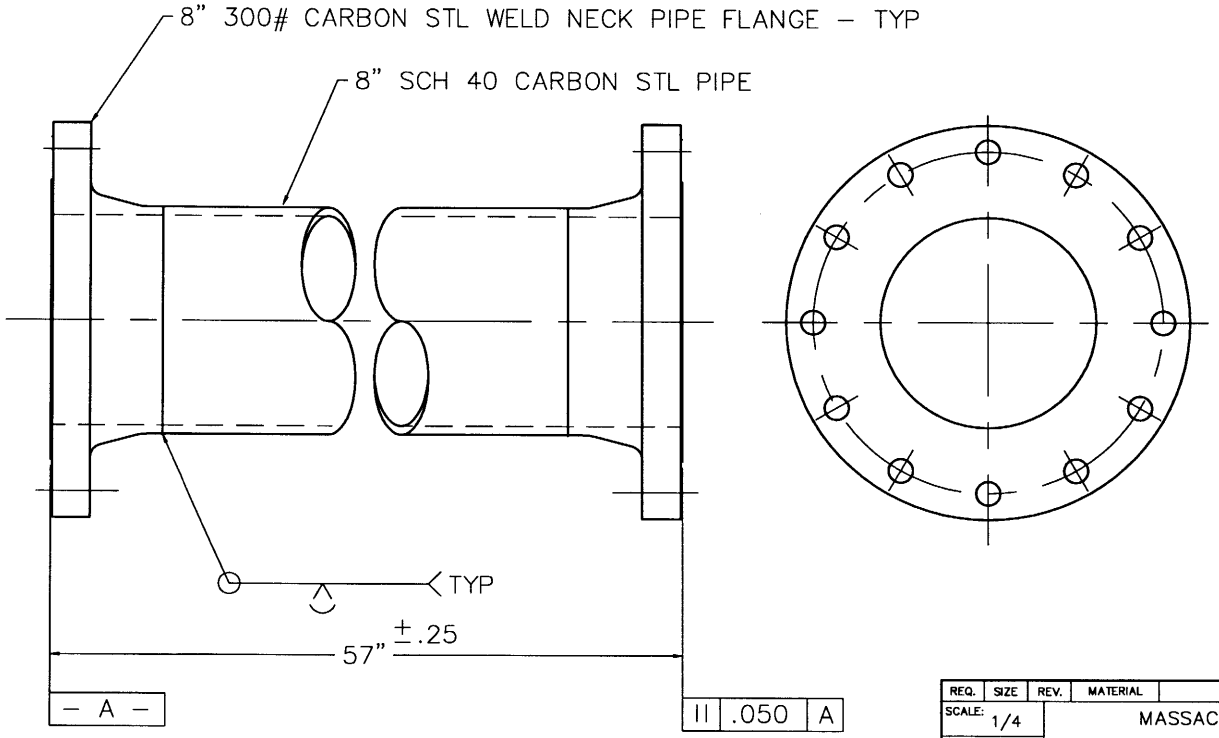

REQ.	SIZE	REV.	MATERIAL	DESCRIPTION	DRAWING NUMBER	ITEM

SCALE: 1/4

MATERIAL: AS NOTED

FINISH:

NO. REQUIRED: 1

NEXT ASSEMBLY

SIMILAR TO:

FILE NAME:

MASSACHUSETTS INSTITIUTE OF TECHNOLOGY
GAS TURBINE LABORATORY
60 VASSAR STREET CAMBRIDGE, MASS. 02139

UNLESS OTHERWISE SPECIFIED:
FRACTIONAL DIMENSIONS: +/– 0.03
DECIMAL: .XX +/– 0.01 .XXX +/– 0.005
FILLET RADIUS: 0.010 MAX.
THREADS: CLASS 2
*DIA. CONC. WITHIN _____ T.I.R.
ALL OTHER DIA. CONC. WITHIN 0.005 T.I.R.
SURFACES TO BE PERPENDICULAR WITHIN 0.005 T.I.R.
SURFACES TO BE PARALLEL WITHIN 0.005 TIR
HOLE ANGULAR TOLERANCE: +/– 0° 5'
ALL OTHER ANGULAR TOLERANCE: +/–0° 30'
REMOVE ALL BURRS AND SHARP EDGES
SURFACE FINISH: 63

DRAWN: C. Killam
DATE: 7/18/95
APPROVED BY:

TITLE: PIPE SECTION, BASE SUPPORT– SHOCK TUBE ASSY

SIZE: B
DRAWING NUMBER: GTL–122
SHEET
REV. A

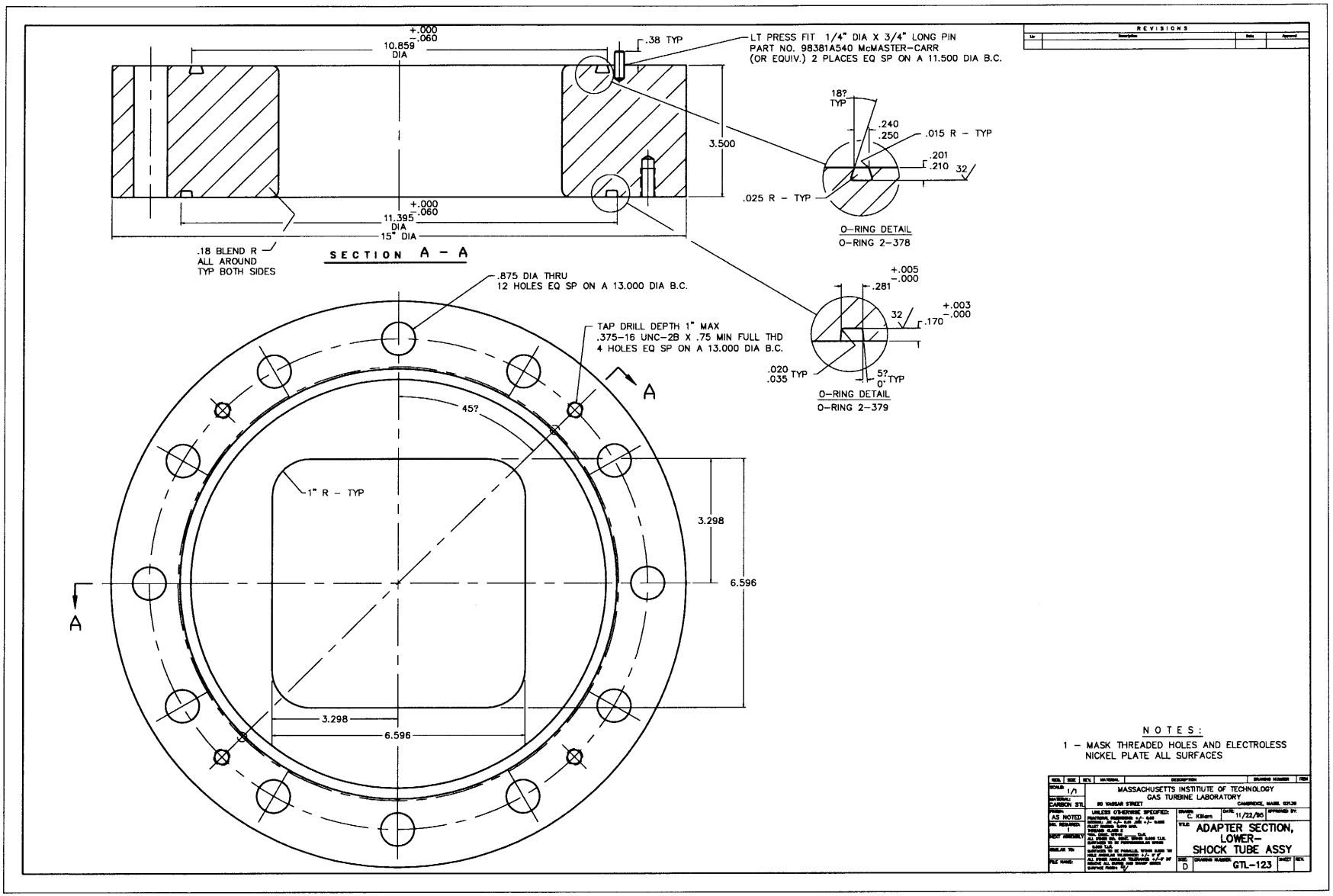
+.000
-.060
10.859
DIA
.38 TYP
LT PRESS FIT 1/4" DIA X 3/4" LONG PIN
PART NO. 98381A540 McMASTER-CARR
(OR EQUIV.) 2 PLACES EQ SP ON A 11.500 DIA B.C.
3.500
18?
TYP
.240
.250
.015 R - TYP
.201
.210
32
.025 R - TYP
O-RING DETAIL
O-RING 2-378
+.000
-.060
11.395
DIA
15" DIA
.18 BLEND R
ALL AROUND
TYP BOTH SIDES
SECTION A - A
.875 DIA THRU
12 HOLES EQ SP ON A 13.000 DIA B.C.
TAP DRILL DEPTH 1" MAX
.375-16 UNC-2B X .75 MIN FULL THD
4 HOLES EQ SP ON A 13.000 DIA B.C.
+.005
-.000
.281
32
+.003
-.000
.170
.020
.035 TYP
5?
0? TYP
O-RING DETAIL
O-RING 2-379
A
45?
1" R - TYP
3.298
6.596
A
3.298
6.596
REVISIONS
NOTES:
1 - MASK THREADED HOLES AND ELECTROLESS
NICKEL PLATE ALL SURFACES
MASSACHUSETTS INSTITUTE OF TECHNOLOGY
GAS TURBINE LABORATORY
CAMBRIDGE, MASS. 02139
ADAPTER SECTION,
LOWER-
SHOCK TUBE ASSY
GTL-123
D

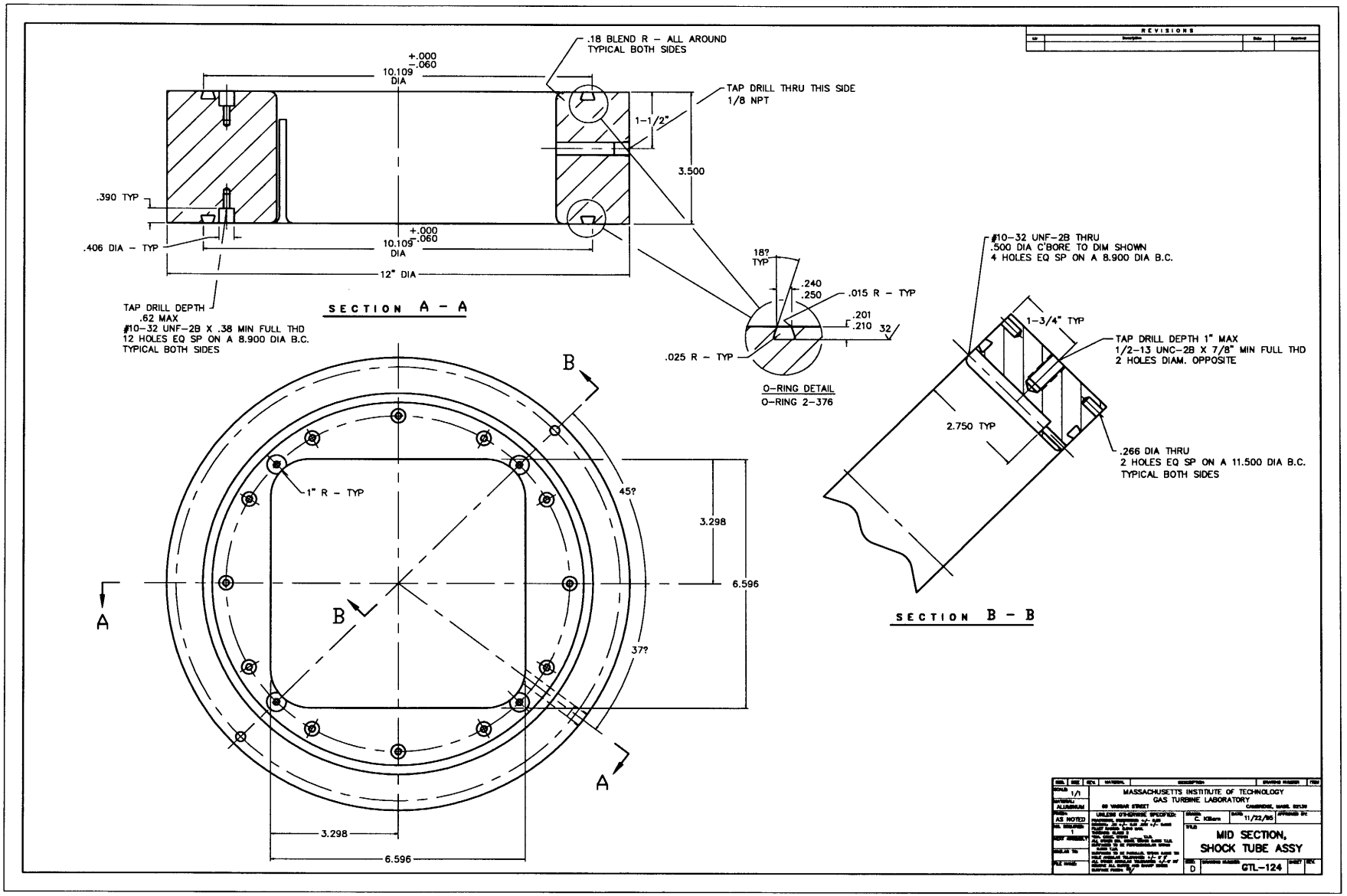
REVISIONS
.18 BLEND R – ALL AROUND
TYPICAL BOTH SIDES
+.000
10.109 -.060
DIA
TAP DRILL THRU THIS SIDE
1/8 NPT
1-1/2"
3.500
.390 TYP
.406 DIA – TYP
+.000
10.109 -.060
DIA
12" DIA
TAP DRILL DEPTH
.62 MAX
#10-32 UNF-2B X .38 MIN FULL THD
12 HOLES EQ SP ON A 8.900 DIA B.C.
TYPICAL BOTH SIDES
SECTION A – A
18?
TYP
.240
.250
.015 R – TYP
.201
.210
32
.025 R – TYP
O-RING DETAIL
O-RING 2-376
#10-32 UNF-2B THRU
.500 DIA C'BORE TO DIM SHOWN
4 HOLES EQ SP ON A 8.900 DIA B.C.
1-3/4" TYP
TAP DRILL DEPTH 1" MAX
1/2-13 UNC-2B X 7/8" MIN FULL THD
2 HOLES DIAM. OPPOSITE
2.750 TYP
.266 DIA THRU
2 HOLES EQ SP ON A 11.500 DIA B.C.
TYPICAL BOTH SIDES
SECTION B – B
B
1" R – TYP
45?
3.298
6.596
37?
A
B
A
3.298
6.596
MASSACHUSETTS INSTITUTE OF TECHNOLOGY
GAS TURBINE LABORATORY
MATERIAL
ALUMINUM
AS NOTED
C. Kilsen
11/22/95
MID SECTION,
SHOCK TUBE ASSY
D
GTL-124

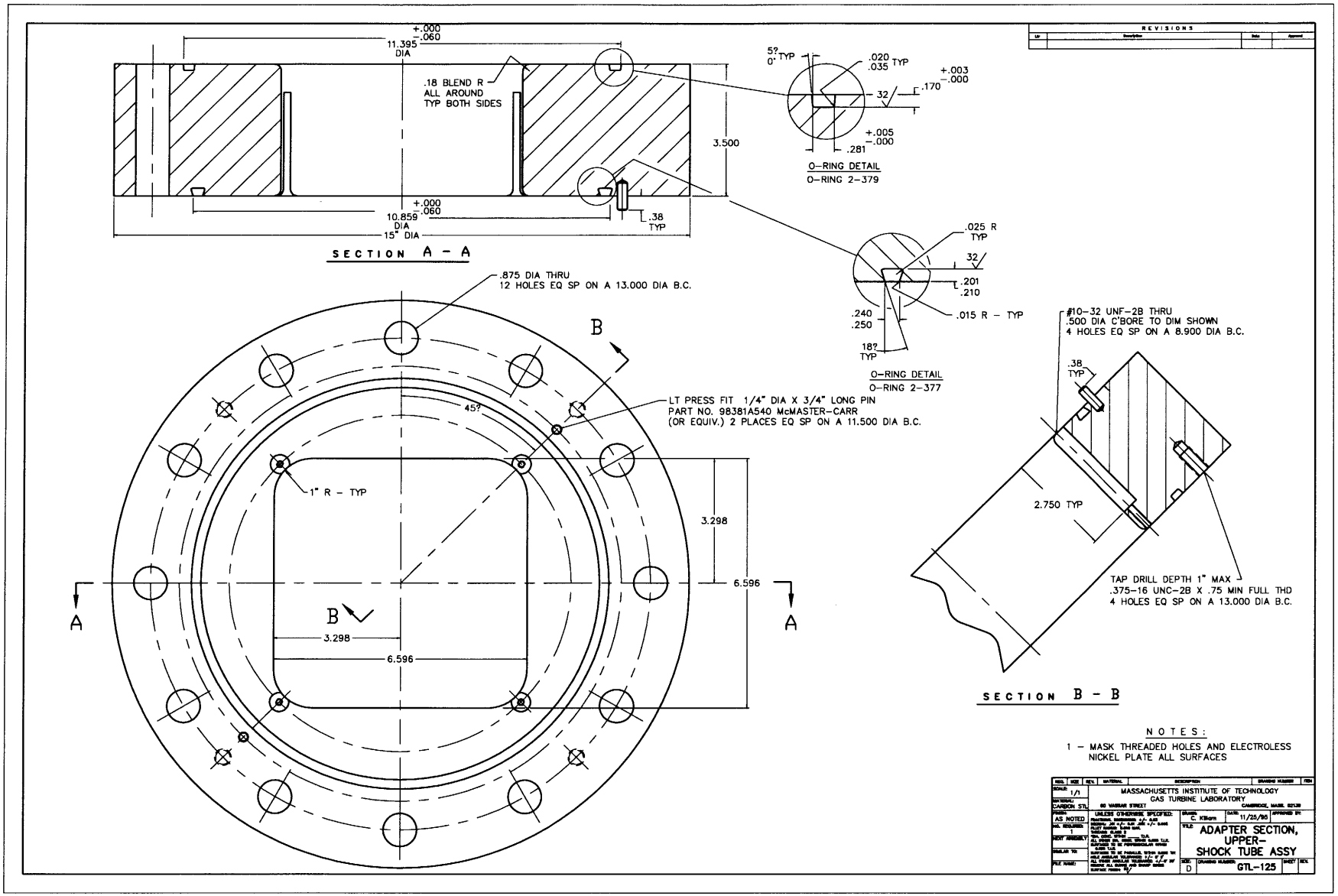
REVISIONS
11.395 +.000 -.060 DIA
.18 BLEND R ALL AROUND TYP BOTH SIDES
3.500
10.859 +.000 -.060 DIA
15" DIA
.38 TYP
SECTION A - A
5° TYP
0° TYP
.020 TYP
.035
+.003 -.000
32
.170
+.005 -.000
.281
O-RING DETAIL
O-RING 2-379
.025 R TYP
32
.201
.210
.240
.250
.015 R - TYP
18° TYP
O-RING DETAIL
O-RING 2-377
.875 DIA THRU
12 HOLES EQ SP ON A 13.000 DIA B.C.
B
LT PRESS FIT 1/4" DIA X 3/4" LONG PIN
PART NO. 98381A540 McMASTER-CARR
(OR EQUIV.) 2 PLACES EQ SP ON A 11.500 DIA B.C.
45°
1" R - TYP
3.298
6.596
A
A
B
3.298
6.596
#10-32 UNF-2B THRU
.500 DIA C'BORE TO DIM SHOWN
4 HOLES EQ SP ON A 8.900 DIA B.C.
.38 TYP
2.750 TYP
TAP DRILL DEPTH 1" MAX
.375-16 UNC-2B X .75 MIN FULL THD
4 HOLES EQ SP ON A 13.000 DIA B.C.
SECTION B - B
NOTES:
1 - MASK THREADED HOLES AND ELECTROLESS NICKEL PLATE ALL SURFACES
MASSACHUSETTS INSTITUTE OF TECHNOLOGY
GAS TURBINE LABORATORY
CAMBRIDGE, MASS. 02139
C. Kiorn
11/28/95
ADAPTER SECTION, UPPER- SHOCK TUBE ASSY
GTL-125
D

REVISIONS			
Ltr	Description	Date	Approval

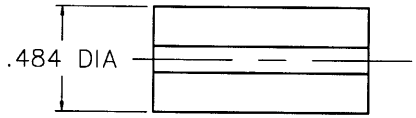

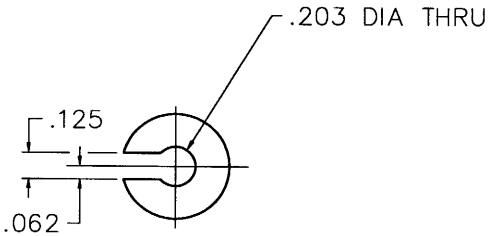

REQ.	SIZE	REV.	MATERIAL	DESCRIPTION	DRAWING NUMBER	ITEM

SCALE: 2/1

MATERIAL: ALUMINUM

FINISH:

NO. REQUIRED: 8

NEXT ASSEMBLY

SIMILAR TO:

FILE NAME:

MASSACHUSETTS INSTITUTE OF TECHNOLOGY
GAS TURBINE LABORATORY
60 VASSAR STREET CAMBRIDGE, MASS. 02139

UNLESS OTHERWISE SPECIFIED:
FRACTIONAL DIMENSIONS: +/- 0.03
DECIMAL: .XX +/- 0.01 .XXX +/- 0.005
FILLET RADIUS: 0.010 MAX.
THREADS: CLASS 2
*DIA. CONC. WITHIN _____ T.I.R.
ALL OTHER DIA. CONC. WITHIN 0.005 T.I.R.
SURFACES TO BE PERPENDICULAR WITHIN 0.005 T.I.R.
SURFACES TO BE PARALLEL WITHIN 0.005 TIR
HOLE ANGULAR TOLERANCE: +/- 0° 5'
ALL OTHER ANGULAR TOLERANCE: +/-0° 30'
REMOVE ALL BURRS AND SHARP EDGES
SURFACE FINISH: 63

DRAWN: C. Killam
DATE: 11/26/95
APPROVED BY:

TITLE: RETAINER, KNIFE BLADE– SHOCK TUBE ASSY

SIZE: B
DRAWING NUMBER: GTL–126
SHEET
REV.

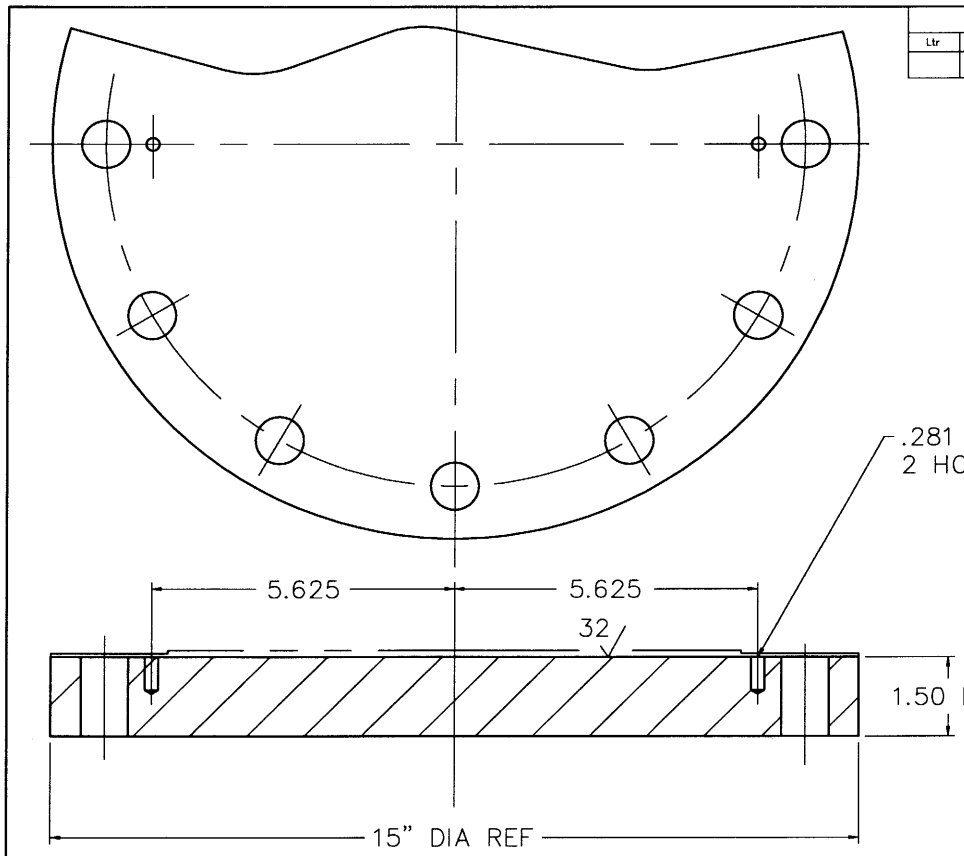

REVISIONS			
Ltr	Description	Date	Approval

MAKE FROM 8" 300# BLIND FLANGE – CARBON STL

REQ.	SIZE	REV.	MATERIAL	DESCRIPTION	DRAWING NUMBER	ITEM

SCALE: 1/2

MATERIAL: AS NOTED

FINISH:

NO. REQUIRED: 1

NEXT ASSEMBLY

SIMILAR TO:

FILE NAME:

MASSACHUSETTS INSTITUTE OF TECHNOLOGY
GAS TURBINE LABORATORY
60 VASSAR STREET CAMBRIDGE, MASS. 02139

UNLESS OTHERWISE SPECIFIED:
FRACTIONAL DIMENSIONS: +/- 0.03
DECIMAL: .XX +/- 0.01 .XXX +/- 0.005
FILLET RADIUS: 0.010 MAX.
THREADS: CLASS 2
*DIA. CONC. WITHIN _____ T.I.R.
ALL OTHER DIA. CONC. WITHIN 0.005 T.I.R.
SURFACES TO BE PERPENDICULAR WITHIN 0.005 T.I.R.
SURFACES TO BE PARALLEL WITHIN 0.005 TIR
HOLE ANGULAR TOLERANCE: +/- 0° 5'
ALL OTHER ANGULAR TOLERANCE: +/-0° 30'
REMOVE ALL BURRS AND SHARP EDGES
SURFACE FINISH: 63

DRAWN: C. Killam | DATE: 11/30/95 | APPROVED BY:

TITLE:
END PLATE, SHOCK TUBE ASSY

SIZE: B | DRAWING NUMBER: GTL-127 | SHEET | REV.